A STUDY OF THE FRAGMENTATION-FISSION OF ^{238}U ON A ^{9}Be TARGET AT 81 MeV/u

By

Anthony Steven Nettleton

A DISSERTATION

Submitted to
Michigan State University
in partial fulfillment of the requirements
for the degree of

DOCTOR OF PHILSOPHY

Physics

2011

Abstract

A STUDY OF THE FRAGMENTATION-FISSION OF ^{238}U ON A ^{9}Be TARGET AT 81 MeV/u

By

Anthony Steven Nettleton

In this work we examine the production of fission fragments from the reaction of 81 MeV/u ^{238}U on ^{9}Be targets with thicknesses of 9, 47, and 94 mg/cm^{2}. The A1900 separator and detector systems were used to make particle identification of the fragments. The fragments were characterized by their mass, nuclear charge, atomic charge, and momentum. Over 400 partial momentum distributions were measured and cross sections for a selection of isotopes were calculated and compared to theoretical predictions and previous work. The predictions of the code LISE++ were compared to the results with general overall agreement. Eight new isomers were identified and three new isomeric transitions were observed.

TABLE OF CONTENTS

LIST OF TABLES

LIST OF FIGURES

1.Introduction

The atomic nucleus is a complex and elegant system of many particles bound together through interactions involving both the strong and electroweak forces. Three of the four fundamental forces of nature contribute to the behavior of nuclei and their study can provide a unique insight into quantum many-body science. It is in particular, the small size of the nucleus and the finite number of constituents that makes it a unique laboratory. Despite all of the exotic science that can be observed in the nucleus it remains a surprisingly inaccessible experimental environment. This thesis deals with advancing the methods to expand our ability to study the nuclear environment and in particular with techniques to allow a broader range of nuclides to be produced and studied.

Early studies of the nucleus focused on stable or near-stable isotopes that could be found in nature. Examination of these isotopes provided a great deal of insight into nuclear structure, especially in the development of a shell structure model that is a rough parallel to the electron shell model of atomic structure [May50][Hax50][Wig36]. However more recent experiments with more unstable, exotic isotopes (often referred to as rare because they are not found naturally) has showed that many of the simple assumptions of nuclear properties are not valid [Aum05]. To get a better insight into the evolution of nuclear structure with the number of neutrons for a given number of protons it is necessary to be able to study isotopes removed from stability and characterize their properties.

Research with an expanded range of rare isotopes will also benefit fields outside of basic nuclear science. The field of astrophysics has found that many of the primary nuclear reactions in stars and stellar explosions, which have over time produced the elements in nature, involve exotic nuclei not found on Earth [Lan11][Bur57]. To model these stellar processes, astrophysicists need to know the properties of these rare isotopes and how they interact with other nuclei. Beyond discovery science, medical science uses rare isotopes as well, most notably in cancer treatments using radioisotopes and positron emission tomography[Ter75]. The availability of greater quantities of rare isotopes may allow new procedures to be developed.

This dissertation will describe new data on one of the most promising methods for producing a wide range of new isotopes, namely projectile fission. Coulomb and fragmentation-induced fission is predicted to generate more than half of the new isotopes that will become available in the next generation of heavy-ion based rare isotope facilities. However, fission processes have only been studied in great detail at one heavy-ion facility, GSI, and then only with a limited range of parameters and primary beam energy [Sch00]. The experiments described here attempt to extend the understanding of projectile fission (and the process of fission in general) by examining fragmentation-fission at a much lower energy (81 MeV/u compared to 350 MeV/u or 1 GeV/u) than in previous work in order to make the models used to describe the process more robust.

1.1 Rare Isotope Production

Rare isotope facilities have evolved along with the development of improved experimental techniques[Mor98]. The two main difficulties in rare isotope work are first to

generate the isotope itself and then to be able to collect and separate it from the other isotopes simultaneously produced. The production cross sections for the rarest isotopes can be in the low attobarns, compared to nuclear interaction cross sections of barns and hence huge primary beam intensities are needed as well as sensitive and efficient means to separate fragments. Ultimately, for the most interesting isotopes only a few atoms may be produced and techniques to work with single atoms are needed.

There are two main methods for the production of rare isotopes, isotope separation on-line, ISOL, and in-flight separation [Huy04]. Due to accelerator technology the initial studies of rare isotopes used ISOL production, which consisted of accelerating a beam of light particles, e.g. protons, into a heavier stable target material. These particles would then interact with the target creating a number of rare isotopes. In order to study these products it was then necessary to extract them from the target, identify them, and separate them from undesired products. While this technique is able to produce large quantities of isotopes in the target, it is limited in what can be efficiently extracted from the target. The time to complete the extraction processes, on the order of one second [Mus03], as well as moving the fragments to the experimental setup also severely limited what could be observed to products with a relatively long half-life, on the order of the speed of the processes.

Over the past thirty years, technological innovations allowed for the development of more powerful heavy-ion accelerators and more capable fragment separators [Det85][Tan85][Mor03]. With these developments it became possible for the in-flight techniques to be competitive to the ISOL techniques for the generation of beams of heavier isotopes. The benefit of this in-flight separation in "inverse kinematic" arrangement was that it allowed the fragments to continue through the target after the reaction avoiding the problems of

having to extract the products from the target material. Later chapters of this thesis will concentrate on in-flight separation of fission products (the topic of this thesis) and describe the function of these devices and how desired nuclides can be selected. Since this separation takes place in-flight and the fragments do not need to be reaccelerated to move to an experimental setup, this process dramatically reduces the minimum lifetime of fragments that can be studied.

The in-flight separation technique described in the previous paragraph has been used for over 30 years to make beams of rare isotopes [Det85][Tan85]. Different reaction methods can be used to produce the rare isotopes ranging from fission (the topic of this thesis) to fragmentation [Mor04]. A disadvantage of the in-flight technique is that the ions are produced at velocities much greater than that desired for many subsequent experiments. This limitation is overcome by slowing the ions, thermalizing them in gas [Bol05], and then reaccelerating them to the desired energy [Schwar10]. This concept is central to the Facility for Rare Isotope Beams, FRIB, being constructed at Michigan State University.

Figure 1 shows the optimum production method for making a reaccelerated low-energy beam of any specific isotopes [Gru99]. As can be seen from the blue region, fission is the process best suited to produce neutron rich isotope with an atomic number between approximately 20 and 50. Because of this, in-flight fission production should be an essential element for any facility that plans to probe the natures of the most exotic isotopes as they approach the neutron drip line. Not easily seen in the figure is that much of the yellow region above atomic number 60 will be best produced by uranium fragmentation, also highlighting the importance of the present experiments with uranium beams.

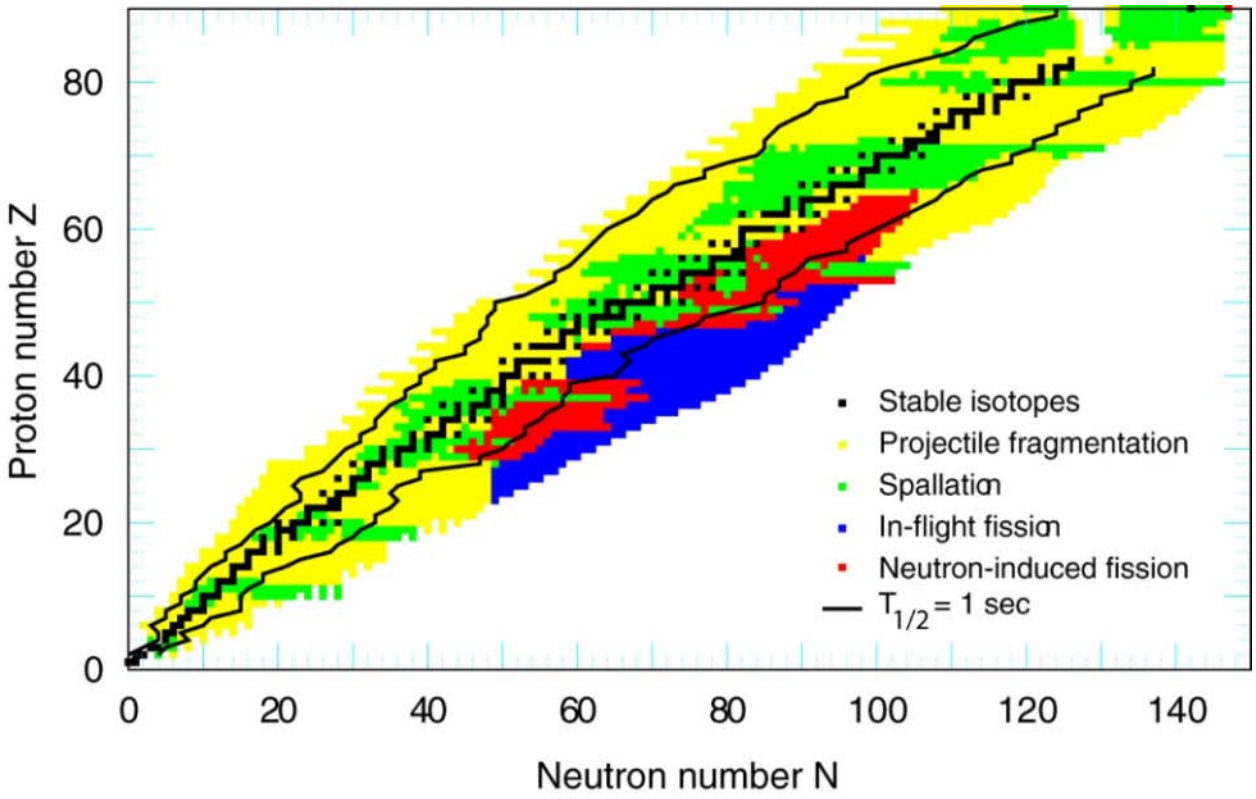

Figure 1: Table of nuclides that are producible in modern facilities, color indicates most favorable production mechanism to produce a reaccelerated beam [Gru99]. For interpretation of the references to color in this and all other figures, the reader is referred to the electronic version of this dissertation

1.2 Rare isotope facilities

Research using in-flight production based on projectile fragmentation and fission has been based primarily at four locations worldwide. These locations, GANIL in France [De85], GSI in Germany [Sch00], RIKEN in Japan [Uen08], and the NSCL/FRIB facility [Sto05] in the United States conduct the majority of rare isotope research using high-energy in-flight

separation. In order to produce and study isotopes with shorter half-lives and lower production probabilities these facilities have all recently had major upgrades approved and put into production.

Early work was done at GSI in the 1990's to characterize the fission products but the fragments were not produced at high rates and were not used to make a secondary beam to send to an experimental station. Later work in the 2000's at GSI and RIKEN expanded upon these early studies and created some secondary beams intense enough for follow on experimentation [Jun07]. These experiments will be discussed in more detail in a later chapter. The present work was designed to complement those previous studies and allow for a more complete characterization of the energy dependence of fission fragment production and refinement of the models used in designing the new facilities.

Figure 2 illustrates the facilities worldwide that are currently involved in scientific nuclear research. Of the facilities using in-flight separation (magenta labels), the new facilities of GSI FAIR, RIKEN RIBF and the FRIB are designed with the capability to use fission as a means to produce isotope beams usable in advanced experimentation. The figure illustrates the great interest worldwide in the science of rare isotopes and the importance of basic information on isotope production methods. The figure further illustrates the importance of the work described in this thesis as the results will be of interest to a number of research facilities which plan to use in flight fission a rare isotope production method.

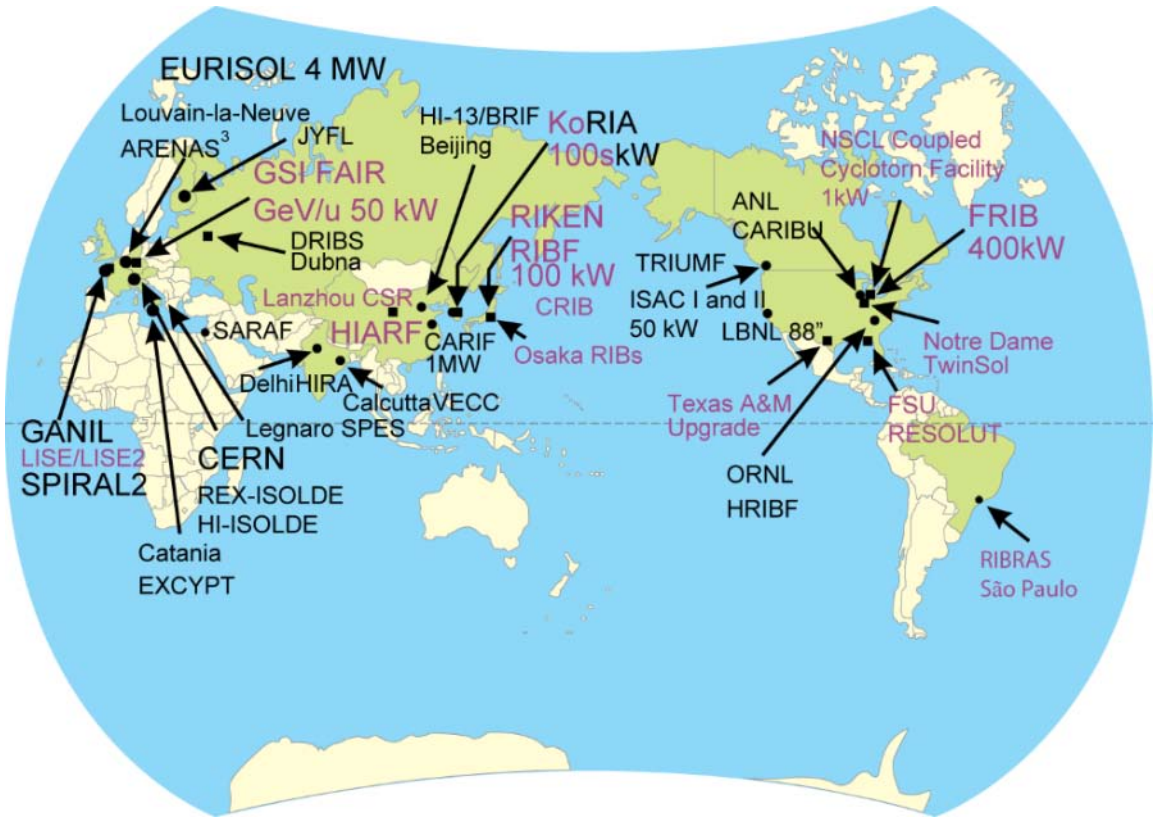

Figure 2: Rare isotope facilities throughout the world, with some of the most powerful new in-flight facilities in development at FRIB, RIKEN, KoRIA, and GSI. The magenta colored laboratories are based on in-flight production and the black labels indicate ISOL production.

1.3 Relevance of this work

Our goal was to characterize ^{238}U fission fragments generated at the 81 MeV/u, which corresponds to close to the highest energies attainable at the Coupled Cyclotron Facility at the NSCL. This beam energy allows us to fill in an energy gap between previous experiments at GSI and RIKEN at 1 GeV/u and 345 MeV/u respectively and fission induced by thermal

neutrons. The lower-energy measurements are particularly important because the FRIB facility will initially use 200 MeV/u uranium for production, which also lies in this energy gap. Our experiments would, in principle, also demonstrate that studies using in-flight fission can be successfully carried out at NSCL beam energies. This would open up the possibility for a range of new experiments at the current NSCL.

The primary motivation for the dissertation was to examine the production cross sections for the fission fragments generated in the fragmentation-fission (often referred to as abrasion-fission) reaction, fission induced by abrading nucleons from a heavy nucleus, and measure the momentum distributions of the resulting fission fragments. This will allow us to test how well the process of in-flight fission production and separation is modeled in the LISE++ code. Understanding how the cross sections vary with beam energy as well as mapping the momentum distributions of fission fragments will allow refinement of existing LISE++ fission models. This would be significant since it would provide a more complete profile of what is actually possible to observe in fission. It is especially important to understand the production of the neutron-rich fragments relevant to the astronomical "r-process", which are believed to be central to understanding the synthesis of more than half of the isotopes heavier than iron found in nature. As a side benefit of the specific particle identification method used in this work, we expect to be able to identify a large number of microsecond lifetime isomeric states that have been previously unobserved. These states are particularly significant for nuclear structure studies since they directly indicate specific excited states in a nucleus that may be difficult to study by any other method. In fact the experiments described here were the first at NSCL to use gamma-rays from isomeric decay to uniquely identify the fragments produced in the A1900.

Perhaps one of the most important benefits from conducting this experiment is the ability to examine the technical challenges of creating secondary beams from fission fragments firsthand and to be able to apply these lessons at NSCL and in designing the next generation facilities. The FRIB facility is designed to begin operation at a much lower energy than the facilities at RIKEN and GSI so the results from this experiment will allow greater refinement in the facility design, specifically in the areas of charge state population and ion transmission. Since fission products fill a large phase space, especially at lower energies, it is essential to know how well existing models predict ion transmission through magnetic systems. Successful identification of fission fragments produced in this experiment will also open up the possibility of using fission to produce secondary beams at the NSCL with the existing configuration.

1.4 Experimental Overview

In order to achieve these goals, we drew upon previous fission experiments for inspiration and designed an experiment compatible with the existing facilities at the NSCL. An inverse kinematic setup was used since it had been shown to successfully produce a number of neutron rich isotopes and was possible to perform at the NSCL where fragmentation based inverse kinematic experiments had been done successfully for many years.

To ensure sufficient beam intensity to create a substantial number of fragments we selected a primary beam of ^{238}U, which emerged from the coupled cyclotrons at an energy of 81 MeV/u. This energy is below, but closer to the FRIB production energy of 200 MeV/u then previous low-energy work. The primary beam needs to be both have a low fission barrier so

that it fissions with a relatively high probability as well as be stable enough that large quantities of it are readily available as well as reasonably priced. ^{238}U fits these criteria for several reasons. It has the highest N/Z ratio of possible primary beam isotopes. This is significant because the fission reaction is expected to roughly preserve the initial N/Z ratio in the fragments [Lov01]. Hence ^{238}U fission can be expected to create a large number of extremely neutron rich products. The fragmentation of ^{238}U allows for the creation of a wide range of high Z fragments that could not be produced any other way. It has been used successfully at GSI and RIKEN in studies of fission fragments and is predicted to be the best beam to produce 30% of expected FRIB products [Hau11]. However, ^{238}U creates a number of problems due to stripper foil lifetimes and losses due to charge states in the stripping process that make it difficult to create an intense primary beam. Despite this it remains the best option.

This beam impacted a ^{9}Be target in which a portion of the primary beam collided and initiated a fission reaction. The fission fragments then flew into the A1900 spectrometer system where they were identified and counted based upon their specific mass, atomic charge, ionic charge state, and momentum. The momentum distribution for each fragment was then measured by scanning the A1900 so that it would record the yield of fragments across the full production range of rigidity. Once the complete distributions were measured the total production for each isotope was calculated by using the LISE++ code [Tar08] to estimate the losses in transmitting the fragment to the detection system. These corrected isotope yields were then integrated to give a total yield, which in turn was compared to the physical specifications of the reacting system to give production probabilities, or reaction cross sections.

1.5 Dissertation Outline

This dissertation will describe the design, setup and results of the experiment designed to achieve the goals described above. The dissertation will begin with the theoretical underpinnings and historical context of isotope production by in-flight fission and will look into the previous work in this field and the lessons learned from them. We will describe the current experiment and provide detail the experimental design and the reasoning behind it. After this follows a discussion of the data collection methods used and how the raw data was compiled into meaningful results. The resultant data will then be examined and compared to theoretical predictions along with making a comparison to results from previous work. Finally, we will summarize the significance of the results as well as discuss methods by which future experiments of this type could be improved.

2. Methods of Rare Isotope Beam Production and Modeling Tools

In this chapter we will review the methods of rare isotope production in order to provide a context for the fisson studies carried out as part of this dissertation. A brief (and not complete) review of past work to illustrate the use of fission will be given, followed by a description of the tools used to model rare isotope production (primarily LISE++ [Tar08])

2.1 Production Methods

As noted in the introduction, there are two main methods for production of rare isotope beams, in-target, ISOL, and in-flight. In this dissertation the in-flight technique of production and separation by fission of a uranium beam is described. In-flight separation based on fragmentation (including fragmentation-fission) consists of the interaction of a heavy-ion beam at between about 50 MeV/u and 2000 MeV/u (or higher) with a target. The beam particles are broken up and the fragments continue forward with nearly the original beam velocity. A magnetic device separates the rare isotopes of interest and the resulting beams used for experiments.

The in-target method normally consists of bombarding a stationary target nucleus with light-ions (such as protons) or neutrons, heating the target to allow the isotopes to escape. They can subsequently be ionized and accelerated. This technique is referred to as Isotope Separation

on-Line (ISOL). It is not the subject of this thesis, but it can use the fission process for the production of rare isotopes. In this regard the cross sections and fission models described later in this thesis are of interest.

Approximately half of modern rare isotope research uses in-flight separation to create a secondary isotope beam [Schwar09]. This technique has proven hugely successful in creating relatively high purity beams of rare isotopes for experiments. The effectiveness of this technique depends primarily on the production probabilities (cross sections) for the isotopes of interest. Since fragmentation reactions consist of knocking off a small portion of another nucleus to generate a rare isotope, as seen in Figure 3 it is largely constrained by the primary beams available [Mor80]. In general, primary beams must be based upon stable or extremely long lived isotopes that can be stored long enough to be useful in generating a beam of sufficient intensity.

Advances in accelerator technology have allowed the acceleration of heavier primary beams, such as ^{208}Pb or ^{238}U, in the energy regime where fission becomes possible [Sch94]. With a heavier beam two types of induced fission reactions become possible: Coulomb excitation from passing close to a heavy target nucleus or fragmentation into a lighter, but still heavy nucleus at high excitation energy that undergoes fission. For the purposes of secondary beam production the abrasion-fission reaction, shown schematically in Figure 3, is preferable due to the light target having more atoms (and hence a higher probability of the beam particle undergoing a reaction) per unit volume.

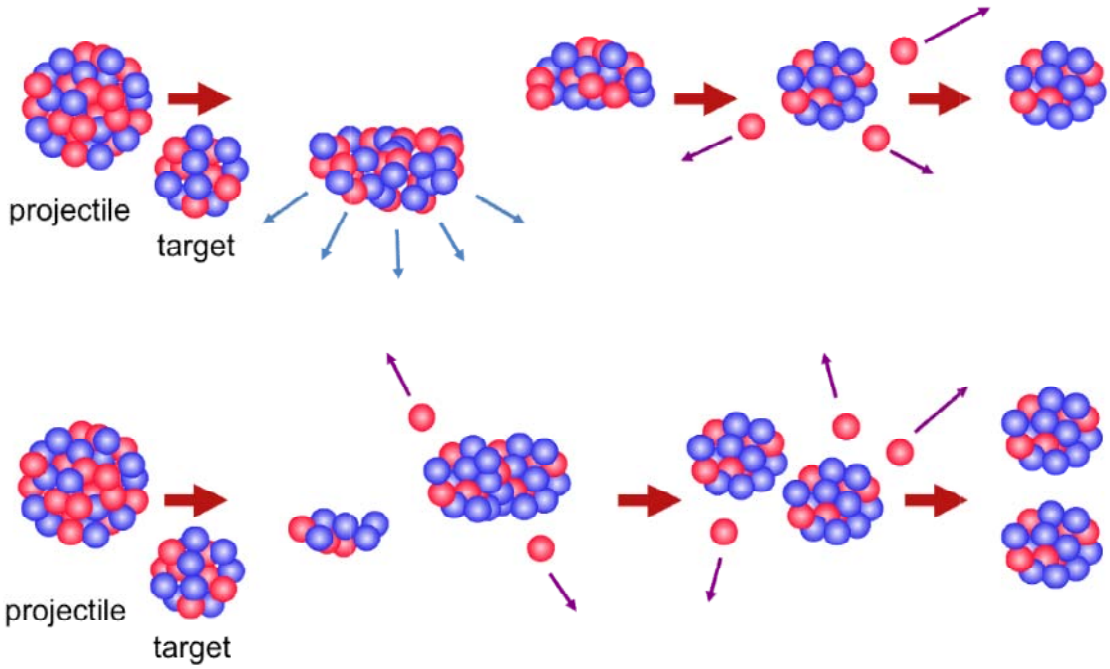

Figure 3 (Top) Pictorial representation of a projectile fragmentation reaction. Note that part of the initial isotope is removed by collision with the target and the remainder continues on essentially unimpeded. Afterwards it deexcites by emission particles or gamma-rays.
(Bottom) Pictorial representation of a fragmentation-fission reaction. The initial part of the reaction is the fragmentation reaction (top) but the deexcitation is carried out through a sequence of neutron emission, fission, and then more neutron emission.

The primary advantage of using fission to produce rare isotopes is that it produces a pair of medium mass fragments that tend to preserve the initial proton to neutron ratio. Taking into account that the heavy, fissile isotopes have significantly more neutrons than protons (relative to mid-mass nuclei), these medium mass fragments are neutron-rich relative to stability. Due to this, for a wide range of neutron number, this technique will likely produce the highest yields. Very far from stability it is possible that fragmentation could be better due to production of fragments at lower excitation energy, or by secondary reactions that produce tertiary products [Sher11]. A significant downside of using fission as a secondary beam production process is that the reaction produces a much wider angular and momentum distribution of fragments and due to

the kinematics of the fission process (more on this later) and hence a much less efficient collection of fission fragments.

2.2 Review of in-flight fission experiments

Pioneering work in using an inverse kinematic setup for studying fission was carried out at GSI in 1994 [Ber94]. These studies were motivated by several advantages over past fission studies. Using a high-energy beam contracts the distribution of fragments in angle and momentum allowing for efficient collection in detectors. This setup also allows for the use of a fragment separator for particle identification purposes, which as will be shown in the analysis section can conclusively determine the mass, nuclear charge, atomic charge and momentum of a fragment. This was one of the first times that the A and Z of fission products could be identified ion by ion and the fission isotopic yields mapped in detail [Sch94]. While this work was hugely successful in producing and identifying over 1000 isotopes including 120 new ones [Enq99], technical limitations due to a relatively weak primary beam limited what could be done.

A series of experiments at several facilities worldwide followed the initial work done at GSI to both examine production characteristics of different targets and to study the properties of the induced fission reaction. Following on the 1994 success, in 1995 research at GSI examined how the fission decay channel contributes to fragment production from ^{238}U [Cle95] and made the first identification of ^{78}Ni [Eng95] using the fragmentation fission reaction. Studies of the reaction cross sections were made in 1996 [Hes96] along with measuring the charge distribution between the fission fragments [Arm96] using both Coulomb and fragmentation fission. In 1997

work was done at the NSCL to develop secondary beams using fission as a production mechanism [Soul97] along with the measurement of several cross sections using a lead target. Major work on cross section measurement using lead and beryllium targets was published in 1998 [Donz98][Ber98] which led to the creation a model that formed the basis of the cross section model used in the code LISE++ [Ben98] as well as work studying the shell effects on fission [Sch98]. Velocity distributions were measured for Coulomb fission fragments the following year [Enq99]. More recent work by Bernas has utilized a proton target to measure cross sections and explore the conditions for symmetric and asymmetric fission [Ber03][Ber06]]. Recently, during the commissioning of the new BigRIPS separator, RIKEN has established techniques to produce and identify fission fragments as well as identify several new isotopes due to the enhanced primary ^{238}U beam rate available in their new facility [Ohn08][Ohn10].

Currently, various in-flight fragmentation facilities have proposed and designed new upgrades (primarily based on higher primary ^{238}U beam intensity) that would allow them to take advantage of the rare isotope production potential of the fission reaction. During the course of this design work several models of the fission reaction were proposed based on the GSI data and these were then in turn built into simulation codes, such as LISE++, that were used during the development of the new facilities.

2.3 LISE++ code

The implementation of in-flight fission at a facility such as FRIB is one of the technical challenges that must be addressed. The application requires an understanding of the production

mechanism and the knowledge of cross sections for what will be produced. While theory predicts that fission can produce extremely neutron-rich exotic isotopes, studies are still needed to verify the predictions and demonstrate that the isotopes can be identified and separated. In order to take advantage of the isotopes created in the fission reaction there has been a push to study in-flight fission and model it. Critical to the design of new rare isotopes facilities and the planning of experiments is the accuracy of modeling software. One of the primary tools in this area is the LISE++ code [Tar08].

LISE++ is a multi-component simulation code designed to assist experimentors from the initial design stage all the way to predicting the data output, including simulation of particle identification plots from actual detector systems [Tar08]. The code has integrated the capabilities of many different specialized routines including those for ion optics [Brown80], energy loss in material [Lin96], atomic charge states of ions [Scheid98], fragment de-excitation [Tar03], and a large selection of possible production mechanisms [Tar08]. The code is capable of both Monte Carlo particle tracking and high speed analytic calculations. These calculations include a variety of production mechanisms including, fragmentation, fusion-fission, Coulomb induced fission, and fragmentation fission. The ion optics code for transmission allow for the use of fifth-order transmission matrices in a blockwise construction allowing the user to quickly add and remove components from the beamline to match a particular experimental setup with matrices imported from another code such as COSY INFINITY [Berz93]. The parameters in these models can be edited by the user allowing for even more flexibility in simulating a particular experiment. It is the very flexibility of this code however that necessitates experiments to confirm the models. The vast majority of the data available for Coulomb and fragmentation fission came from the series of GSI experiments run by Schmidt et al. [Sch00],

although recently new data has become available at RIKEN [Ohn08]. Since previous experiments have shown that the production cross sections in fission vary with the energy of the primary beam and the selection of target material. In order to utilize this code and codes like it then, experiments such as the current work are needed to further refine the models and their parameters to allow for better simulations.

In order to demonstrate the output of the LISE++ code, Figure 4 is an example of an energy loss versus time of flight simulation using the LISE++ default settings for the reaction of 81 MeV/u ^{238}U with ^{9}Be. The settings used to generate these plots correspond to those of part of the experiment aimed at identifying new isotopes, as described in the later chapters and the detector systems used to measure energy loss and time-of-flight are described in chapter 5. Figure 4 illustrates the two modes used by LISE++ to graphically describe expected results for a particular experimental configuration. The bottom panel was produced by a Monte Carlo simulation taking into account the production cross sections and beam line transmission. The top panel uses the same parameters but with the faster analytical method. The bottom panel is more representative of what would actually be seen using our experimental setup while the top panel provides a simpler schematic representation that is useful for planning purposes where many different settings need to be tried quickly.

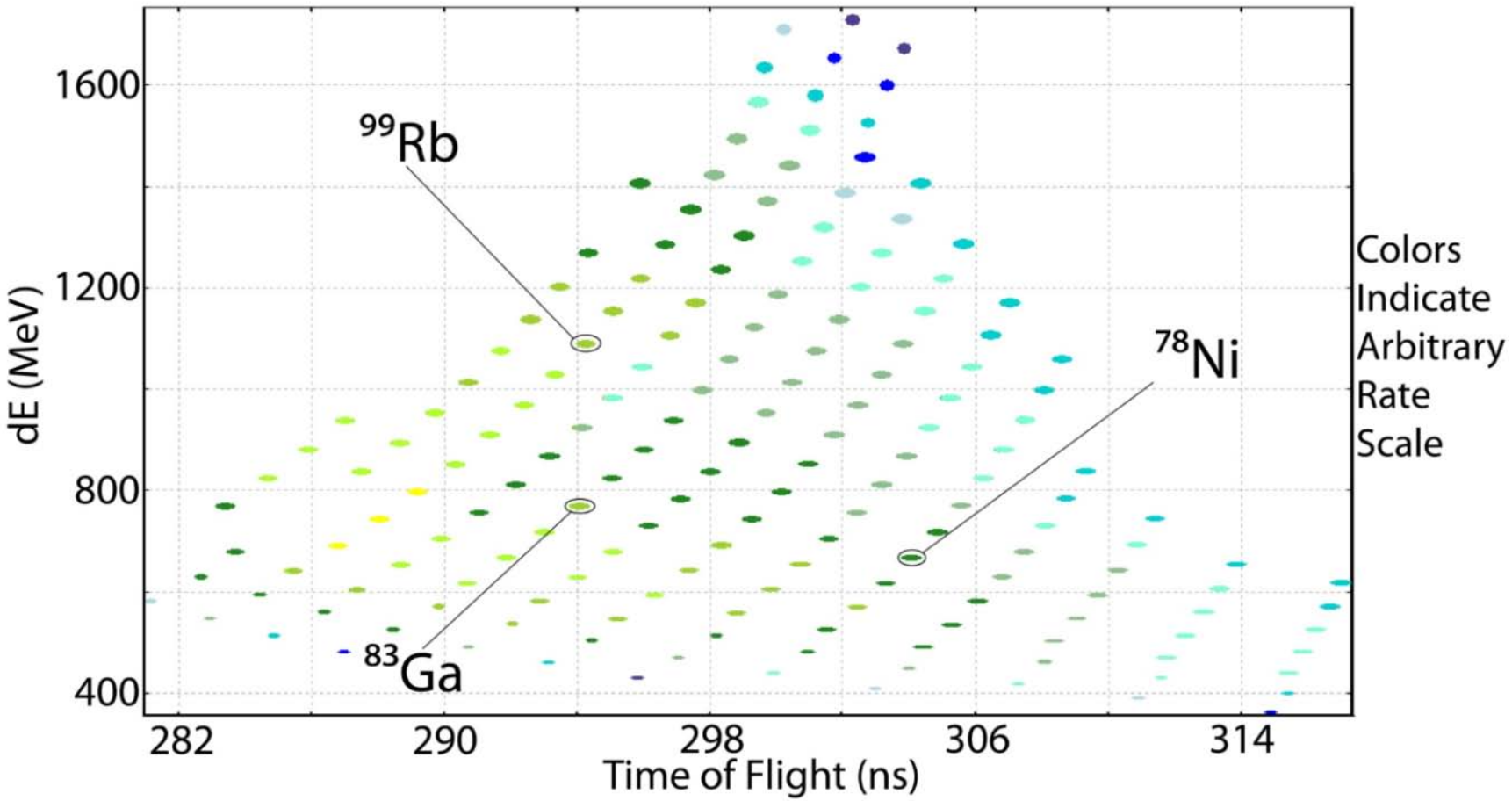

Figure 4: Sample LISE++ Calculations of Energy loss vs. Time of Flight for fragments in the A1900 from Abrasion Fission using both analytical and Monte Carlo calculation methods, simulating a typical particle identification plot. The system configuration was that of setting 1118 with the reaction of 81 MeV/u ^{238}U with ^{9}Be as described in Chapter 5.

Figure 4. (Cont'd)

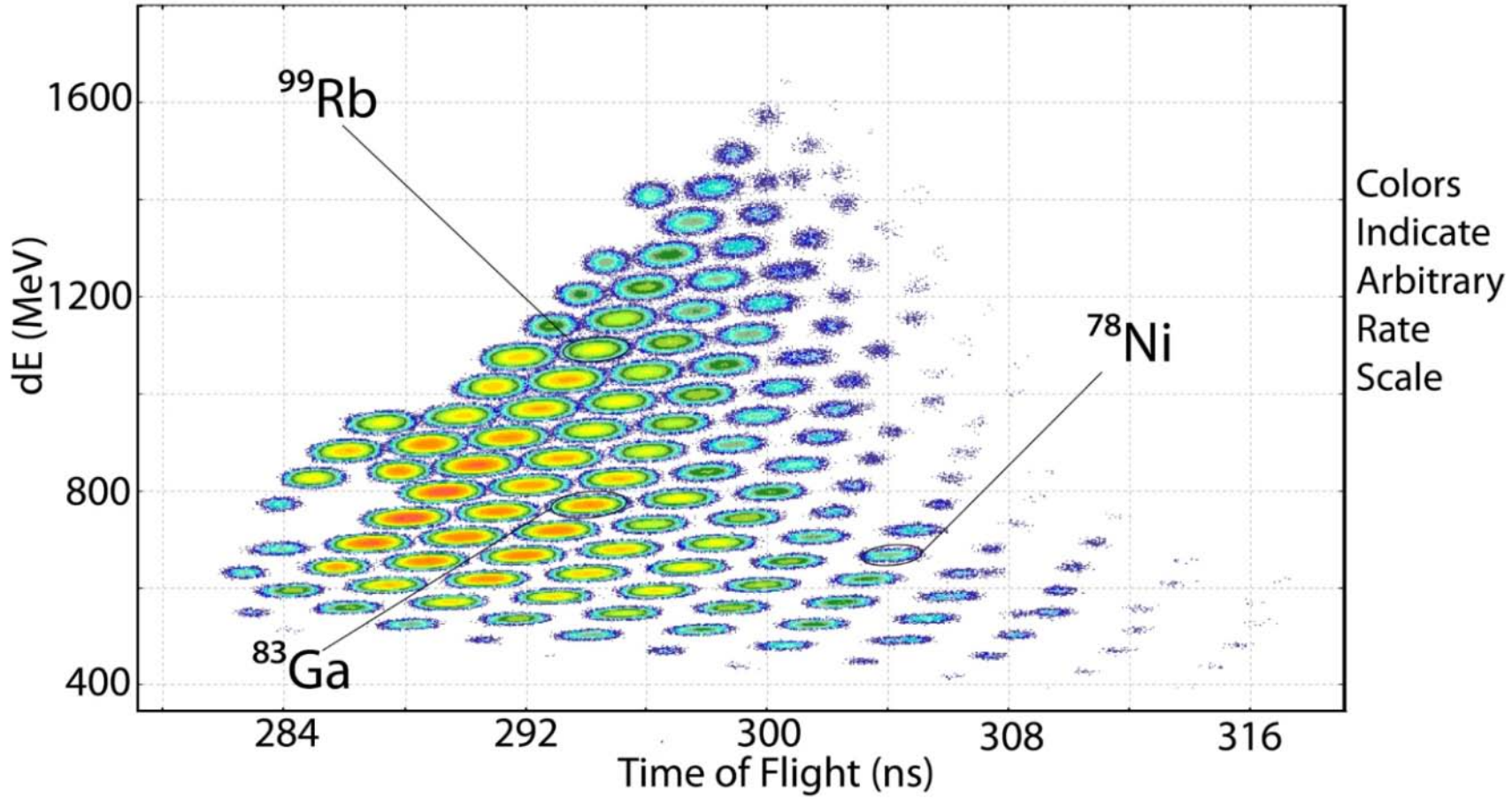

2.4 LISE++ Abrasion Fission

Specifically in this dissertation, we will describe the abrasion-fission portion of the LISE++ simulation code developed by Tarasov and Bazin [Tar08]. Computationally, fragmentation fission is one of the most difficult to model due to the large number of steps in the process. The fragmentation-fission reaction takes place in three phases, the initial fragmentation reaction, the subsequent fission, and the decay into the (longer-lived) fragment that makes it to the detector (as was shown in Figure 3 above). Each fragmentation reaction of the ^{238}U beam has a large range of possible products, which can then fission into an even larger range of products and subsequently decay with some probability to a number of final products. Generation of a complete map of all possible routes for each final fragment would result LISE++ being too slow for effective simulation of the various experimental conditions. Therefore, in order to allow for reasonably fast calculations, simplifying assumptions have to be made. The LISE++ abrasion-fission model is based on the assumption that every initial primary beam particle that interacts leads to one of only three possible fragmentation products representing low medium and high excitation energies (with probabilities chosen by predefined weighting factors). The representative prefragment for each excitation energy is selected based upon the fragmentation cross sections of ^{238}U and a user selection of what excitation energies qualify as low, medium, and high. The fission cross section for each isotope is created using a weighted sum of the fission cross sections from each of the prefragments. Figure 5 illustrates the cross section distributions used by LISE++ for the prefragments ^{236}U, ^{229}Ac, ^{214}Po and total cross

section taken to be 1300 mb with excitation energies of 23.4 MeV, 96.6 MeV, 287.9 MeV respectively.

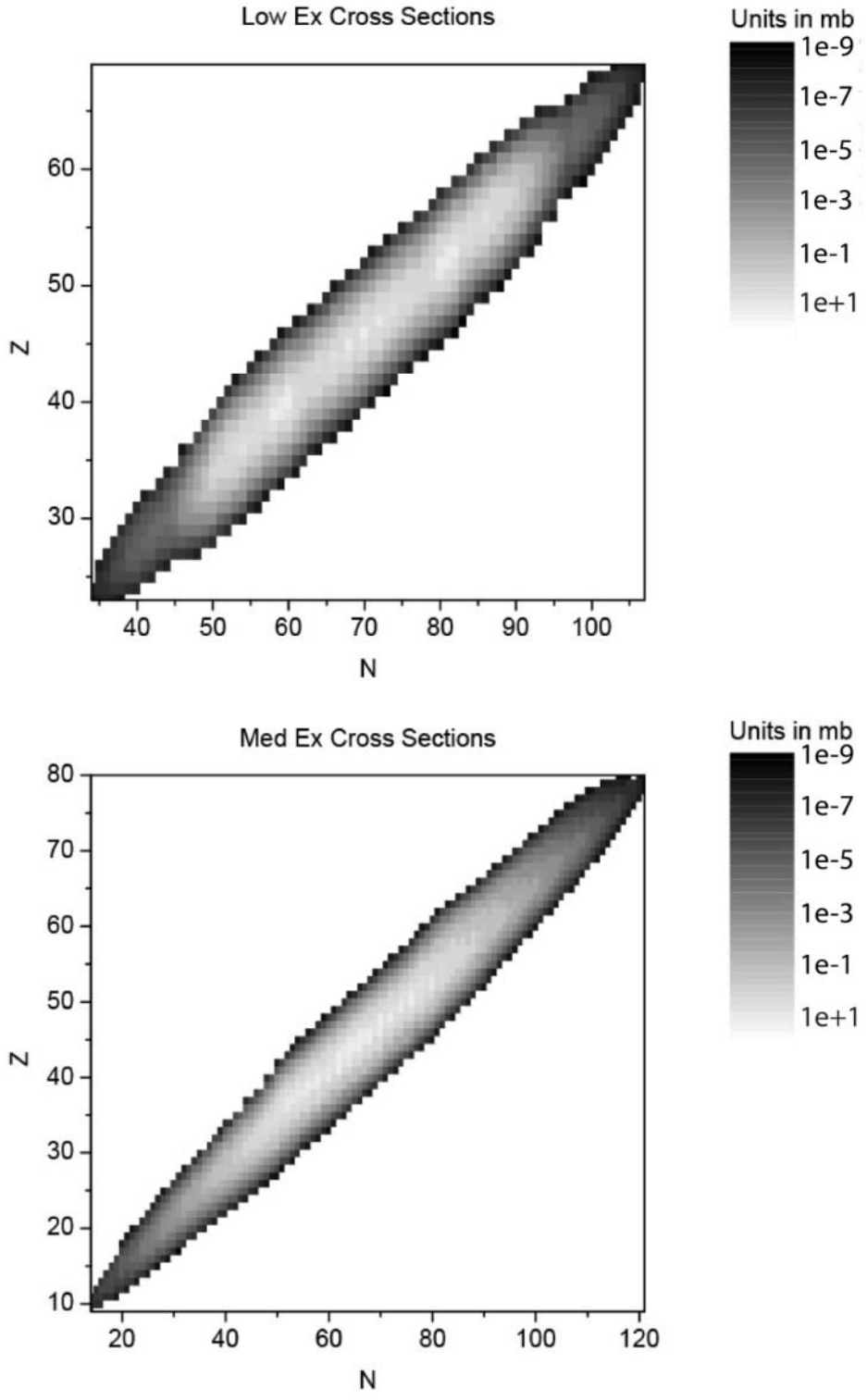

Figure 5 LISE++ Calculated fission prefragment cross sections of ^{238}U on ^{9}Be. Predictions are made for each of three excitation regimes with the summed total cross sections shown for each isotope.

Figure 5 (Cont'd)

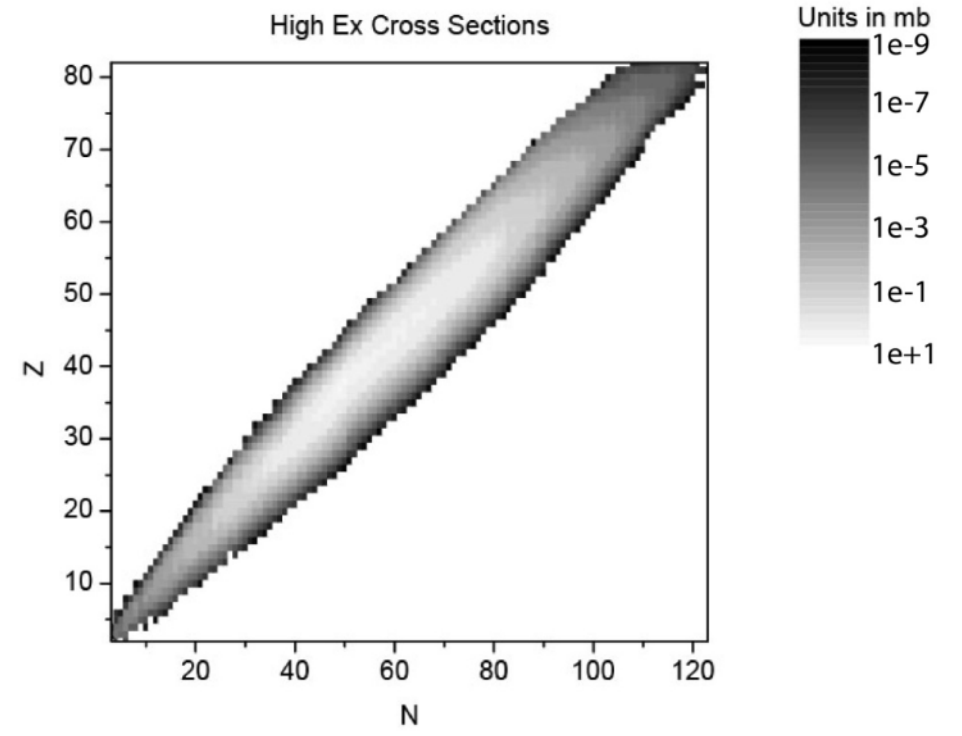

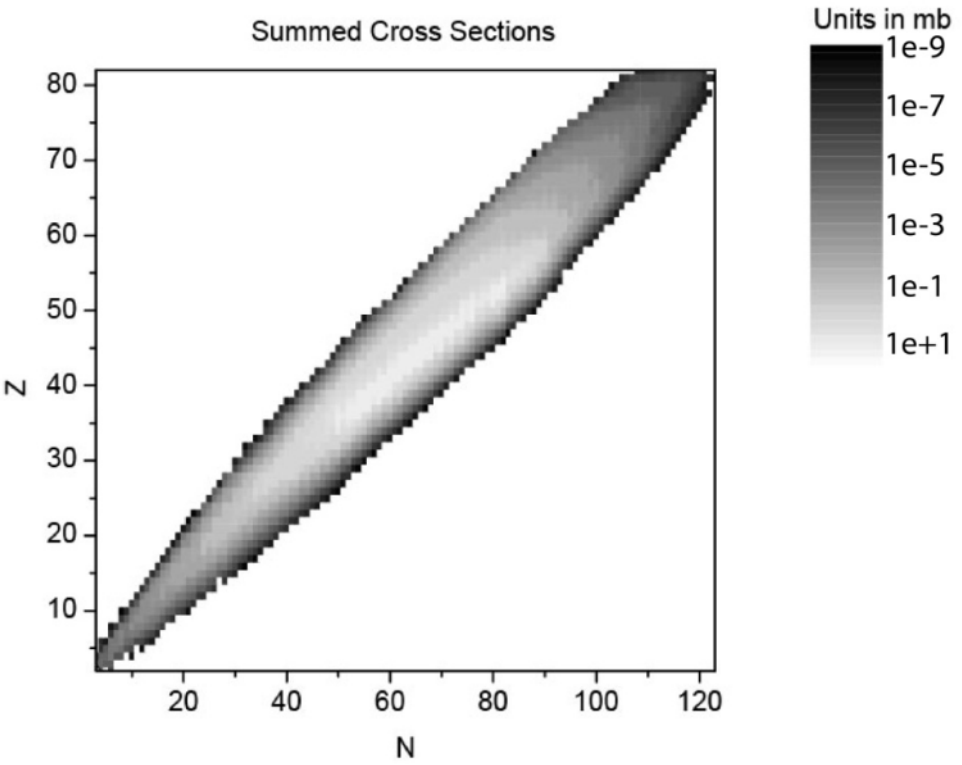

Once the initial fragments are determined then the code examines several decay possibilities. These can be selected by the user in order to avoid wasting processing power on calculating decay processes not expected to contribute to the final isotope production. The code then selects the fragments in the fission channel and calculates the fission fragment distribution for each of the three fragmentation products. The distributions are described using a potential barrier defined by Cohen [Coh74] with shell corrections from Benlliure et. al. [Ben98] giving a selection of fission products based upon the initial excitation energy of the fissioning nuclei and shell structure correction. We will address this model in more detail in the following section. After the fission products are determined the excitation energy is assigned to them based upon the initial fragment internal excitation and the energy released in the reaction. This assignment follows the prescription of Faust [Fau02] giving the final values of center-of-mass kinetic and internal excitation energies for each fission fragment pair. In accordance with accepted theory, the fission fragments are assigned to a spherically symmetric angular distribution in the center of mass frame, as illustrated in Figure 27.

Once the fragments and their internal excitation energies are determined, de-excitation processes are calculated for each fragment. This primarily consists of prompt neutron emission resulting in a decrease of mass and excitation energy of the fragment. The fragment's momentum is then convoluted with a Gaussian distribution to account for the change in fragment momentum during the evaporation process which assumes no preferential emission direction in the center of mass frame. Once the momentum distribution, charge, and mass have been determined for the final fragments they are converted into the laboratory frame where they are fed into an ion optical model of the separator. This model describes the operating conditions of the experiment with up to fifth-order matrices to account for transmission. Finally the code

outputs the expected results of the experiment based upon which of the initial fragments are expected to be transmitted through the experimental setup. The specifics of the fragment transmission calculations will be discussed in a later section.

2.5 Experimental Observables

An important goal is to understand the various steps in the fragmentation and fission process. This is needed in order to be able to model fragmentation-fission for planning of experiments at places like NSCL and FRIB.

Table 1 lists the various model parameters and the experimental methods that might be used to refine them. As can be seen in the table each of the factors is related to these observables and hence a unique extraction of model parameters is difficult. However, it is also clear that one of the most critical aspects is the ability to measure the differential cross sections (momentum distributions) of the fission fragments. Previous experiments at GSI and RIKEN have not attempted to extract this information. The table lists a number of additional experiments that could be done to reduce the uncertainties, but these are outside the scope of this work.

The corresponding parameters used in the LISE++ abrasion-fission model and the values adopted for this dissertation are shown in Table 2. These values correspond to the default values assigned within the code. The values depend on the beam energy and the target and were set for the beam energy of 81 MeV/u and a ^{9}Be target.

Table 1: List of the model parameters, and the experimental observables that might be used to determine them. Some of these methods will be used in this thesis to test the models.

Fission Model Factor	Method to Observe Experimentally
Prefragment fissile nuclei (Currently three chosen) Cross Section	• Measurement of fragmentation cross sections by observation fragmentation products; not measured in this experiment, and would require a model for the ratio of fission probability to neutron emission • Cross sections of fission fragments; with other parts of the fission model determined one could infer what the original distributions should have looked like. • Momentum distribution of fission fragments; higher excitation energy in the prefragment would yield a broader momentum distribution
Prefission Fragment Excitation Energy	• Examination of the length of evaporation channels after the excitation reaction; difficult to directly measure but may be implied from cross sections • Observation of momentum distributions; This requires knowledge of the distribution of energy between internal excitation and kinetic energy and the fission reaction Q-value • Observe the centroid of the momentum distribution to infer how much energy was dissipated in the initial collision; this would require a detailed knowledge of the pre-fission fragment distribution and a model dependent unfolding.
Fission Energy Distribution Between TKE and Internal Excitation	• Measure TKE of fission fragments with known fissioning nucleus; The energy input into the system must be determined somehow as well as the fission Q value of the reaction
Fission Barrier Model and Shell Correction	• Relate the total reaction cross section to the energy induced to the nucleus prior to reaction • Examine the production cross sections of the products to determine which are more favorable
Deexcitiation Channels of fission Fragments	• Measure the total reaction cross section • Collect reaction fragments and use their identification and kinematic propertied to determine their originating reaction

Table 2: Parameters used in the LISE++ abrasion-fission model and the values adopted for this analysis.

LISE++ Parameter Name	Values used in this analysis
Three representative fragmentation products with (low, middle, and high excitation energy)	^{236}U, ^{229}Ac, ^{214}Po; total cross section taken to be 1300 mb
Assumed average excitation energy of prefission fragment (Low, middle, high)	23.4 MeV, 96.6 MeV, 287.9 MeV; taken from the parameterized Gaussian distribution with parameters taken from [Sch02]
Fragment Excitation TXE	Reaction Q-value [Fau02]
Fragment Mass Distributions	Taken from [Ben98]
Fragment Excitation Energy, standard deviation of distribution	5.5 MeV

3. Experimental Setup

This chapter will describe the specifics of the experimental setup and the reasoning behind the particular design decisions. We will first provide a brief overview of the experimental procedure and then look at each component of the experiment in some detail to clarify its purpose and necessity.

In the introductory section we discussed why ^{238}U was the best choice for the primary beam. At beam energy over 50 MeV/u the main reaction mechanisms of ^{238}U breakup are fragmentation and fission. Fission can be induced by nuclear or Coulomb excitation. As discussed previously, we believe that the Coulomb fission mechanism is better understood, so in this thesis we will focus solely on fragmentation fission. The target material, Be, was chosen to induce fragmentation fission (as opposed to Coulomb fission that would be induced by a higher-Z target) and the thicknesses were chosen for reasons described below.

We will describe how the existing A1900 fragment separator was used to determine an ion-by-ion identification of the fragment mass, momentum, atomic and nuclear charges in Chapter 4. Particles are identified by Bρ (which provides information on mass, velocity, and charge state), time of flight (which is related to velocity and mass), energy loss (which determines atomic number), total energy (which depends on mass and velocity). The four measured quantities allow the four properties to be inferred. Detectors must be able to measure the quantities to a precision needed to get unit A, Z and Q resolution. Finally we will examine

the specific detector configuration used for this work and how it measure the parameters required for the particle identification.

3.1 Beam Source

The beam was generated in an Electron Cyclotron Resonance (ECR) ion source and transmitted to the K500 Cyclotron. The $^{238}U^{30+}$ beam was then accelerated to an energy of 7.68 MeV/U and stripped to a charge state of 80+. This beam was then transmitted to the K1200 cyclotron where it was accelerated again to 81 MeV/u and a charge state of 80+ and transmitted to the target box. Full details about this system are described in [Ant94].

The ions generated in the source were fed into the coupled cyclotron, K500-K1200, system, shown in Figure 6. The system was set to accelerate the 69+ ion charge state in the K1200 to a beam energy of nominally 81 MeV/u. The ions were then extracted from the K1200 with a small angular emittance. The intensity of the beam is controlled by an attenuation system in the ECR beam line allowing for selection of rate without adjusting the cyclotrons themselves. The maximum intensity was determined by the limits of the life time of the stripper foils. The high mass and charge of the ^{238}U caused the foils to typically last only one hour at 1 pnA. The stripper holder could only have at most 31 foils [Bon01] meaning that running a beam over 1 pnA would be inadvisable for any experiment expected to last over a day due to the time lost in changing the foils. Details on the K500-K1200 coupled cyclotron system can be found at reference [Mor97].

3.2 A1900 Spectrometer

Particle identification and counting was done using the A1900 separator/spectrometer [Mor03] shown in Figure 6. On the most basic level the A1900 uses the Lorentz force on a moving charged particle in a magnetic field to separate different fragments. The A1900 consists of a set of four dipole magnets each having a uniform magnetic field that define the geometry of the beamline and a series of quadrupoles for focusing. Each dipole bends the fragments relative to one another by taking advantage of the fact that fragments with differing momentum to charge ratios have a different radius of curvature within a uniform field. Since fragments with a different magnetic rigidity experience a different force when passing through the dipoles, two fragments with identical initial positions but different rigidities exit the dipoles with a spatial separation between them. The maximum physical separation occurs after the second dipole where the particle paths become parallel to one another. At this position it is possible to easily measure the magnetic rigidity of the fragments, or manipulate the beam by placing a detector or block of material in the beam path. A physical slit can be put into the beam path at this position to select a specific range of momenta. This results in limiting the transmitted fragments to those of possessing a specific range of momentum to charge ratios. Placing a degrading block of material in the beamline reduces the fragment momentum based upon the atomic number which in turn allows the second set of dipoles to select fragments based upon the atomic number. An alternate method to identify the momentum per charge, p/q, ratio in cases where beam intensity is low is to place a position sensitive detector in place of the slits in order to record the p/q value without losing any yield. The third and fourth dipoles in the series are mirror images of the first two and serve to reverse the dispersive effects, causing the fragments to refocus at a point after

the fourth dipole. It is at this point that a detection end station can be placed to measure all of the transmitted particles or they can be transmitted to further experimental setups. If there is material placed in the beamline prior to the final dipoles, not all fragments will be focused at the same point, but will be dispersed according to A and Q (Z). For the present work, since we were attempting to measure as many isotopes as possible, is was necessary to scan the field strengths of the final dipoles in order to observe the entire group of fragments transmitted through the first two.

In order to determine the actual total number of fragments produced it is necessary to take into account the angular and momentum acceptance limitations of the A1900. While in-flight fission the fragments are produced in a spherically symmetric distribution. After Lorentz boosting them into the lab frame they are still left with a fairly broad angular spread. The A1900 cannot accept this entire spread simultaneously and instead can only accept a cone with a solid angle of 10 msr centered on the central axis. The resulting distribution would resemble Figure 26, below, after the system has been scanned over all momentum/charge values. The detection system can only handle about 1000 cps before signal pileup begins to cause dead time and data is lost which made it necessary to control the beam intensity as noted in the previous section to control the rate. Because the A1900 is a physical system it differs from the ideal system described above and these differences can affect the fragment transmission and must be accounted for by calculating the acceptances with an ion optics code supplied with the field strength maps measured for the system. These limitations are discussed in detail in Chapter 5.

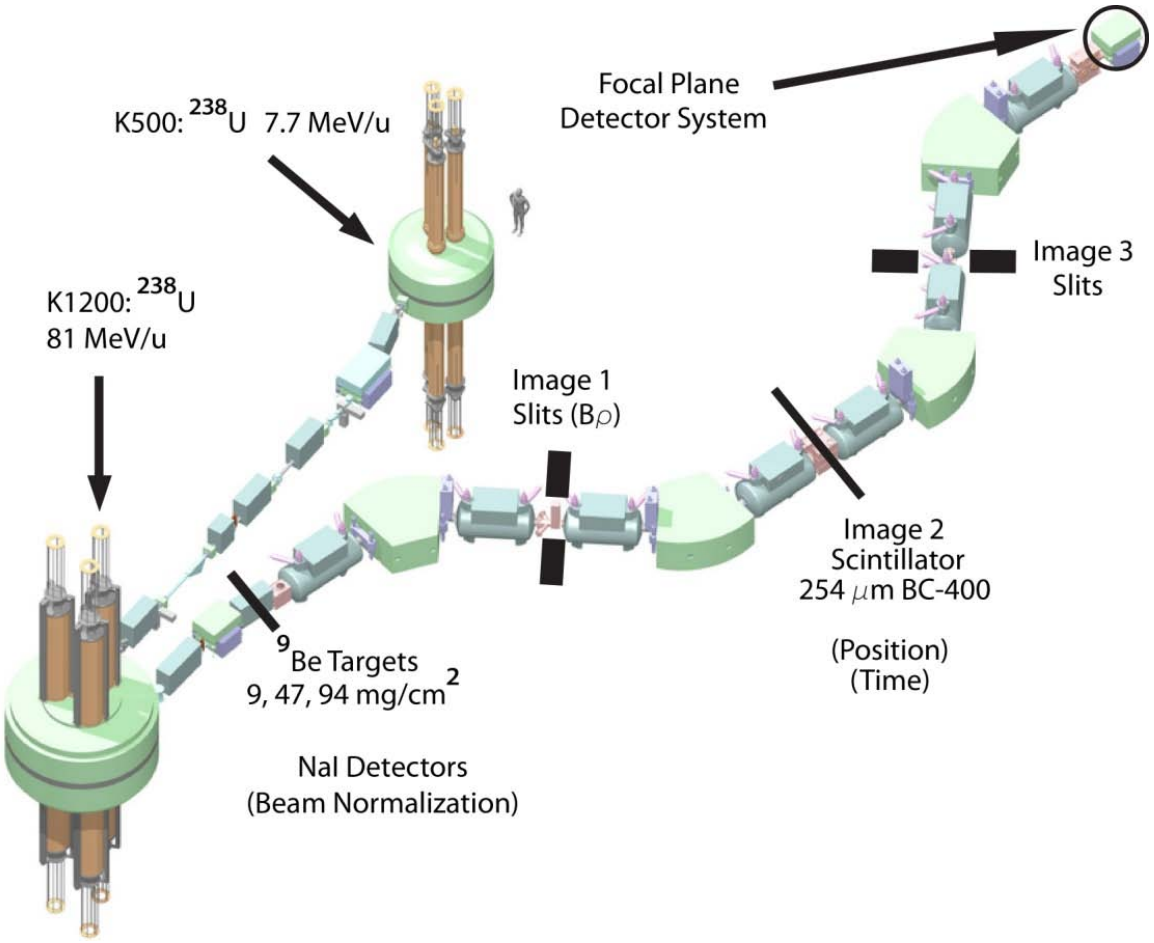

Figure 6. Schematic layout of the A1900 experimental setup. Slits at Image 1 were used to control momentum acceptance. A 254 micron BC-400 scintillator was placed at Image 2 in order to measure the position of fragments at the plane of maximum dispersion, allowing for effective fragment tracking. The focal plane detectors consisted of a Si telescope with 1 x 500 micron detector followed by 4 x 1000 micron detectors used to measure the dE/dx of the fragment as well as stopping it and collecting the total kinetic energy. A Ge detector was placed adjacent to the telescope to record gamma rays emitted from fragments stopped in the stack.

After extraction from the cyclotron the ions were transmitted to a target box at the beginning of the A1900 where one of a set of three targets was placed in the beam path. The targets mounted in the target holder were 9, 47 and 94 mg/cm^2 of ^{9}Be. A small portion of the

ions reacted with the target atoms generating fission reaction products. The beam rate on target was monitored by a set of NaI counting detectors which are sensitive to particles scattered from the target which is assumed to be proportional to the beam intensity. The NaI detectors will be discussed in more detail in the analysis section.

Both the unreacted primary beam and the reacted fragments then passed out of the target into the first set of quadrupole magnets, which serve as collecting lenses, essentially defining the solid angle of the A1900 separator/spectrometer. Then the beam passed into the first dipole of the A1900. In this dipole the fragments were selected by their momentum to ionic charge ratio, with the fragments not meeting this criteria stopped by physical slits placed in the beamline. For most settings the unreacted primary beam was removed here by absorption in a large metal block

Depending on the intensity of the fragments after the first dipole, two operating modes were available. In the first mode the momentum slits were set to a very narrow acceptance (0.1%) which limits the total number of fragments reaching the detectors and removes ambiguity in the fragment momentum identification caused by overlap in momentum distributions between neighboring isotopes of the same element. This is discussed further in the data analysis section. With low intensity fragments, the momentum slits were set to the largest value (5%) which allowed more fragments to be collected but caused some complications in the particle identification process. In order to measure the momentum, a position sensitive detector was placed at the dispersive plane of the spectrometer (described in the next section) to assign a momentum value to each of the particles. The counting rate of the detection system was limited to about 1000 cps before dead time becomes a significant factor giving the limiting criterion for switching between operating modes.

In the second half of the spectrometer the optics were set to focus all of the fragments onto a single point near where the detectors are placed. This allowed measurement of all transmitted fragments simultaneously as long as the rate was low enough for the detection system to handle it (around 1000 particles per second). In the second operating mode the focusing was changed due to the presence of the detector in the beamline meaning that the second section must be scanned across several values to collect all of the isotopes generated.

At the focal point the fragments are stopped and collected in a stack of five Si detectors described in the detector section, which record the amount of energy lost in each layer. Once stopped any isomeric states in the fragments decay by gamma ray emission. If the lifetime of these isomers is less than 10 microseconds they may be observed by a Ge detector placed adjacent to the detector stack.

3.3 Target

In general for isotope production the target would be selected in order to maximize the number of reactions and hence the rate of individual fission fragments. For the purpose of this experiment we used the appropriate target material (^{9}Be), but because we were interested in measurement of momentum distributions we ran individual parts of the experiment with as thin a target as possible to leave the momentum distribution as unaffected from energy loss as possible. For thick targets the specific location within the target where the reaction occurs can have a big impact on the final momentum measured. In very thick targets the broadening of the momentum distributions of the fragments can be so large that it is no longer possible to unambiguously

reconstruct the distribution generated in the reaction. Beryllium was selected as the target material due to the high number of atoms per unit volume and relatively low energy loss, as particles pass through it. This combination gives a high probability of generating a reaction while minimizing energy loss in the target allowing a more accurate measurement of the fragment energies as they were generated in the reaction. As shown in Table 3 below, Be has the highest rate of production for a number of fission fragments as compared to other available target materials for equivalent energy loss target thicknesses. These values were calculated using LISE++ (v9.1.12) default settings and using an incident beam of 81MeV/u $^{238}U^{80+}$. The reaction was assumed to take place in the center of the target with no additional energy assigned to the fragments due to the reaction. A light nucleus, like ^{9}Be, is more conducive to fragmentation-fission than heavier nuclei since it has significantly less charge and will not significantly excite beam nuclei unless they approach close enough for a removal of nucleons by the strong force. There is a small contribution from Coulomb fission, but this is estimated to be below 5% in the default LISE++ code.

Table 3: Comparison of predicted production for a set of representative isotopes using a variety of target materials normalized to a uniform energy loss for the transmitted fragment assuming a reaction at the center of the target.

	Target (mg/cm^2)			Rate (PPS)			Cross Section (mb)		
Fragment	Be	C	Pb	Be	C	Pb	Be	C	Pb
Sn 126	94	85.5	157	2.02E+04	1.41E+04	5.50E+02	17.384	17.159	19.207
Sn 129	94	85.5	157	3.67E+03	2.62E+03	2.32E+02	3.321	3.3717	7.8903
Sn 132	94	85.5	157	2.79E+02	2.02E+02	8.93E+01	0.244124	0.249938	4.211136
Sr 98	94	85.5	157	3.34E+03	2.38E+03	3.04E+02	2.3912	2.4391	9.4085
Sr 100	94	85.5	157	1.47E+02	1.08E+02	5.91E+01	0.10152	0.10327	1.73457
Sr 102	94	85.5	157	4.31E+00	3.05E+00	4.86E-01	0.00272	0.002773	0.014361
Ni 72	94	85.5	157	1.59E+02	1.14E+02	1.15E+01	0.142114	0.147014	0.200901
Ni 74	94	85.5	157	1.68E+01	1.21E+01	1.21E+00	0.013708	0.014318	0.02018
Ni 76	94	85.5	157	6.96E-01	5.14E-01	4.49E-02	0.00056	0.0006	0.000722

Three target thicknesses of Be were chosen for this experiment. The selection of a particular thickness was based on balancing the needs of production rate, preserving the initial momentum distribution, and giving the generated fragments with an equilibrium charge state distribution. A equilibrium charge state distribution is of particular importance to calculate the total transmission through the spectrometer since the A1900 selects fragments based upon their momentum to charge ratio, meaning that any fragments produced at the same momentum but with different ionic charge might be excluded causing a loss in yield. In order to maximize the number of reactions a thick target of 94 mg/cm^2 was chosen when isotope production cross sections were low. This had the downside of introducing changes into the momentum distributions through energy loss and straggling. For cases with a high cross section a thin target of 9 mg/cm^2 was selected in order to minimize the target induced shifts in the momentum distributions. While this gave a clear picture of the distributions, the fragments did not reach an equilibrium charge state in the thin target causing the loss of a significant amount of yield. This was obvious as the distribution of charge states was centered lower and was broader in the 9

mg/cm^2 target compared to the thicker targets discussed below. For most cases the medium target thickness of 47mg/cm^2 was used as a compromise, since it was thick enough to give a more uniform charge state distribution and a greater number of reactions per beam particle than the 9mg/cm^2 target while attempting to reduce the influence of the target on the momentum distributions.

Due to the lower beam energy at the NSCL the fission fragments are produced with a wide range of ionic charge states compared to the previous work at GSI where the beam energy was so high that the fragments were all fully stripped. The extraction of cross sections must include a correction for the loss of intensity due to the distribution of fragments in various charge states. The charge state distributions can be reasonably well predicted using codes such as GLOBAL [Scheid98]. Our data provide a measurement of charge state distributions with high-energy medium and heavy ions not normally available and can be used to check the accuracy of the predictions. For comparison, the charge states of ^{238}U at 81 MeV/u after passing through 9 mg/cm^2 and 47mg/cm^2 of ^{9}Be are shown with the predictions of GLOBAL in Figure 7. The code does well for the thin target but is not very accurate on the thicker target indicating room for improvement in the model. We estimate that generally corrections due to charge state distributions will not be larger than about 2.

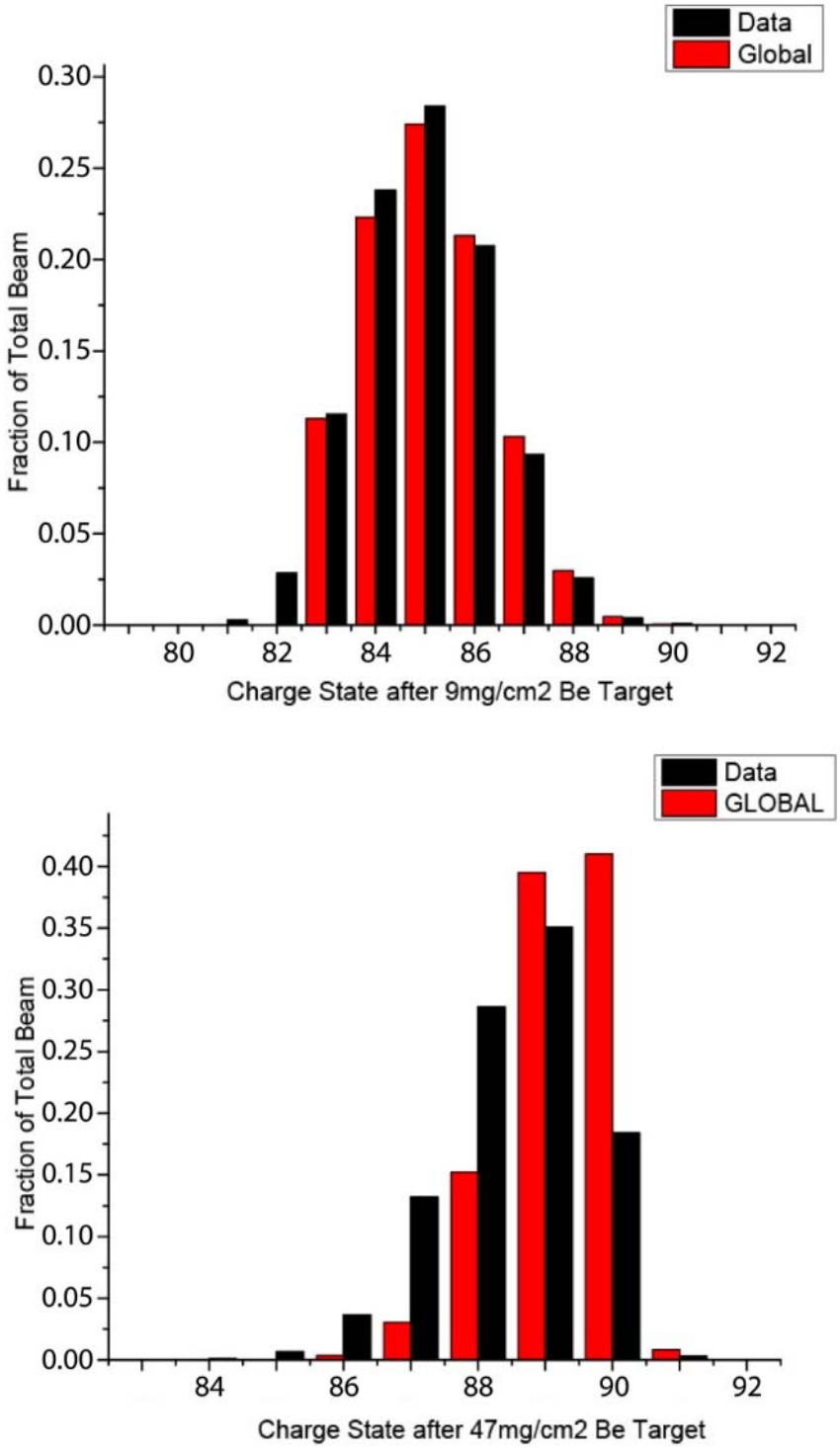

Figure 7: Charge state distributions of a ^{238}U primary beam after passage through the specified ^{9}Be target. These distributions are compared to predictions from the GLOBAL charge state calculation code.

3.4 Detector Systems

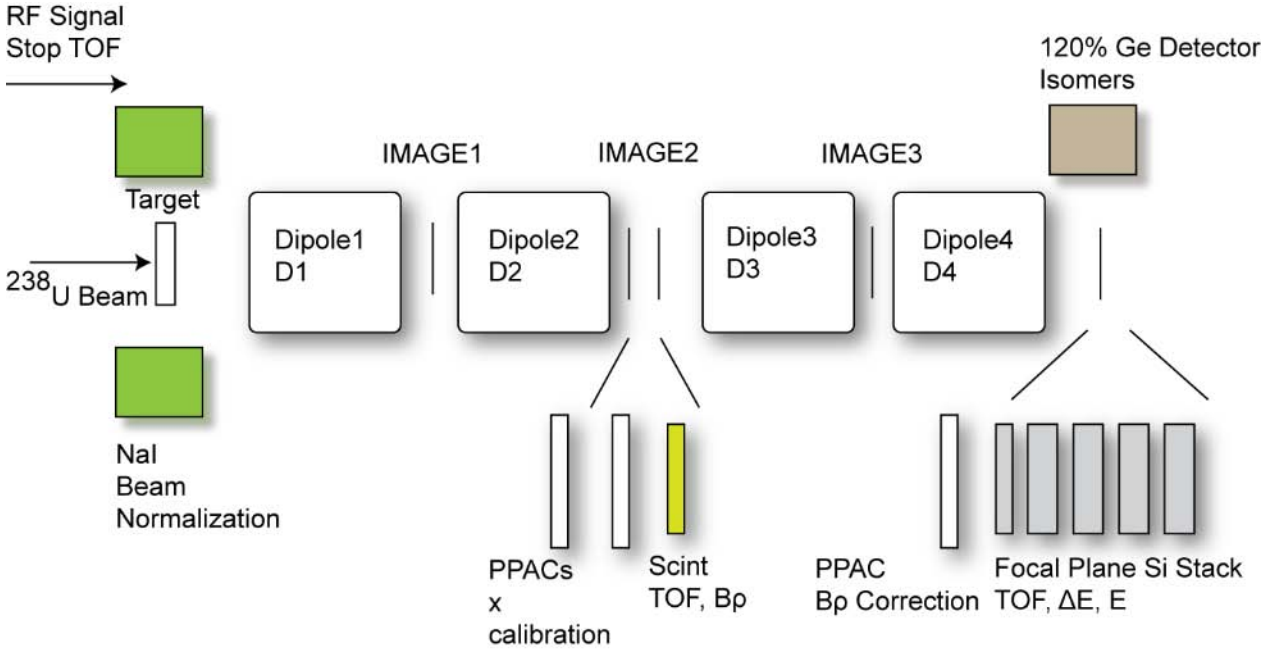

Figure 8: Schematic representation of the A1900 indicating the relative position of the detectors and the signal they contribute to the analysis.

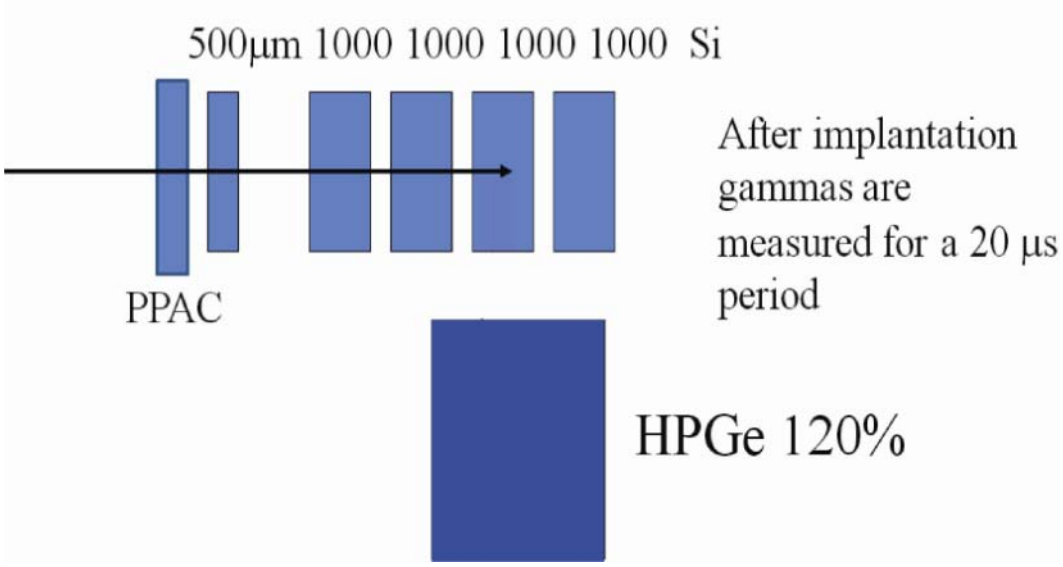

Figure 9: Schematic of the focal plane detector system used for this experiment.

The detection system was designed to characterize fragments by their mass, nuclear charge, atomic charge and momentum. To accomplish this a set of detectors was used at Image 2 (I2) and the focal plane (FP) as shown in Figure 6 and Figure 8. The scintillator at I2 was a plastic (BC-400) rectangular foil with a thickness of 254 micrometers and a width of 300 millimeters. This was used to measure the position of the particle at the dispersive plane allowing partial reconstruction of a fragments flight path. This detector also additionally provided a secondary timing signal to measure the time of flight of the ions in the second half of the separator.

The detector system at the focal place, and shown in Figure 9, consisted of a parallel plate avalanche counter (PPAC), a series of five silicon PIN detectors, a thick plastic scintillator, and a high purity germanium gamma ray detector mounted perpendicular to the Si stack at a distance of 5mm. The PPAC served to record the position of fragments entering the focal plane in order to reconstruct the flight path which is used in particle identification. The first detector in the Si stack was a 500 micron PIN which due to its relative thinness was used to measure the dE/dx of the incident fragments and serve as a start signal for time of flight measurements. The following four PIN detectors were 1000 micron thick and 50mm x 50mm square. These were used to stop the fragments and record the total kinetic energy. After the Si stack was a 10 centimeter plastic scintillator. This was used to catch any light fragments that may have passed through the stack and its signal was used to exclude events from the detection system since total energy had not been collected in the PIN detectors. The Ge detector had a relative efficiency of 120% and was used to measure gamma rays emitted from isomers that were stopped in the Si stack. How the signals from these detectors were used to determine the A, Z, and Q of the fragments will be discussed in the analysis section.

4.Data Analysis

In this chapter we will examine how the signals from the detector system (discussed in the previous section) are transformed into a complete identification of the ions detected in the A1900. First we will examine the physical quantities such as velocity and momentum per charge and which detectors were employed for their determination. Then we will look at how these quantities are converted into a specific mass and inferred A (mass number), Z (atomic number), Q (charge state), E (particle kinetic energy), and P (particle momentum) for each fragment. Finally we shall examine the generation of momentum distributions from these fragments, which are used in the extraction total production cross sections and for comparison to the LISE++ fragmentation-fission model.

4.1 Raw Detector Signals

To make an identification of atomic number, Z, mass number A, charge state Q (fully strip ions have Q=Z), energy, and momentum of the particles, detectors within the A1900 were used to measure positions, times, and energy deposited. For reference, the schematic layout of the A1900 with positions of the detectors is shown in Figures 8 and 9. Labels used in the following discussion are defined in this figure. The data derived from this system were used to

construct the time of flight, kinetic energy, momentum to charge ratio, energy loss in material, and the energies of emitted gamma rays.

4.1.1 Time of Flight (TOF)

The measurement of the time of flight (TOF) of a particle requires a start and stop signal and will have a higher relative precision when it has a longer flight path. In this experiment, the start signal was provided by the PIN detector at the beginning of the focal plane Si stack since each particle was required to reach that point to be measured. It was not possible to use one consistent stop signal throughout the experiment. The initial plan was to use the cyclotron RF sine wave as the stop signal. When the accelerated ions from the cyclotron arrive in a narrow time distribution, this choice provides a signal when the particles began their flight from the target. In practice, during the course of the experiment the cyclotron at times was not well tuned and the reference time relative to the arrival of ions on target varied by up to 6 ns, rendering this method unusable. Hence the RF signal was not always sufficient for the particle identification. In the post-run analysis when the resolution was deemed sufficient to resolve mass numbers it was used and otherwise an alternative method was necessary.

The second method for producing a stop signal used a scintillator placed at the image-2 plane of the A1900. This scintillator consisted of 254 μm BC-400 plastic which emits photons in response to ions passing through it. These photons were then transmitted to either end of the block by direct transmission and internal reflection where they were collected in photomultiplier tubes that produced signals for the stop. The signal rise time is on the order of 1 ns, and hence

the timing resolution of the scintillator was very good, however the flight path from Image2 is only half of that from the target. Also, this scintillator was not used in all settings because it placed material in the beam path and introduced a differential momentum loss for the fragments. Hence not all fragments could be measured at the same time in the focal plane of the A1900. The material at Image2 also caused fragment losses due to changing of charge state in the material. For runs where it was used, a correction to the final yields was applied based on estimates of the charge state fractions from GLOBAL (this correction is described in section 4.4).

The TOF was calibrated by using the position sensitive PPAC detector at Image2 to select fragments that passed through the center of the spectrometer. The centerline data (corresponding to the path of the A1900 central ray) allowed us to know the exact path length of the fragments, which can vary from the nominal value for particles that follow paths different than the central ray by as much as +/- 30mm. The field values measured with NMR probes in the dipoles were used in connection with the known bend radius of the A1900 dipoles of 3.1 meters and a bend angle of 45 degrees to determine the central particle magnetic rigidity (in T-m) and hence the central momentum value (determined from the mass and Q taken from the particle ID). The central path length is known from a laser-based survey of the magnet positions to be 35.64 m.

4.1.2 I2-X and relative momentum

Much of the experiment was conducted using a small momentum slit at Image 1 of 0.1% in momentum per charge. For the other runs with a larger momentum acceptance, the x-position

measurement at the Image-2 was used to determine the fragment momentum. The X-position was measured by using the same scintillator used for the TOF measurements. The scintillator was read out by phototubes on each end and the position was determined by either the difference in time between the two signals or the relative pulse heights of the signals. The position based on these two methods was determined and calibrated as follows.

The time-based measurement involves comparing the time difference between the signals at the two ends of the scintillator. The transmission velocity of light is assumed to be constant throughout the material so a linear calibration can be performed. The data points for this calibration were acquired by comparing the position of particles in a PPAC detector with a known position calibration from previous experiments using the A1900 with the position from the time difference signals from the scintillator. With zero time difference assigned as the center, four points on each side spaced between the center and the edge of the scintillator were used to make the calibration curve. The second calibration method uses the difference in light output at the ends of the scintillator to give the position. Assuming a symmetric distribution of emitted photons and an exponential attenuation of the light intensity as it passes through the material it is possible to relate the difference in energy signals using the equation (1) which is derived from Beer's Law for absorption of light as it passes through a material with constants determined through detector calibration.

$$x = \ln\left(\frac{En}{E_S}\right) * S + O \qquad (1)$$

The calibration for this method is conducted in the same manner as the previous method. The time difference was found to give superior resolution due to the precision of the time signals as opposed to the energy signals. The time method was used for the I2-x position measurement for most of the data with the energy difference method used only in a subset of the data. The energy method was needed early in the experiment due to problems with the recording of the RF-TOF signal that were corrected during the experiment.

With this information, the momentum of any particle could be determined relative to the central momentum by correction for off-center Image-2 (I2) and Focal Plane (FP) x-positions by use of the relationship

$$B\rho_{12} = B\rho_0 * \left(1 + \frac{x_2}{D_1}\right) \quad (2)$$

$$B\rho_{34} = B\rho_0 * \left(1 + \frac{(x_2 * M_{24} + x_4)}{D_2}\right) \quad (3)$$

In this formula M_{24} represents the ion-optical magnification between I2 and FP, while the D represents the momentum dispersion from the target to I2, x_2 is the position at image 2, and x_4 is the position at the focal plane. M_{24}, D_1, and D_2 were all taken from the standard ion optics of the A1900 system with the values of -0.7033, 59.10165 and -41.58004 mm/%

respectively. Equation 2 gives the rigidity for the first half of the A1900 up to Image2 and equation 3 gives the rigidity for segments 3 and 4.

4.1.3 Focal Plane Position (FP-X)

To complete the momentum measurement we used one parallel-plate-avalanche- counter (PPAC) [Swan94] , at the focal plane to record the position x_4 required in eqn (3). The standard A1900 optics was retuned slightly to make an x-focus at the position of this PPAC. In these detectors the central anode has horizontal segmentation on one side and vertical on the other yielding a measurement of x and y.

4.1.4 Energy Loss in Material (dE/dx)

Energy loss in material can be used to identify a particle's nuclear charge using the Bethe-Block formula [Bethe30] plus corrections [Scheid98]. To acquire this data we used the first silicon PIN detector in the stack to collect a signal proportional to the energy deposited in the detector. The signal was calibrated by using a series of ions with known atomic numbers and the known thicknesses of the device in calculations of the energy loss value. The calibration was done by taking the signal channel for several identified ions and comparing it to the predicted energy loss of these ions in silicon using the version of ATIMA contained in LISE++. These channels are then linearly fit to the predicted values giving a channel to energy conversion for

the detector signal. The linear assumption was thought to be valid over the energy range of the ions used in this experiment, as illustrated in Figure 10. The variation in the rated energy loss is approximately 1% for a ^{80}Ga fragment observed in this work.

The quality of the Z-identification we obtained in the experiment is illustrated in Figure 11. The Z values can easily be resolved even in the raw dE-TOF for both timing methods. Due to the high resolution, the atomic number was typically used as one axis of the particle identification plots as will be shown later.

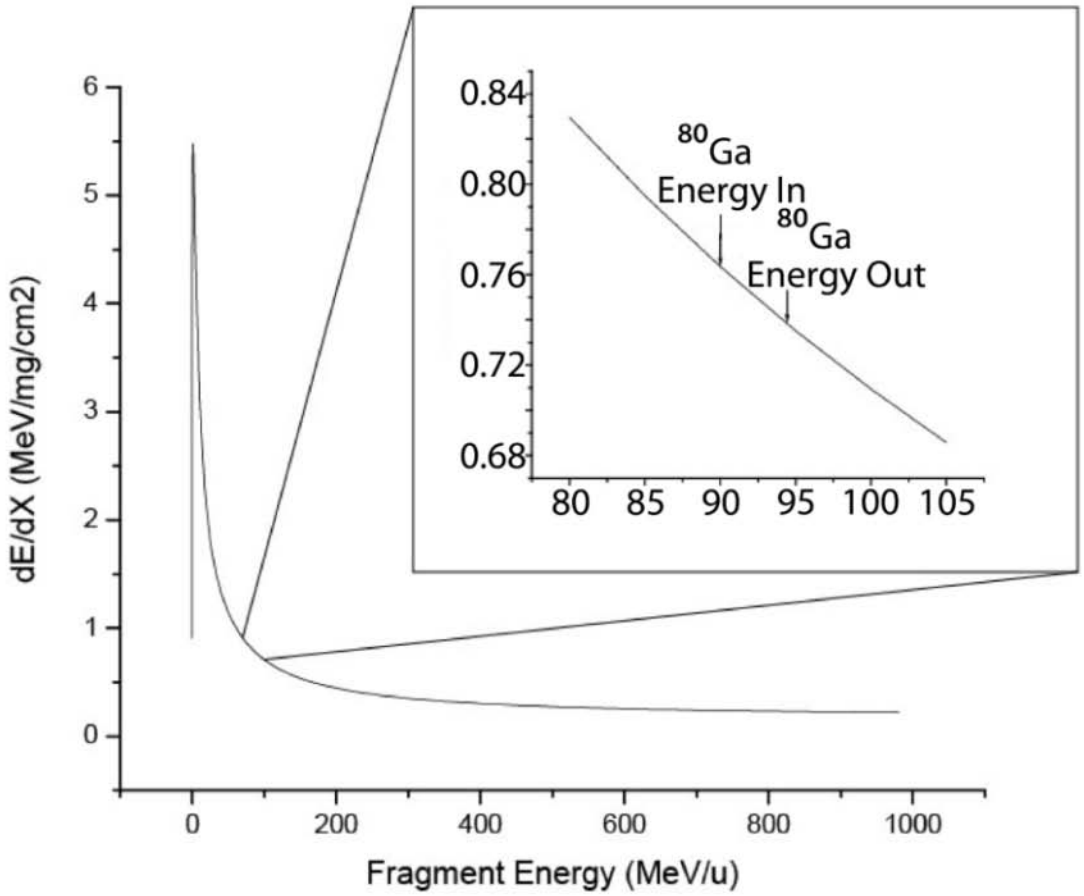

Figure 10: Calculated energy loss of ^{80}Ga in a BC-400 scintillator predicted by the code ATIMA [Lin96]. The inset shows an expanded region illustrating the relatively linear slope of the dE/dx curve in the region of the particles passage.

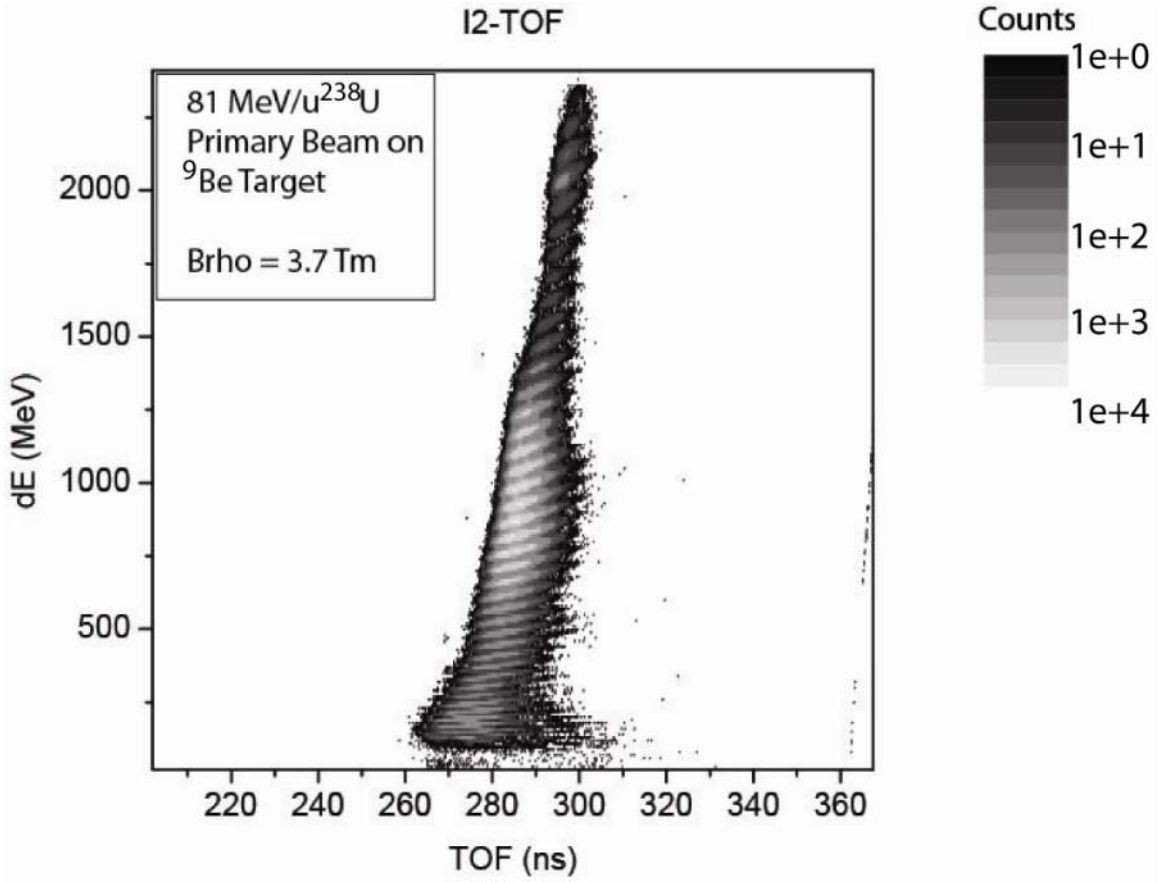

Figure 11: Distribution of energy loss, dE, versus time of flight, TOF, raw data signals using the RF timing stop signal (top) and Image-2 scintillator timing stop signal (bottom) for same data set. Notably the RF signal produces a double image of the data because every other stop pulse was removed by a down scaler. The figures show that the Z resolution using the first PIN detector is excellent and atomic numbers from 20 to 60 can easily be resolved.

Figure 11 (Cont'd)

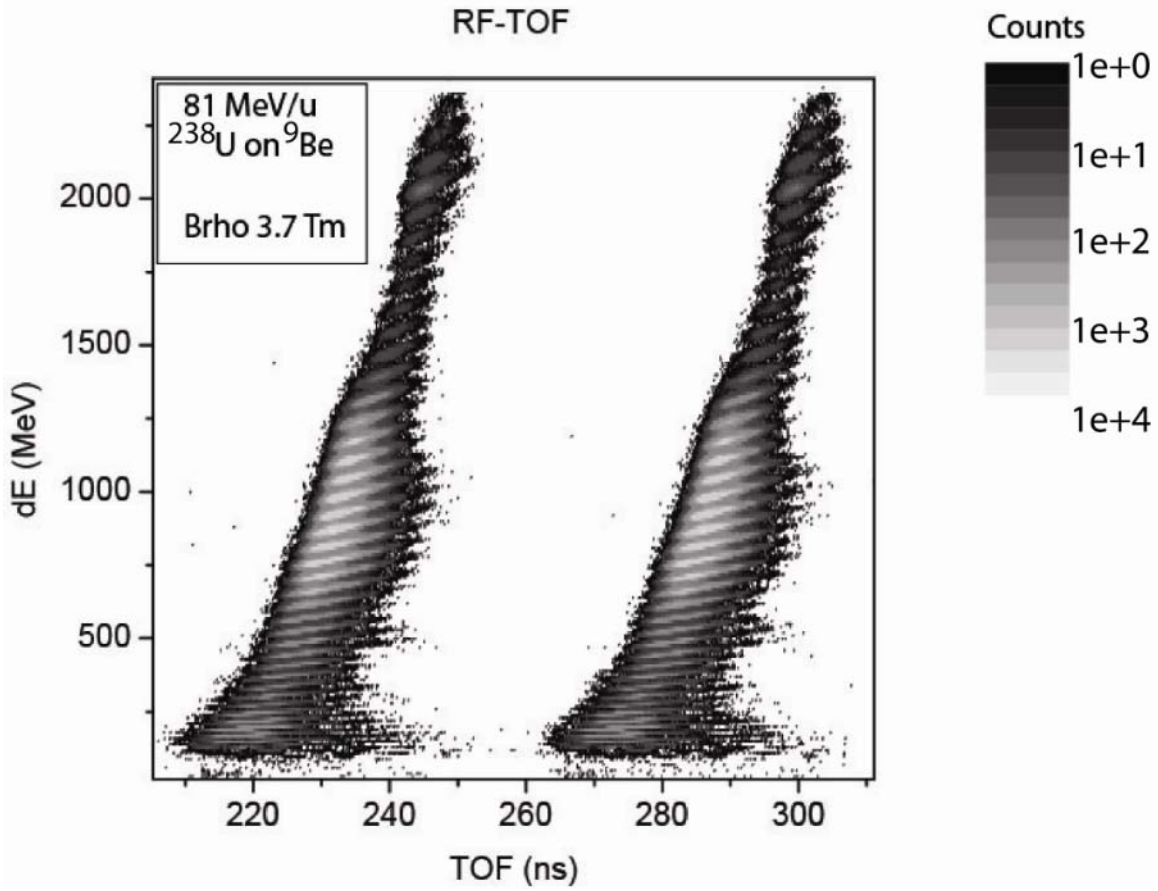

4.1.5 Gamma Ray Spectra

A small fraction of the reaction products were found to be created in isomeric states. Isomeric states are long lived excited nuclear states which decay by photon emission and photon energies are generally unique. The detection of these photons allowed unambiguous identification of an isomeric particle. To take advantage of this identification technique (called isomer tagging in the literature [Grz95]) we installed a 120% efficiency Germanium detector perpendicular to the Si stack. When the fragments stop in the stack any isomeric states would start to decay with their characteristic half-life. In this experiment, a time window of 10

microseconds was opened following a signal from the Si stack. Gamma ray signals obtained within this window were recorded. With a 10 microsecond window we have a 0.005% chance of a second event coming in before the gamma can be recorded, and any shorter lifetime isomers would usually decay before they are actually stopped in the stack. Since this detector was installed for particle identification purposes rather than a detailed isomer study we made no effort to have a high detection efficiency. In our case the absolute efficiency for detection of a 1.4 MeV gamma ray was around 1% and was determined by placing a source in a mockup of the silicon stack and comparing the observed gamma spectra to the spectra predicted to be emitted from the previously characterized source. The energy calibration for this detector was done using a ^{152}Eu source shown in Figure 12.

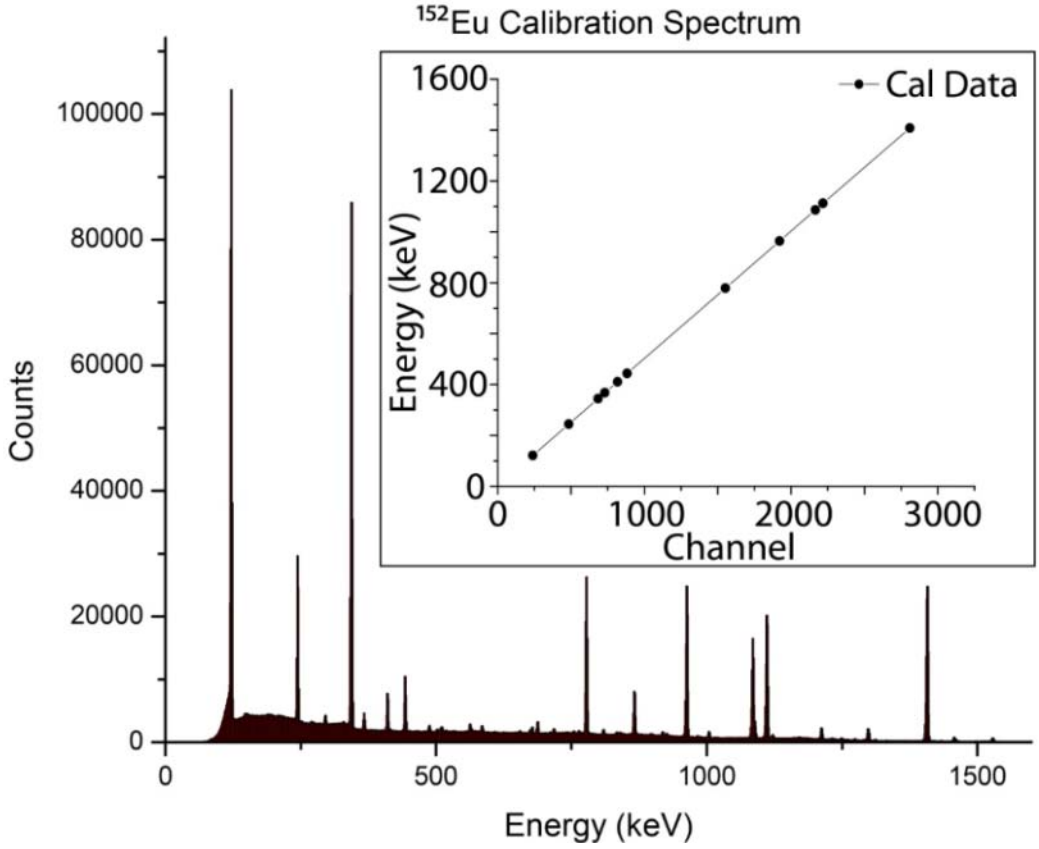

Figure 12: Germanium detector energy calibration spectrum taken using a ^{152}Eu source with known gamma-ray energies. Inset: Calibration curve relating detector channel number with known gamma energies.

4.2 Particle Identification (PID)

Here we present the data analysis scheme that was used to process the signals described above and translate them into the final cross sections for individual products along with their momentum distributions. We have not yet described the calibrations of the silicon telescope, because in our method this calibration requires a rudimentary particle identification (PID). The initial portion of the analysis dealt with the particle identification which allowed the calibration

of the detector signals. After this we will examine how the data signals were translated into physical quantities and then show how those quantities were translated into the final outcome of momentum distributions and production cross sections.

4.2.1 dE-TOF Pattern

Identifying individual heavy ions without an absolute calibration of a detector setup requires examining the raw data for signatures unique to particular isotopes. The most basic means to examine raw data for patterns is to look at a two dimensional energy loss in matter versus time of flight plot. This plot is roughly analogous to a nuclear charge versus mass to charge ratio plot since the Z term is dominated by the dE/dx while the A/Q is primarily determined by TOF as will be discussed later. For cases in which the fragments have a very narrow momentum width, the times of flight are resolved enough to generate a pattern where each intense region is produced by one isotope. The isotopes vary within the pattern as shown in Figure 13. This plot can be used with uncalibrated detectors since it relies on relative positioning rather than a fixed value for identification. While the pattern itself is straightforward it remained a challenge to fix a reference point on which to base the identification. In cases where low mass isotopes are generated it is possible to observe a gap in the pattern where an unbound isotope such as ^{8}Be or ^{10}Li would be and use the hole created by the absence of that isotope as a starting point. In our case however, the lighter isotopes were not populated and such reference points were not available.

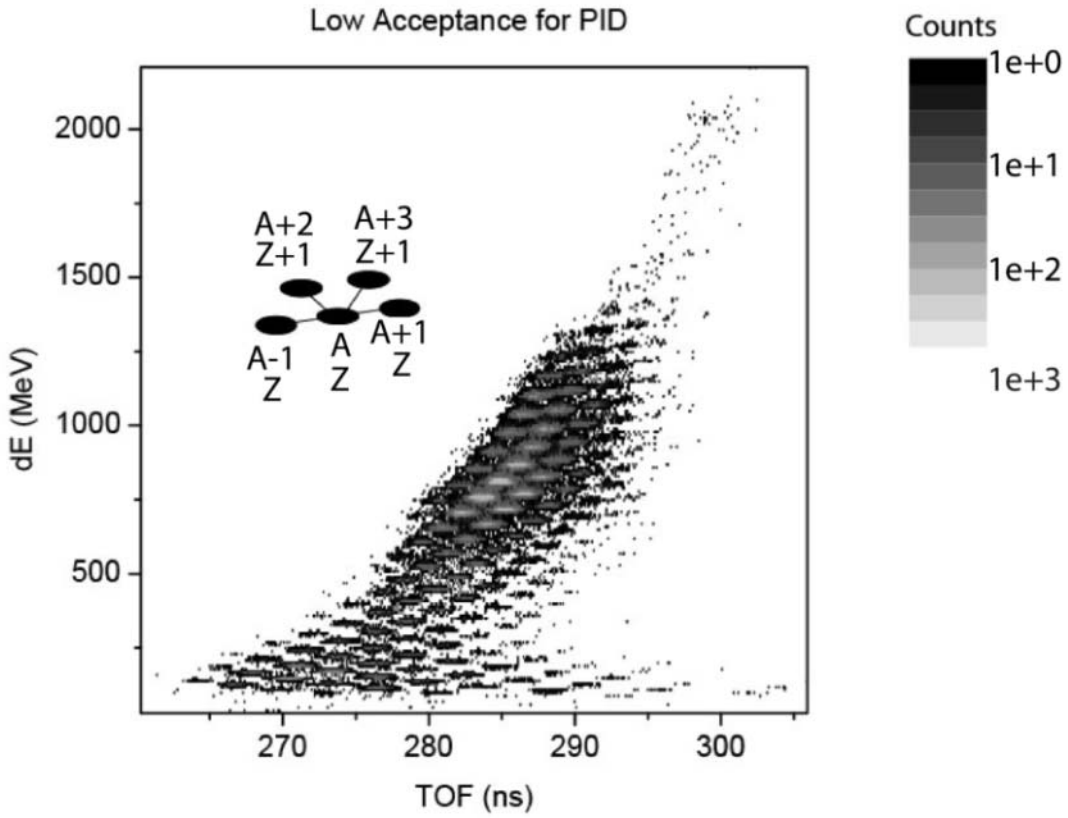

Figure 13: Energy Loss vs. Time of Flight for one setting of the A1900 used for initial particle identification. Once a reference point is found in this plot, the region of the pattern containing the mid mass isotopes of interest to this work can be identified using the pattern indicated.

4.2.2 Isomer Identification

To determine our reference isotope in the PID map we had to rely on isomer signatures that were collected in the Ge detector adjacent to the Si stack. Our search for isomers was guided by locating regions in the dE/TOF plot that had an unusually large number of gamma rays coincident with a given spot. An example of using a gamma to total counts ratio in an A vs. Z plot generated from the data set is given by Figure 14. Locating isomers to use for identification however turned out to be non-trivial, not because we could not identify isomers, but because so

many nuclei were detected in isomeric states. Many of the observed lines were unknown. The primary complication to this process was the limited number of known isomers in the region of isotopes produced by the fragmentation-fission process. Identification was hindered by the small number of the observed isomers that had been recorded in available databases. Only a small portion of the total number of fragments generated during the fission reaction could be transmitted to the end of the separator for a given setting, so that for each setting we had to ensure that there was a microsecond lifetime isomer in one of the more intensely produced and transmitted isotopes so that identification could be carried out in a limited time. This problem was compounded by the unknown fraction of these isotopes that would populate an isomeric state after the reaction as well as the losses of emitted isomer gamma rays due to the limited acceptance of the germanium detector. For this analysis we used ^{96}Rb, ^{99}Mo, ^{98}Y, ^{66}Cu, and ^{118}Sn for identification purposes depending on which isomer was transmitted efficiently in a particular experimental configuration.

These isomers could then be analyzed by applying a gate to the data set so only fragments with a coincident gamma signal in the Ge detector would be plotted. It then became possible to observe the gamma spectrum generated from one particular isotope using a second gate on the energy loss versus time of flight plot. With several candidate isomers identified their gamma spectra were compared to those of known isomers. After having confirmed the identity of one fragment in a setting by means of the isomer we were then able to identify all fragments in a given setting which allowed us to identify several of the new isomers as will be shown in the results section.

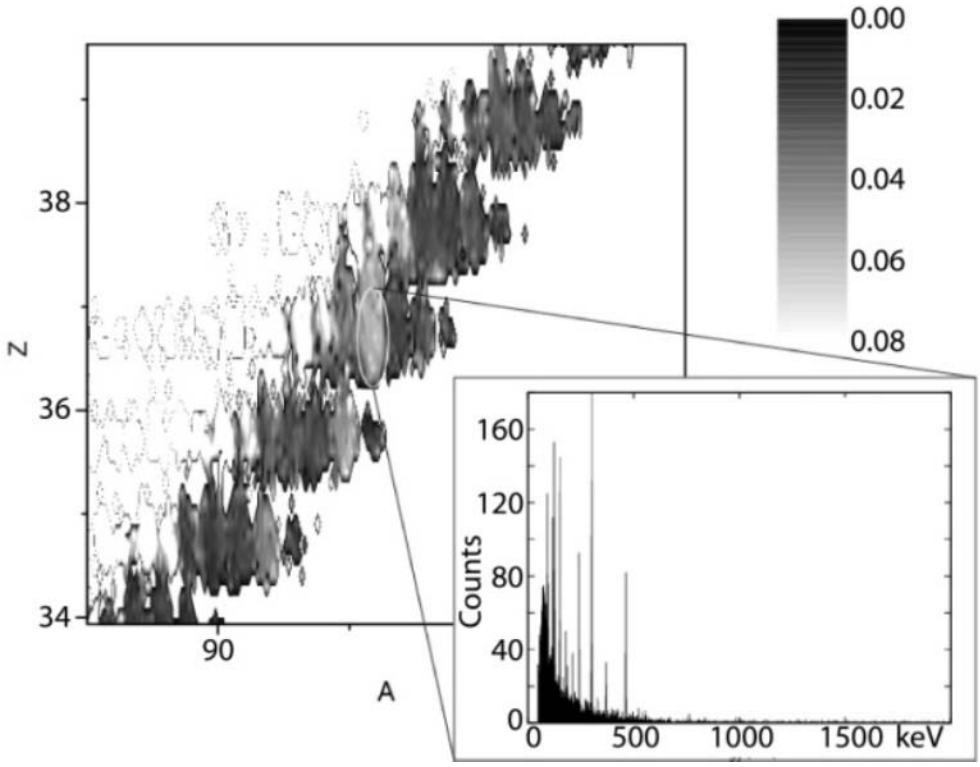

Figure 14: Data plot showing the ratio of data points with a corresponding gamma ray to the total number of counts in the bin. Inset is the gamma spectrum of the highlighted isotope: ^{96}Rb.

4.3 Derived Particle Identification Quantities

Relying on known physical relationships between the measured quantities it is possible to determine the detected fragment's mass, nuclear charge and parallel linear momentum, all of which are necessary for successful calculation of the momentum distributions and production cross sections. In this section we will discuss the method to determine these values. After a discussion of individual measurable quantities we will then move on to describe the method of combining these quantities to get the necessary results and the physics and assumptions behind the calculations.

The general scheme of how the measured information is converted into the parameters mass (and hence A), Z, Q, p and E is illustrated in Figures 15 and 16. The details are given in the following sections with the formulas use for the determinations, and how the experimental data was calibrated.

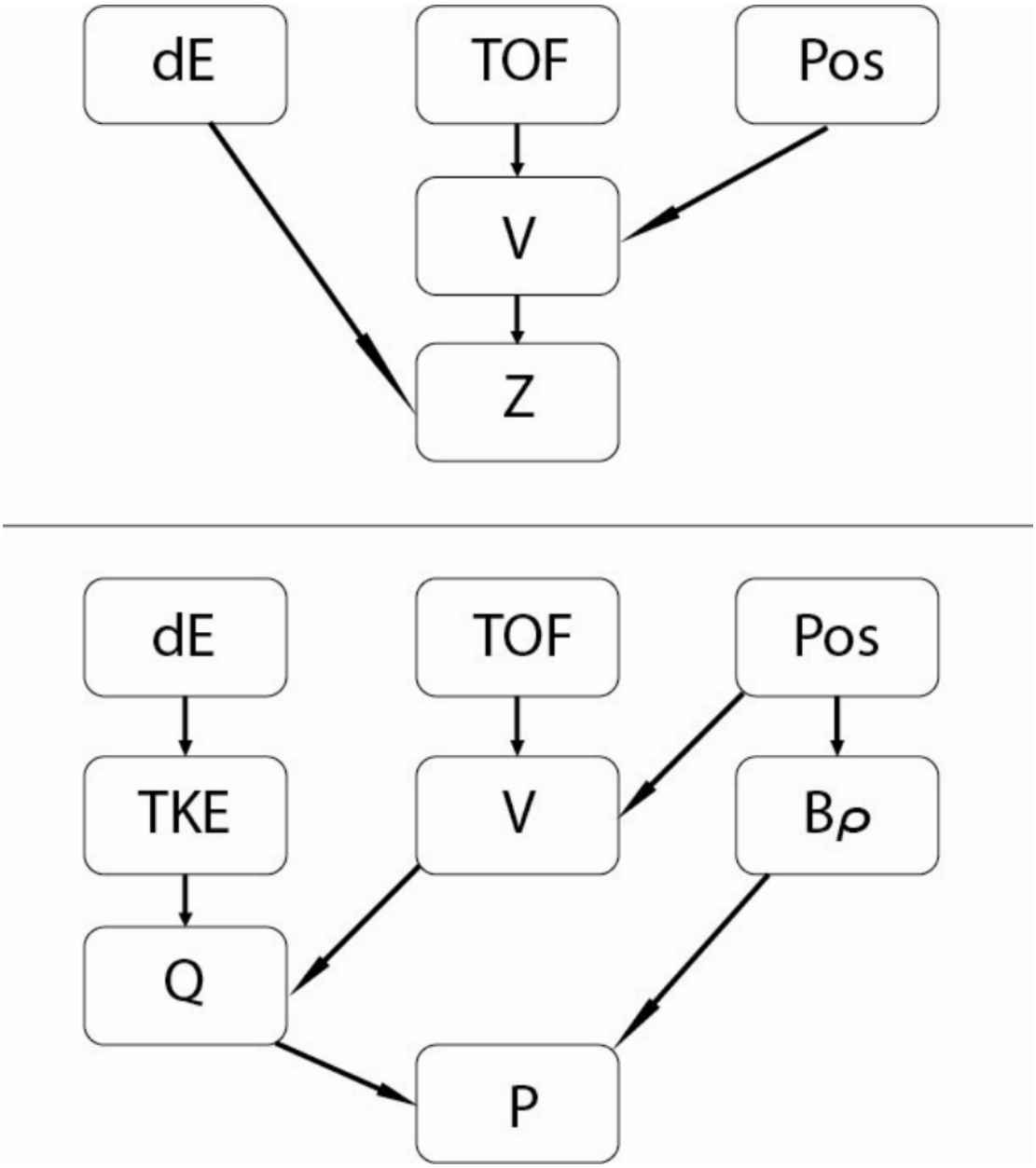

Figure 15: (Top) Flow chart for the calculation scheme for the nuclear charge (Z) using raw detector data; energy loss (dE), time of flight (TOF) and position in the beamline (Pos). (Bottom) Similar chart for the calculation of the fragment momentum (P).

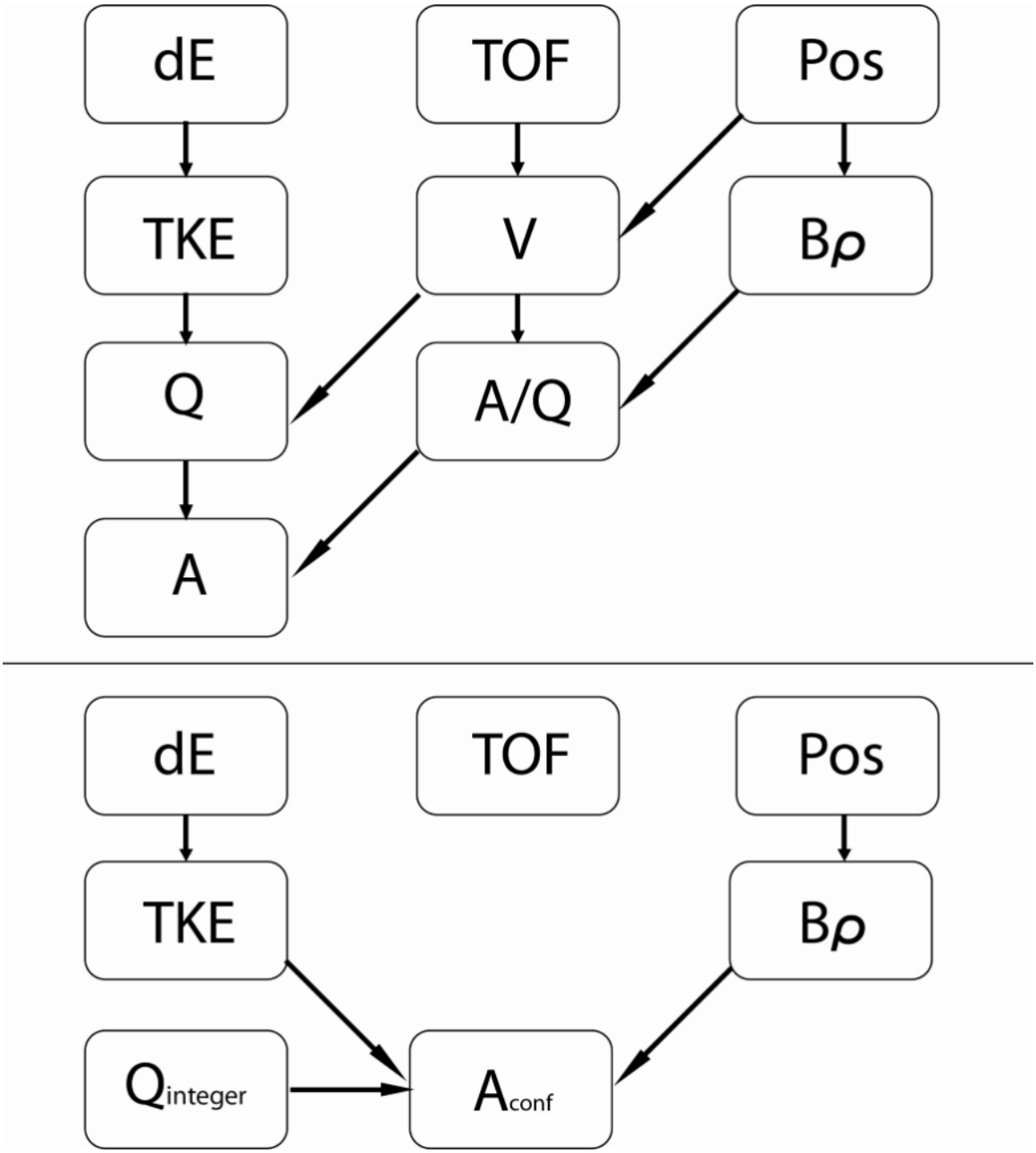

Figure 16: (Top) Flow chart for the calculation scheme for the nuclear mass number (A) using raw detector data; energy loss (dE), time of flight (TOF) and position in the beamline (Pos). (Bottom) Similar chart for the calculation of the mass number confirmation. Note that in this case TOF is not used, so the A determined in this way provides an independent confirmation.

4.3.1 Velocity (V)

We begin with the determination of a fragment's velocity. Velocity requires knowledge of the fragment's time of flight, TOF, as well as precise knowledge of the flight path as shown in

$$\beta = \frac{L}{TOF * c} \tag{4}$$

Where L represents the flight path length and TOF is the fragment time of flight. For cases where the flight path is confined by the momentum slits along the central axis of the beam pipes L = 35.64 m. However, in the cases where the beam is allowed to occupy the entire acceptance of the A1900 this becomes significantly more complicated. For computational simplicity the correction in path length for particles not at the central momentum was folded into the time of flight by using the calculated variation in path length with momentum deviation and the position at Image2. We were able to take advantage of the approximately linear relationship between position at the dispersive plane and the path length difference from the central ray in order to calculate the fragment velocity as described above. The linear relationship between velocity and dispersive plane position is shown in Figure 17. This corrected time of flight was then used in eqn (4) to give the fragment velocity. The correction is equivalent to using the correct momentum-dependent path length in the calculations due to the subsequent calculations only using velocity, not time of flight or path length..

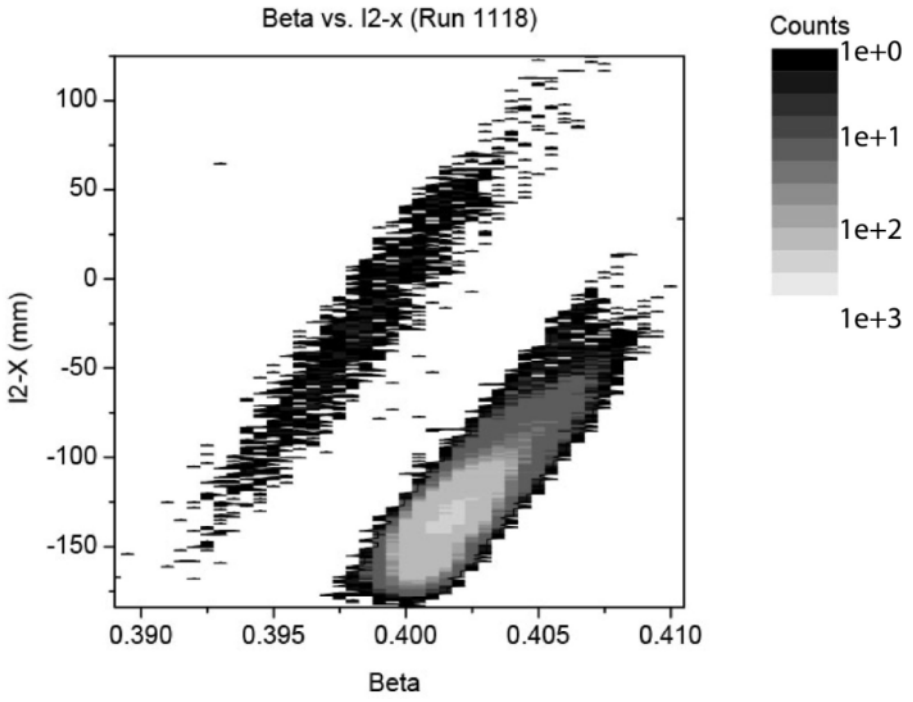

Figure 17: Plot of ^{80}Ga velocity vs. position at the I2 scintillator. The relationship between velocity and position appears linear as expected due to the variation in particle momentum as a linear function of image2 (I2-x) position in the ion optical calculations. Also shown in the figure is the presence of two charge states in the data. The lower group corresponds to fully stripped ions and the upper to electron ions.

4.3.2 Mass to Charge Ratio (A/Q)

With the calculation of the fragment velocity it was possible to calculate the mass to charge ratio of the fragment. Using the following relation (5)

$$B\rho = \frac{p}{Q} \tag{5}$$

Where p is the fragment momentum, Q is the atomic charge and $B\rho$ is the fragment's magnetic rigidity (determined from the measured central magnetic field measured by an NMR system and the known central bend radius of the A1900 dipoles). This is derived from the Lorentz force on charged particle in a uniform magnetic field. It can be shown that

$$\frac{m}{Q} = \frac{B\rho}{k\beta\gamma} \tag{6}$$

Where m/Q is the mass to charge ratio and $k\beta\gamma$ is a function of the fragment velocity with k as a unit conversion term.

For cases with a small acceptance this again is trivial since the velocity has already been determined and the magnetic rigidity can be taken directly from the magnet settings since the fragments are along the central axis. The complications arise when the acceptance is wide. In the wide acceptance case the fragments are no longer confined to the central axis and the flight radius though the dipole magnets can vary significantly, allowing a much wider range of magnetic rigidities. To compensate for this it is necessary to calculate the correction to the magnetic rigidity from the off axis travel. This can be done using the relations 2 and 3 described earlier. Equation 2 is the correction in magnetic rigidity in the first half of the spectrometer based upon the dispersive plane position and the dispersion of the system between the target and dispersive plane (D_1). Equation 3 describes the correction for the second half of the spectrometer where the M_{24} term represents the magnification between the dispersive plane and focal plane.

Using the positions signals from the Image-2 and Focal Plane detectors along with the known optical terms from the A1900, corrected magnetic rigidities were generated. These values were then used, along with the velocity, to calculate the mass to charge ratio for each fragment. In previous experiments at GSI and RIKEN (results shown in the next section) the A/Q ratio plotted versus Z was sufficient for particle identification, but in cases with low beam energy, many charge states are present ruining the A/Q particle identification due to overlap between fragments with similar A/Q ratios within an element as seen in Figure 18. For this reason we are forced to calculate the fragment mass and charge separately to identify our particles.

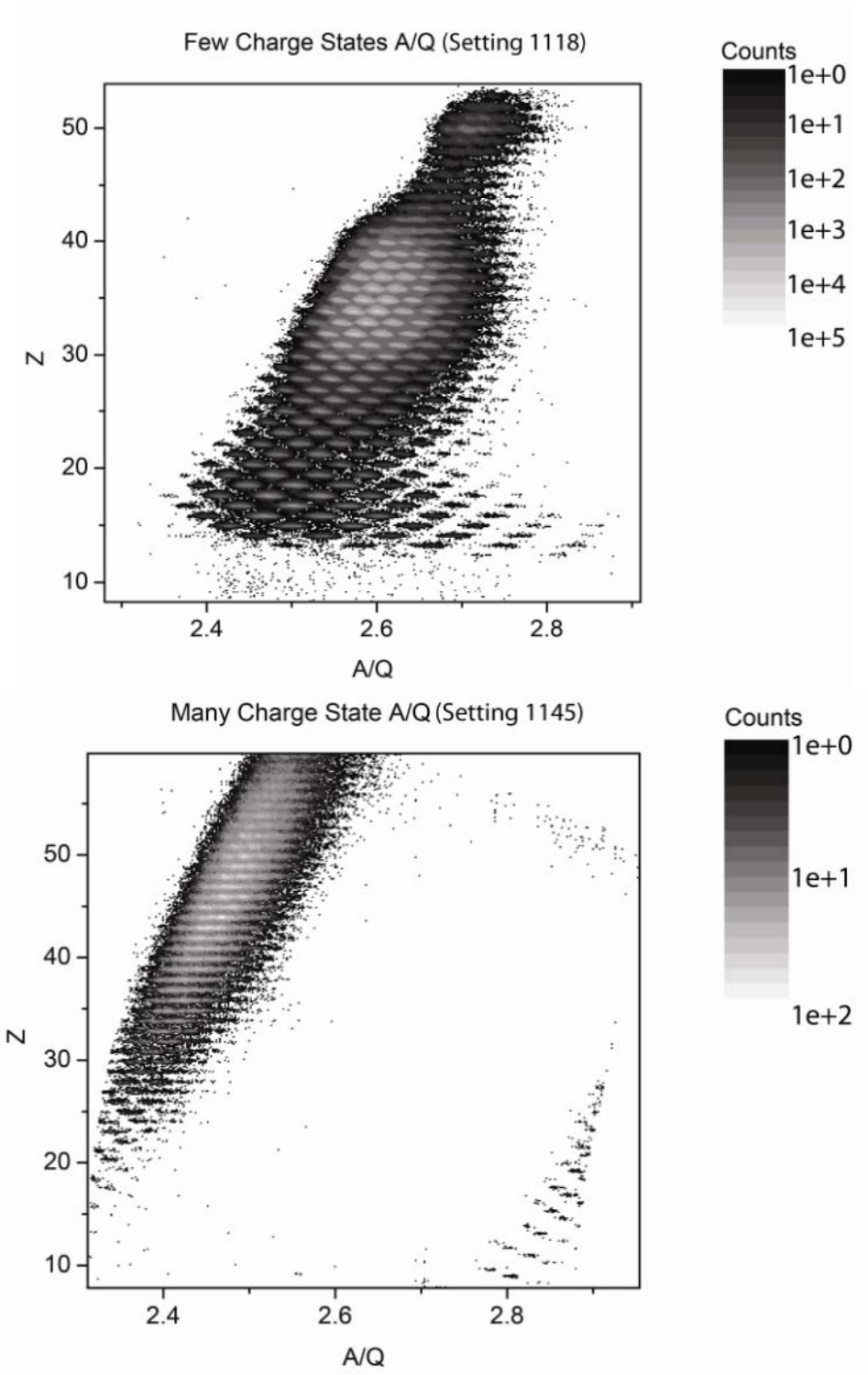

Figure 18. (Top) Z versus A/Q particle ID plot for a case with one dominant charge state. In this case PID can be easily done using an A/Q measurement. (Bottom) With many overlapping charge states it is impossible to identify the particles with a simple A/Q measurement.

4.3.3 Total Kinetic Energy (TKE)

The total kinetic energies (TKE) of the fragments were determined by stopping them in the stack of Si detectors at the A1900 focal plane (as illustrated in Figures 8 and 9) and combining the signals of the individual detectors. With the experimental setup used there were two methods available to calculate the fragment TKE's, either by calibrating each individual detector and summing the energy signals, or by calibrating the entire stack of detectors as one detector and getting the energy value directly from the combined detector system. Both methods assume a linear relationship between the detector signal and the energy deposited in the detector. During the analysis we tried both methods and found the combined system calibration to be superior [Tar07]. This method eliminates any uncertainty caused by unknown detector thicknesses and errors in the energy loss model since the energy of the particle is known exactly from the magnetic rigidity and one knows the sum of the detector energies must add up to this value.

$$(7) \quad TKE = KE_1 * S_1 + KE_2 * S_2 + KE_3 * S_3 + KE_4 * S_4 + KE_5 * S_5 + Offset$$

The TKE calculation above uses the individual energy signals (KE) from each detector and then multiplies them by their individual calibration term (S) with dimensions of energy/channel with a global offset added to reach the correct energy.

The combined detector calibration works by simultaneously fitting the channel to energy conversions for each of the detectors with the total predicted TKE for an identified isotope. These fits were done with (n+1) free parameters where n is the number of signal generating detectors in the stack and the additional parameter is the calibration offset. The fit that, as a total group, gives the best agreement to the predicted energies is taken to be the calibration. Even though the channel to energy conversion for the individual detectors is often not close to what is predicted by energy loss models, the entire system matches quite well for all isotopes that stop in the same system of detectors. The downside to using this method is that the calibration needs to be redone for different stopping detectors. This is due to the calibration being done as a set of detector signals rather than a series of individuals, and the addition or removal of a signal from the system (by stopping in a different detector) invalidates the calibration.

4.3.4 Nuclear Charge (Z)

A fragment's nuclear charge can be obtained from a single thin Si detector that the fragment passes through. For our work we have modeled the amount of energy lost in a thin layer of material by using a variant of the Bethe-Block equation. Since we are assuming a layer that is a small fraction of the fragment range, the energy loss per unit thickness of the detector can be taken to be constant with a dependence upon the square of the ratio of the nuclear charge to fragment velocity. Given an energy loss from the thin Si detector and the velocity from the time of flight measurement the nuclear charge for a given fragment can be inferred. This was calibrated by comparing the energy loss predictions for a number of fragments to the channel numbers from the detector and getting a linear relationship.

$$Z = \sqrt{\frac{dE}{V_{Term}}} * S + O \tag{8}$$

$$V_{Term} = \left(-1 + \frac{ln\left(\frac{k}{\frac{1}{(\beta^2 - 1)}}\right)}{\beta^2} \right)$$

Calculation of Z where dE represents the energy loss in the first Si detector, S is the calibration slope, β is the velocity of the fragment in terms of the speed of light and k is the unit conversion constant. The quality of the Z identification can be seen in Figure 19.

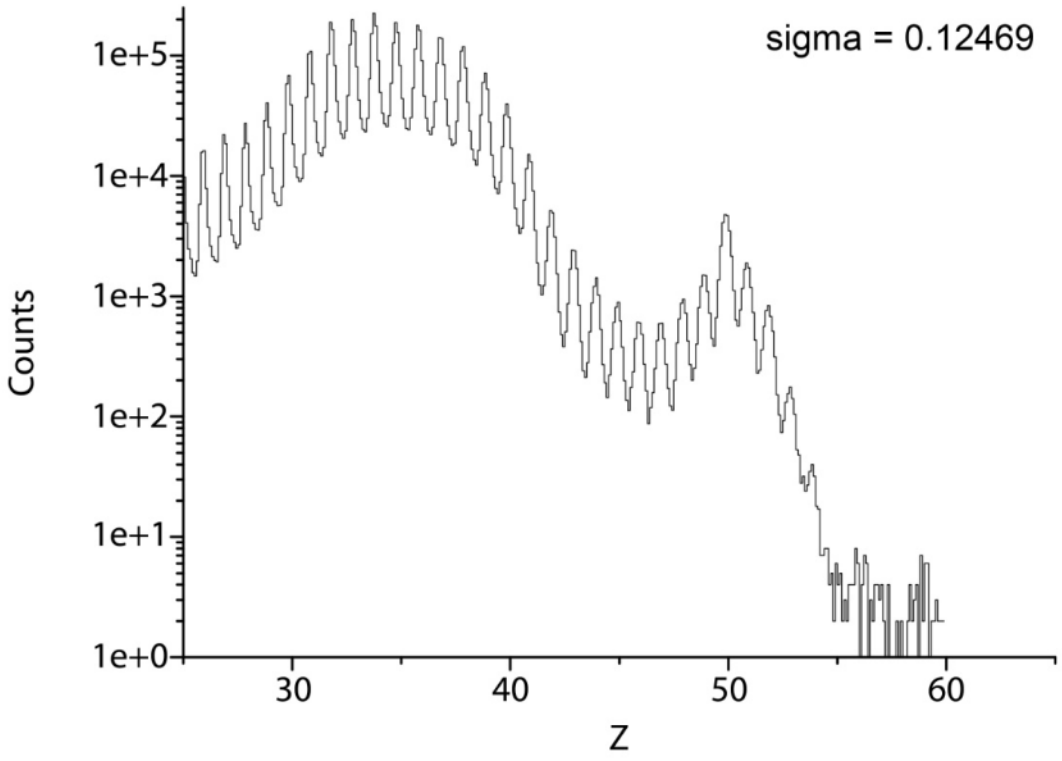

Figure 19: Typical Z resolution using this calculation method. The high quality of the Z identification allowed it to be used as a basis for the automated data counting system described later in this chapter.

4.3.5 Atomic Charge (Q)

Having determined a fragment's TKE, mass to charge ratio, and nuclear charge it becomes possible to calculate the ionic charge. The primary method of charge state calculation that we used relies on equation (9). This equation was derived from relativistic energy conservation principles by removing the TKE from the total energy allowing the extraction of the charge state as a function of the mass to charge ratio. Due to the number of calibrated

measurements used to derive this value it is particularly sensitive to errors in any of the measurements or calibrations. A second method to confirm the Q will be discussed in a following section.

$$(9) \qquad Q = \frac{TKE}{(\gamma - 1) * \frac{m}{Q}}$$

$$\gamma = \left(\frac{1}{1 - \beta^2}\right)^{\frac{1}{2}}$$

In this formula A/Q represents the expression in equation (6). The Q distribution measured in this way is shown in Figure 20.

We found that the Q values obtained using this technique sometime lead to errors in mass identification. To reduce the number of fragments with bad charge state values a second method was used to confirm the results of equation (9). The method and equations are given in section 4.3.7 below. This method was derived independently of the first using a combination of total kinetic energy similar to the first method and the Lorentz force equation to get a relationship between the charge state, mass, and total kinetic energy. Unfortunately this method has two remaining free variables, the mass and charge state, meaning that it cannot independently determine the charge. The main advantage if this method is that it can safely assume an integer charge state since that physical quantity is an integer. For a given charge state the formula gives a specific mass and hence approximate mass number, A, for the fragment. The mass number determined in this way can be compared to the mass number calculated from equation (10) discussed in the next section. As will be seen shortly, if the calculation for the charge state in the first method is correct, then the mass calculated must agree with the mass calculated using the

same charge state in the second method. If not the charge state can be iterated until both methods give the same atomic mass, A. Because a 1% variation in Q leads to a 2% variation in total energy, this technique can provide a unique determination of Q. That is, only one Q can give a consistent A for both methods. The resolution of A/Q for a single particle using this method can be seen in Figure 20. The distribution of the cross section in the two charge states matches well that expected from GLOBAL at this magnetic rigidity setting.

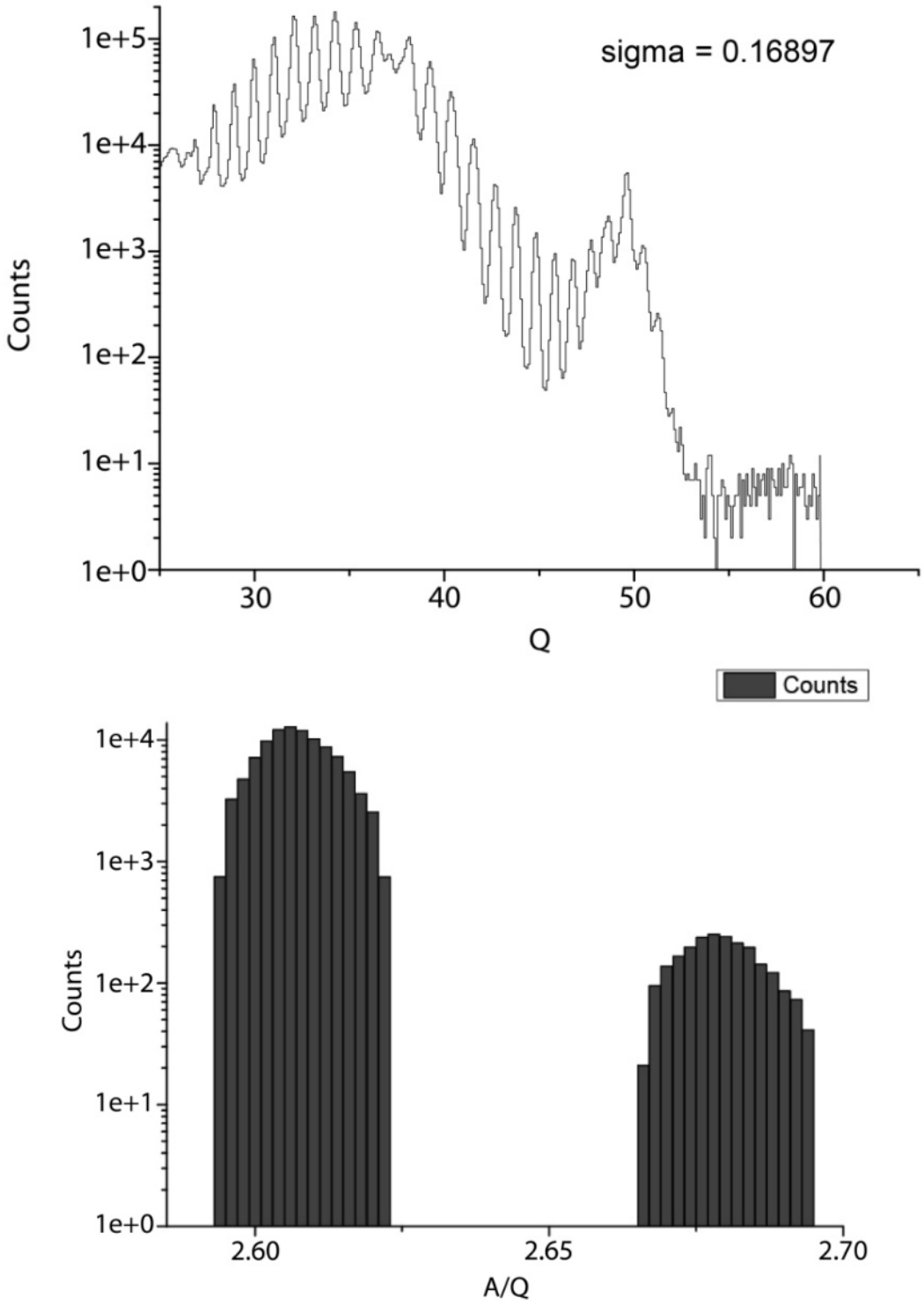

Figure 20: (Top) Typical Q distribution for the data set. The peak split near Q = 38 is an artifact created during total kinetic energy calibration and is accounted for in the final particle identification. (Bottom) A/Q resolution for ^{96}Rb after confirmation method. The A/Q spectrum has no contribution from the Q calculation in its derivation indicating that the separation is not an artifact.

4.3.6 Mass Number (A)

With the above terms fixed it is now possible to determine the nuclear mass of the fragments. The primary method of calculating the mass consists of simply multiplying the mass to charge ratio with the nuclear charge determined in eqn. (9). This method gives a mass value that works well in cases where the constituent components only have a small error spread. When the errors increase the spread in mass number becomes greater than one mass unit, destroying the resolution.

$$m = \frac{m}{Q} * Q \qquad (10)$$

In this formula m/Q is the term taken from Equation (6) and Q is taken from Equation (9).

4.3.7 Mass and Charge Confirmation

To compensate for uncertainty in mass and charge calculations we can take advantage of the fact that the ionic charge must physically be an integer. However, we cannot assume that the correct value of ionic charge is just the nearest integer value to that calculated in eqn (9). Instead we can look at the mass number calculated by a second method, eqn(11).

$$A_{conf} = \left(\frac{TKE}{\left(\frac{V_t + 1}{V_t - 1}\right)} - 1 \right) \tag{11}$$

$$V_t = \frac{(B\rho)^2 Q^2}{TKE^2}$$

Due to the different methods of calculation the two mass formulas will only agree in the case where the correct integer value of nuclear charge is used. This happens because the mass value in the first method shifts by the mass to charge ratio with each integer jump of the nuclear charge, while in the region of isotopes relevant to this work the mass number shifts by nearly twice as much using the second method. Because the mass value is determined without the use of the time of flight measurement it is independent of the mass calculated using equation (10) it can be used to confirm the mass calculation. By using this comparison we can then assign an integer value of charge for the first mass method to get much better resolution by eliminating the spread in calculated charge, as shown in Figure 21. This method of identification by mass number overcomes the resolution problems with the A/Q method when many charge states are present. Figure 22 compares the many charge state A/Q plot from Figure 18 to the mass number plot for the same data set.

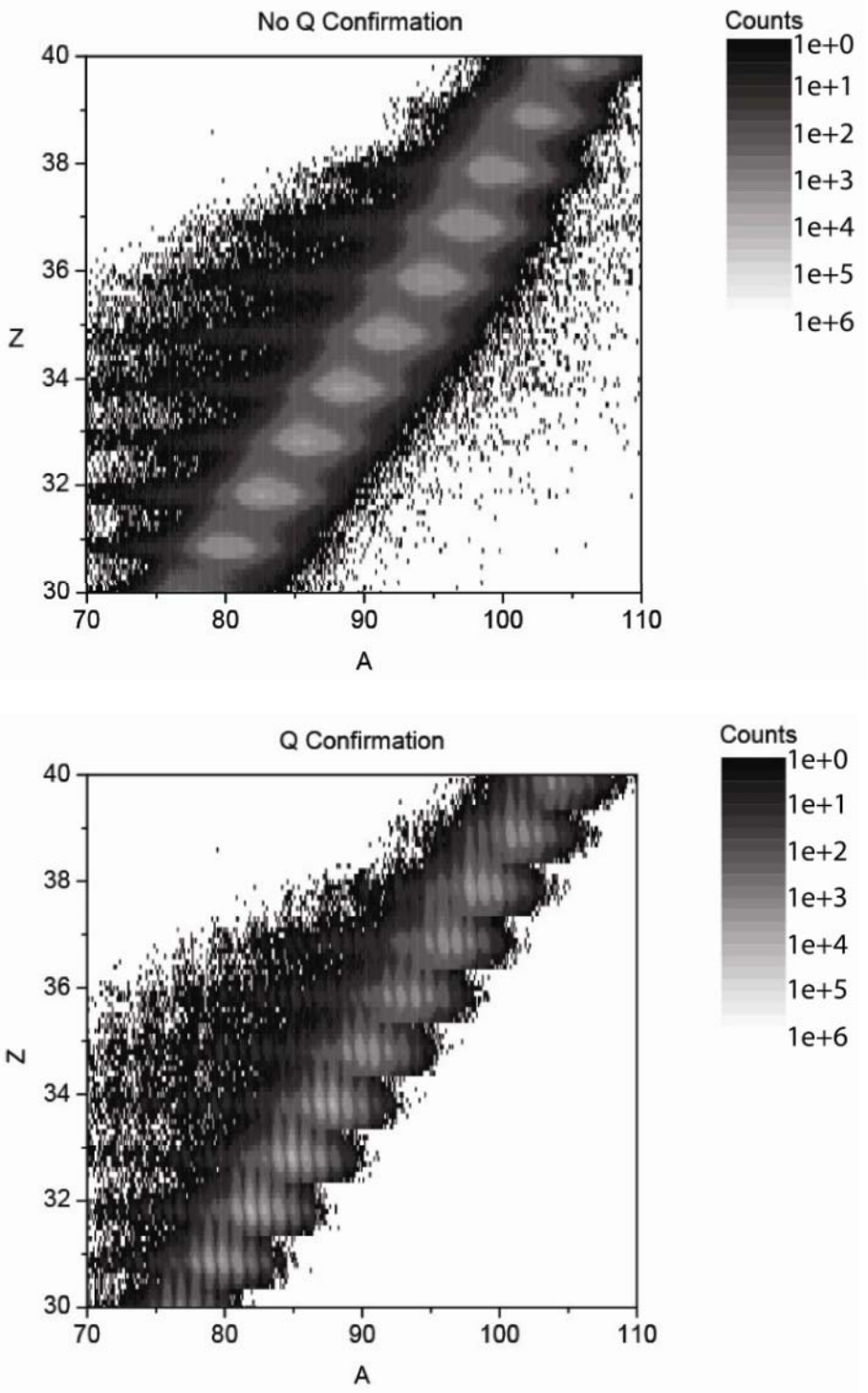

Figure 21: (Top) A typical data set using the charge state calculation based upon the TKE and A/Q. (Bottom) The same data set using an integer value of Q determined with the confirmation method. In this case a number of invalid data points were discarded, cleaning the distribution.

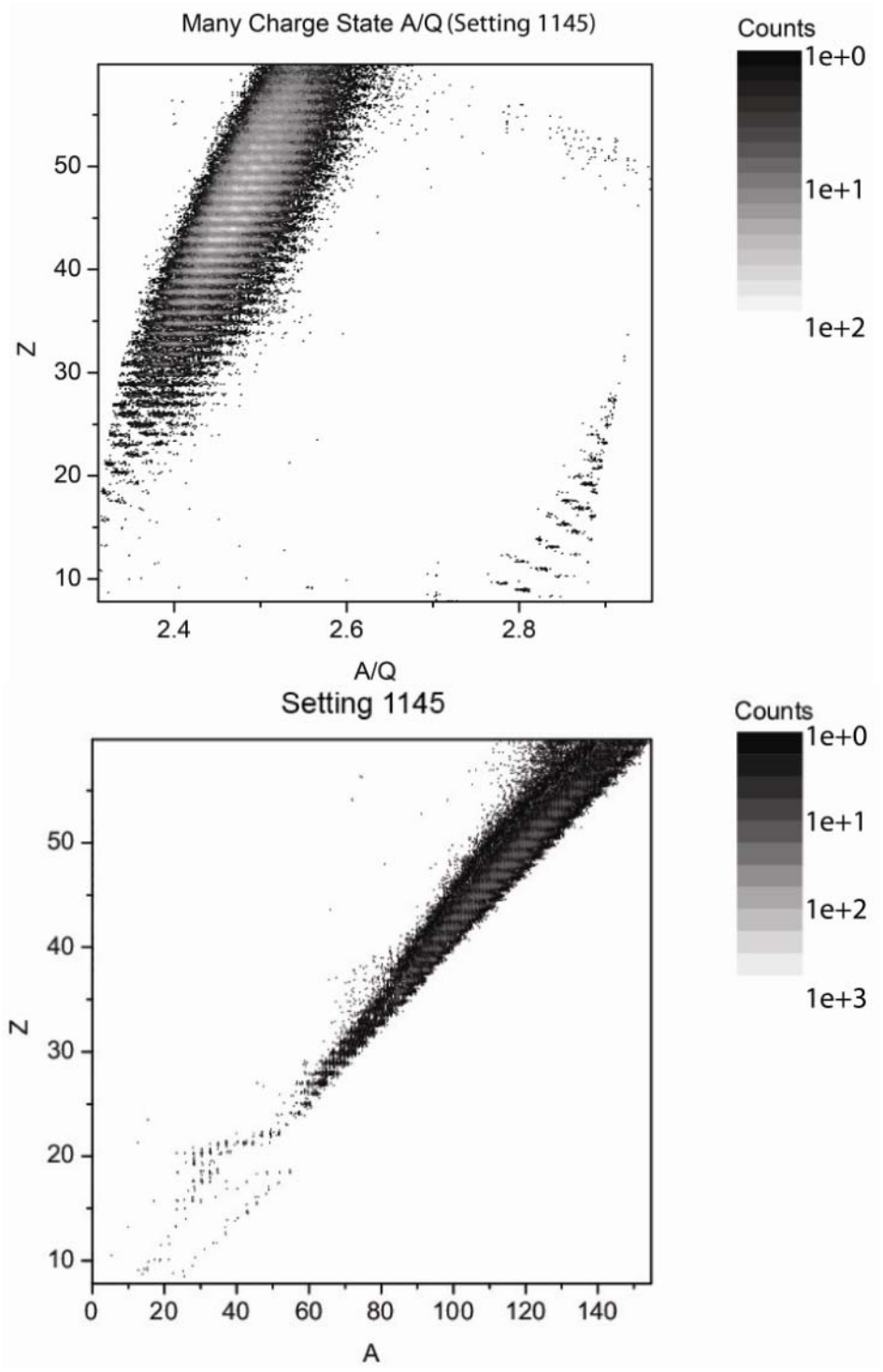

Figure 22: (Top) A multiple charge state particle identification plot based upon A/Q measurements. (Bottom) A particle identification plot for the same data set using the A with Q confirmation method, demonstrating that this method allows identification of fragments with a large number of charge states present.

4.4 Data Counting and Fitting

After the calculation of the physical parameters for each data point we are able to count the number of each detected fragment type as a function of rigidity and integrating them into final distributions for comparison with theory. Because of the large volume of data generated during the course of this experiment it was necessary to develop techniques and software to rapidly count the data and combine them into data sets using common mass, ionic and nuclear charge, and momentum.

The first step in this process was to take the total data set and divide it into smaller portions based upon the nuclear charge, ionic charge, spectrometer setting, and magnetic rigidity through the second portion of the separator. Dividing the data set in this manner reduced the total data set to a series of one-dimensional plots of nuclear mass, each containing several peaks. While somewhat counterintuitive, reducing the total set into a large number of one dimensional spectra rather than keeping it as a few two dimensional spectra reduced the computing requirements to count the data allowing for much faster processing of the entire data set. The choice of gating parameters was motivated by choosing the ones with the best resolution, with the nuclear charge having the best resolution and the ionic charge being assigned to an integer value as described in the previous section. To ensure consistency with between wide and narrow momentum acceptance settings we selected a magnetic rigidity gate of momentum width +/- 0.2% to be consistent with the spread of momentum allowed in most low acceptance settings. Because of its relatively poor resolution compared to other terms the nuclear mass was selected as the free term to be included in the one dimensional spectra.

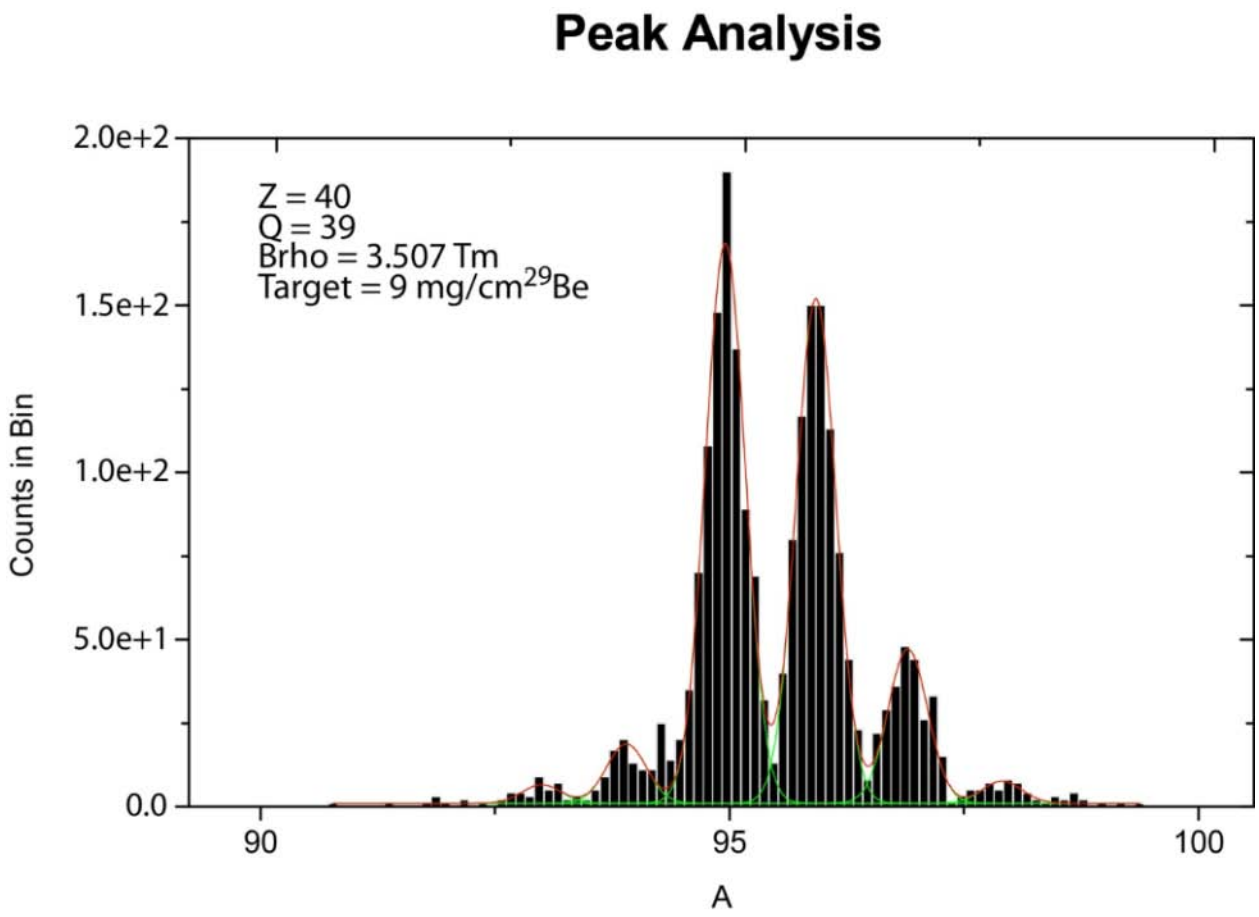

Figure 23: Gated data set fit to give number of counts for each mass number in set.

The series of one dimensional mass spectra generated by the gating procedure were then fit with a series of peaks, shown in Figure 23, using an automated fitting code to allow for the handling of the large amount of data in a relatively limited time. The mass spectra were particularly good for automated fitting due them consisting of a series of evenly spaced Gaussian peaks, allowing for easy exclusion of invalid data points. After the fitting the integrated number of counts contained in each peak gave a final result of the number of counts for each mass, charge, and magnetic rigidity in a setting.

To be able to plot each fitted data point as part of an overall spectrum we had to calculate several normalization factors to allow for a fair comparison. The first factor to be considered

was the total amount of beam incident upon the target during a particular data collection run. The NaI counters set at the target box generated a signal proportional to the number of beam particles striking the target. Due to each target thickness having a different NaI calibration and the difficulty in reliably combining momenta from different target thicknesses into the same spectra, as will be discussed shortly, the number of counts were normalized to a representative data run for each target.

Change of transmission from the nominal central momentum value due to off central momentum fragments is a correction that must be made. This problem has been studied in detail at GSI [Per00] and addressed in the Monte Carlo simulations of the code LISE++. Due to the importance of this correction a method to determine the momentum dependent acceptance was devised and will be presented in the results chapter. These results were used to correct the data for runs where a range of momenta were measured simultaneously.

Another important correction was for ion charge state distributions. Because all observed ionic charge states are not produced with equal probability, less favorable charge states will have a lower yield than their more favorable counterparts at a given momentum value. In order to properly generate a distribution from data points consisting of a mix of charge states this must be corrected for. To predict the amount of a given charge state expected to make it to the detection system a multistep calculation based upon the code GLOBAL [Scheid98] was used. To model the charge state creation process we have split the calculation up into three parts. In the first portion we treat the transmission of the primary beam through the first half of the target, calculating the probability for each primary beam particle to be in a given charge state. We then assume that the reaction takes place in the center of the target and assign the remaining primary beam electrons to the fragments proportionately to their nuclear charge. These fragments are

then transmitted through the second half of the target with a starting energy of the primary beam less the losses from transmission through the first half. Again GLOBAL is used to calculate the charge state distribution for a given initial fragment charge state. To get the total probability of a fragment charge state emerging from the target we then sum all possible paths in our calculation that lead to a given final charge state.

In the cases where a detector was placed in the beam path prior to the focal plane we needed to apply a further correction to account for charge exchange losses in the material. The charge states generated in the previous section were then recalculated after passage through the detector material assuming an initial energy that is reduced by passage through the detector. In this calculation however, we eliminate the fragments that do not exit the material with the same charge state that they entered with. This is justified by the fact that in most cases the fragment will not be transmitted through to the end of the separator after changing charge state. The surviving fractions were then multiplied with the initial production charge state fractions to give the portion of the full isotope production that would be expected to survive to the end detectors and be in a given charge state assuming no other losses.

In an earlier section we described that the data sets were gated upon the magnetic rigidity in the second portion of the separator. While in the cases where no material is present in the beamline such as the narrow momentum acceptance settings the first and second half rigidities are identical, when material is present the first half rigidity must be calculated in order to determine the fragment momentum. Before calculations could be done, an effective thickness of the beamline material needed to be determined. This was done by taking a small sample of isotopes from the data set where the first and second half rigidities were known and adjusting the calculated thickness of the material based upon energy loss in the material using the code

ATIMA, until the x-position of the fragments matched between the entrance of the material and the exit. Once the effective thickness was determined the rigidity in the first portion of the separator could be determined using the code ATIMA. Since the code only calculates energy loss, in order to calculate what the energy must have been before the material in an efficient fashion we relied upon the approximation that the energy loss per unit length in a material is approximately constant for a thin material at high energy. Taking this into account, we generated a table of energy losses in the material for all isotopes in the rigidity occupied by the final products and added the energies from this table to generate the appropriate first half rigidities. Once the rigidities were determined the momentum for each data point was calculated using the formula (5) where Brho represents the first half magnetic rigidity and Q is the integer value described earlier.

With the corrections and normalizations applied and the momenta calculated we then grouped the data together by mass, nuclear charge and target thickness to generate partial momentum distributions. Immediately after the reaction, the momentum distributions of the fragments should be identical independent of the target thickness. As the fragments are transmitted through the target however interactions with the target material distort the distributions by reducing and spreading the overall momentum. Because the reaction can occur at any place in the target material, the distortions are not uniformly applied to the fragments and increase in magnitude the earlier in the target that the reaction occurs. This means that the thicker targets suffer more of an overall reduction to the produced momentum as well as a wide spread in the distribution since there is a wider range in which the reaction can occur. There is no reliable way to unfold the target contributions outside of a series of models and hence we present the data for the three targets separately.

5. Results

In this section we will present the results of the experimental analysis. Beginning with the particle identifiaction, we will then present each portion of the data and compare them with theoretical predictions and results from previous experiments. Following the particle identification we will examine fragment transmission, momentum distribtutions, partial cross sections and finally total cross sections for a selection of isotopes determined from our experiments. These will be compared to LISE++ predictions and data taken from experiments at GSI and RIKEN.

5.1 Data Particle Identification

As described in the previous chapter the idetification of atomic number, Z, mass (and hence inferred atomic mass, A), ionic charge state, Q, and momentum, p was carried out ion by ion for all data sets collected for this experiment. The A1900 parameters and targets for the data sets used in the analysis are shown in Table 4. Listed are the spectrometer magnetic rigidities for the first and second halves of the A1900 (Brho12 and Brho34, respectively) and corresponding targets. As discussed previously the presence of the scintillator allows for velocity measurement

of fragments when the dp/p is large but reduces the momentum of the fragments and allows only a subset of fragments to be detected at the focal plane.

Figure 24 below shows the particle identification spectra for all settings used for the momentum distribution meausrements, with the specific configuration used for each setting is given in Table 4. The figure illustrates that a unique A and Z can be determined for each ion. Only settings where the A, Z, and Q identification was sufficient for automated gating and fitting were accepted into the final data set. The automated gates required that the identification plots maintained a regular pattern throughtout the data that was consistent between settings so that a universal set of gates could be applied rather than custom generating gates for each setting.

As is shown later in this chapter, the pariticle identification plots are consistent with results from RIKEN. From the particle identification plots shown in Figure 24 one can get a general impression of the range of fragments produced in fragmentation-fission. These data sets are consistent with the predictions of LISE++ to which a representative set is compared in Figure 25. A subset of these data were taken without material (the scintillator) at image two and hence represent the full range of fragments produced at the corresponding magnetic rigidity. As opposed to that observed for Coulomb Fission [Donz98] the data show a more symetric distributions of fission fragments. This is consistent with the expected high excitation energy imparted to the pre-fission nuclei produced in the fragmentation step. In this case the fission barrier and shell effects do not play a large role.

However there are differences depending on rigidity. Notably setting 1054 (low rididity and close to the peak of the fission yield) shows a nearly completely symmetric distribution while setting 1118 (higher rigidity and set for more neutron-rich fragments) shows a more

asymmetric one. This could possibly be due to a stronger than expected contribution of lower excitation energy fission than what is expected from the simulations.

Table 4: Spectrometer settings and targets used for the data collection settings shown in Figure 23. Brho12 and Brho34 represent the magnetic rigidity of the first and second halves of the spectrometer respectively.

Setting	Brho1,2 (Tm)	Brho3,4 (Tm)	Target (mg/cm^2)	Scintillator	dp/p %
1054	2.75	2.75	9	no	0.2
1085	3.78	3.72	47	yes	4.0
1087	3.78	3.7	47	yes	4.0
1088	3.78	3.7	47	yes	4.0
1095	3.72	3.66	47	yes	2.0
1096	3.72	3.66	47	yes	4.0
1103	3.72	3.66	47	yes	4.0
1112	3.55	3.55	9	no	0.1
1113	3.3	3.3	9	no	0.1
1117	3.72	3.66	47	yes	4.0
1118	3.7	3.64	94	yes	5.0
1145	3.51	3.51	9	no	0.1
1146	3.47	3.47	9	no	0.1

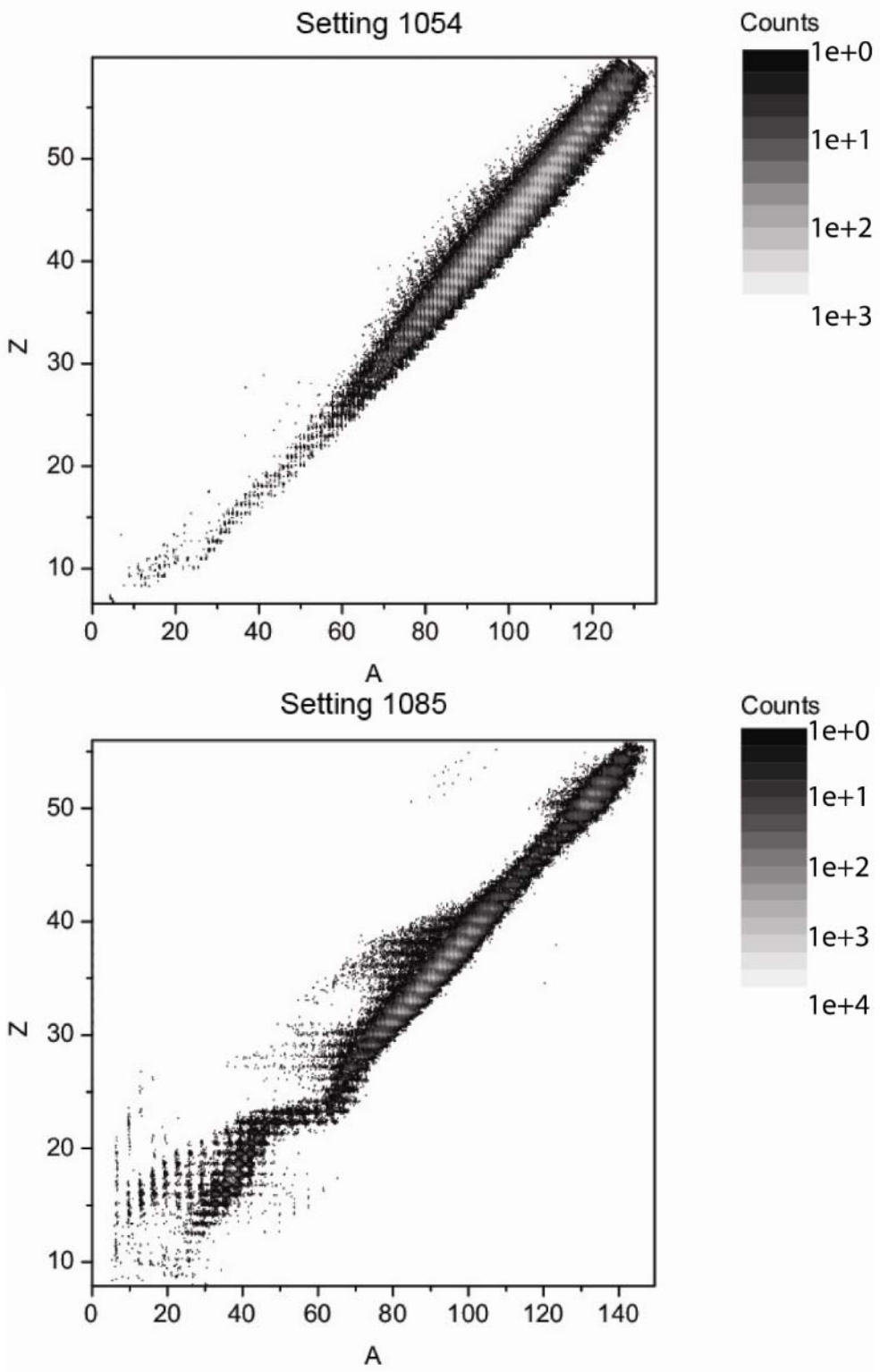

Figure 24: Particle identification (Z vs. A) plots arranged by experimental setting.The parameters corresponding to the experimental settings is given in table 4.

Figure 24 (Cont'd)

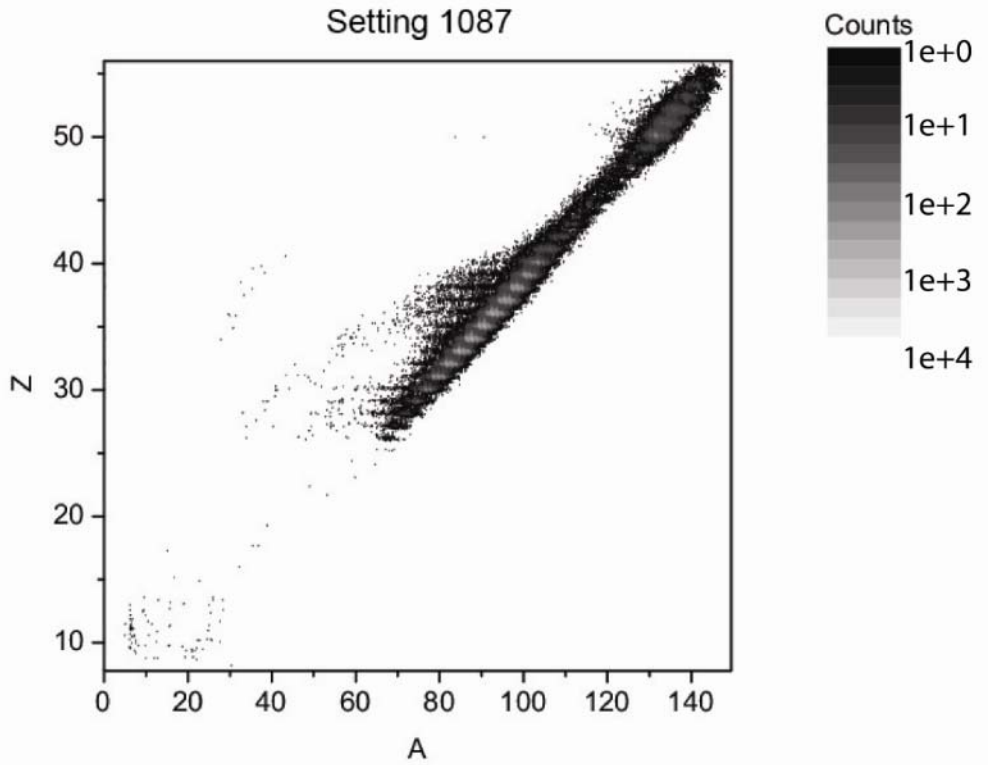

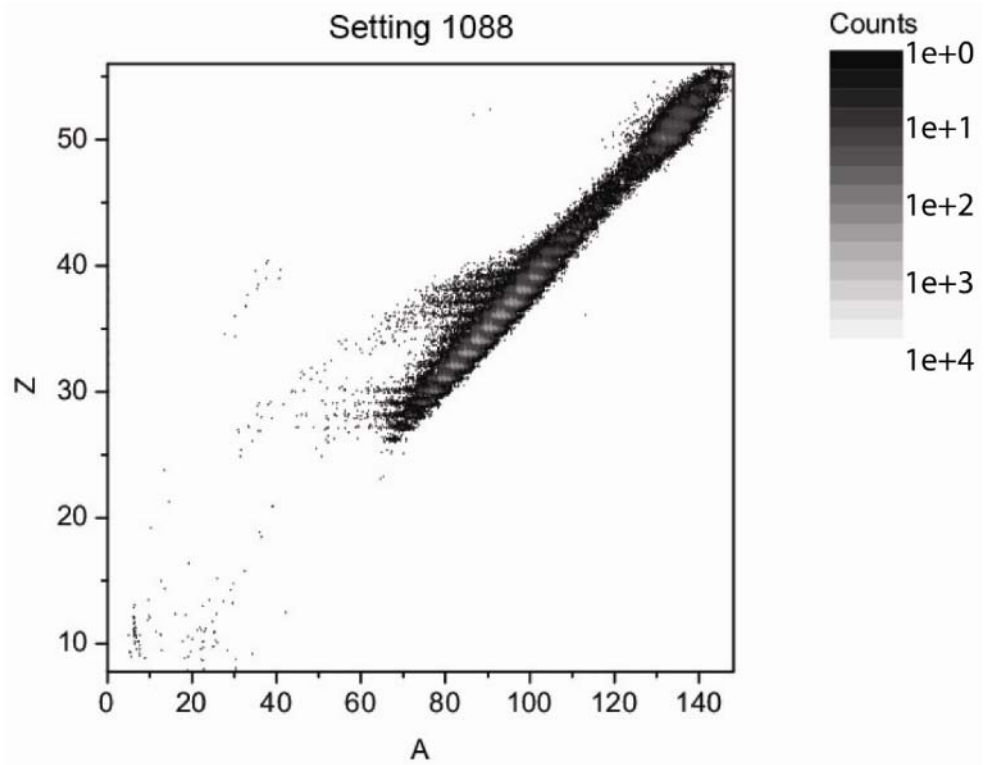

Figure 24 (Cont'd)

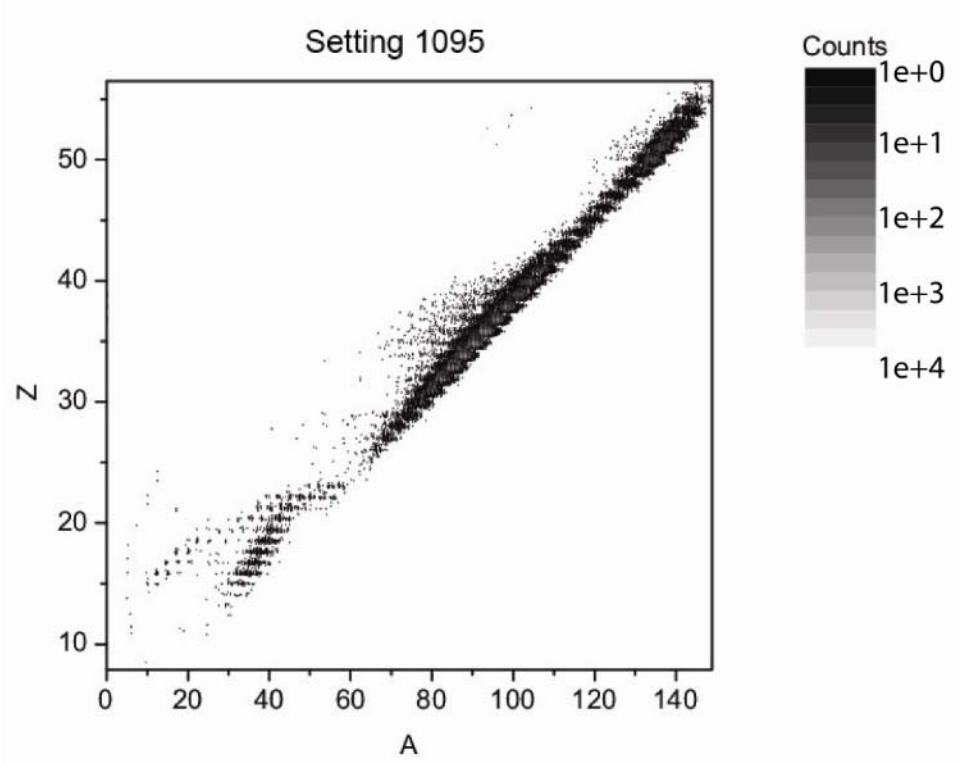

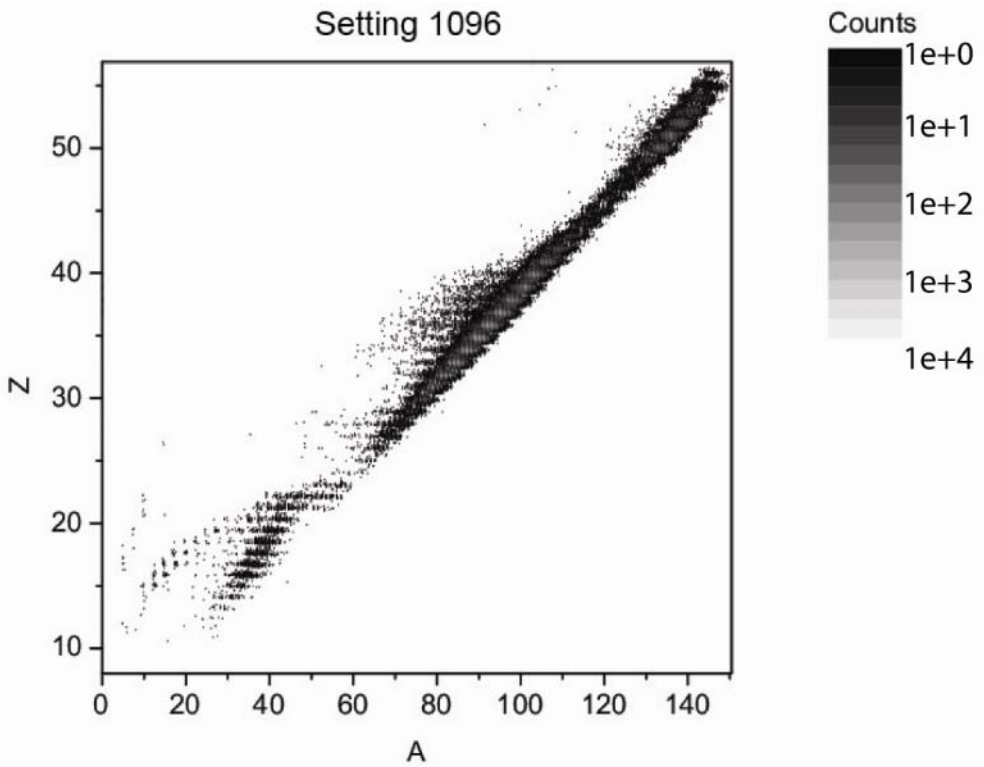

Figure 24 (Cont'd)

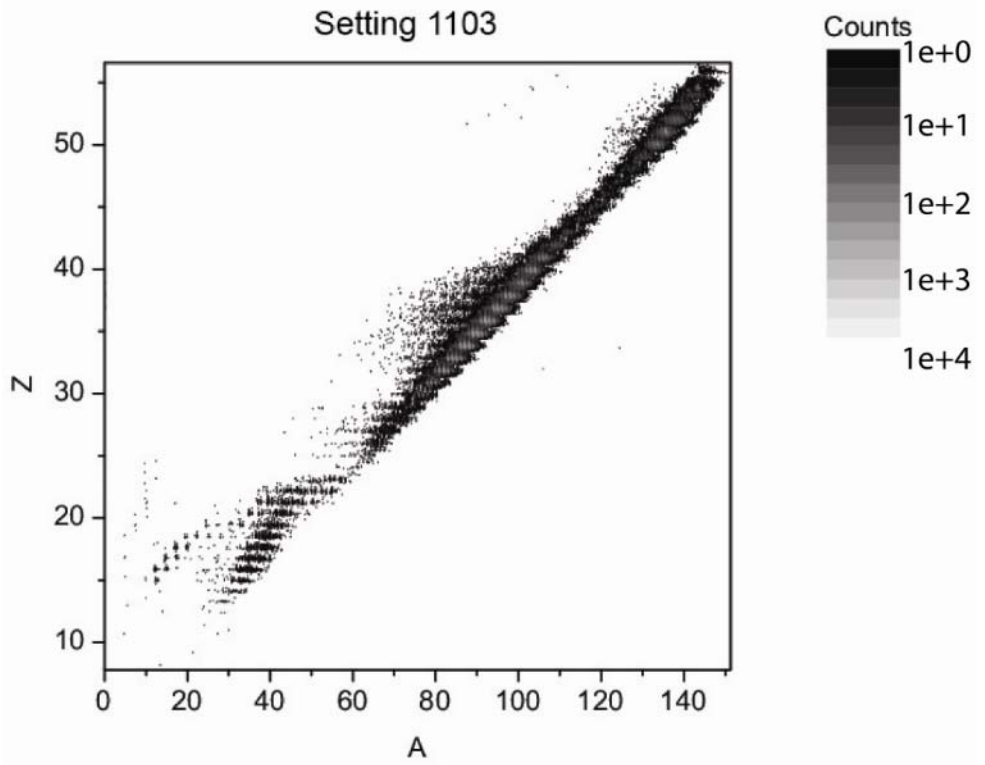

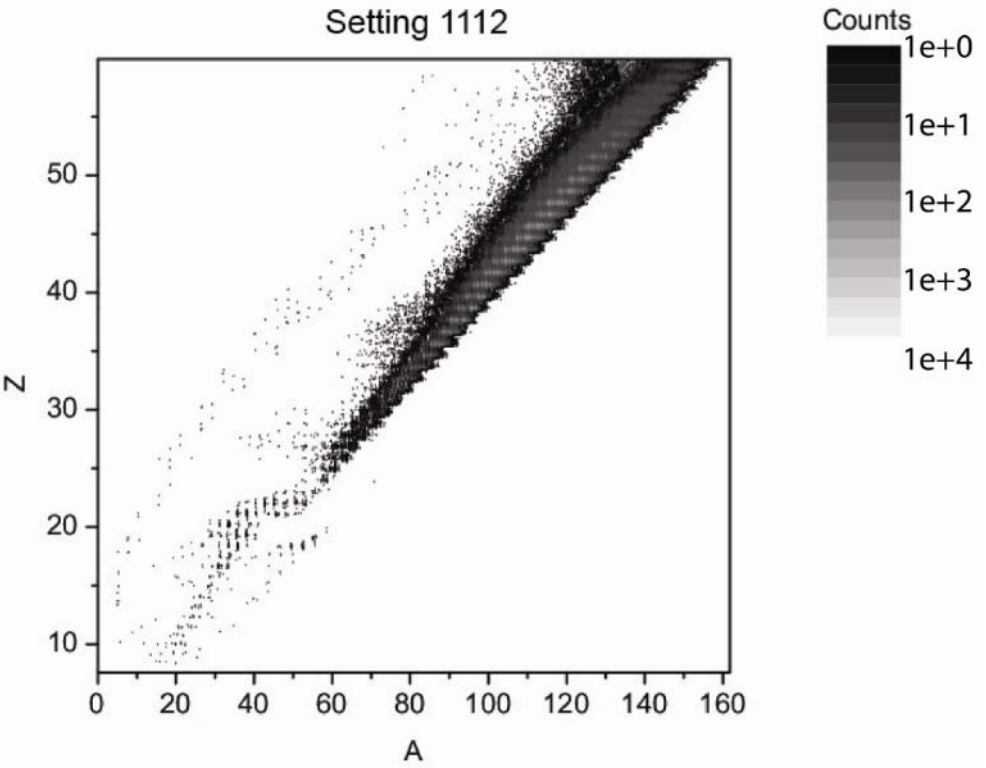

Figure 24 (Cont'd)

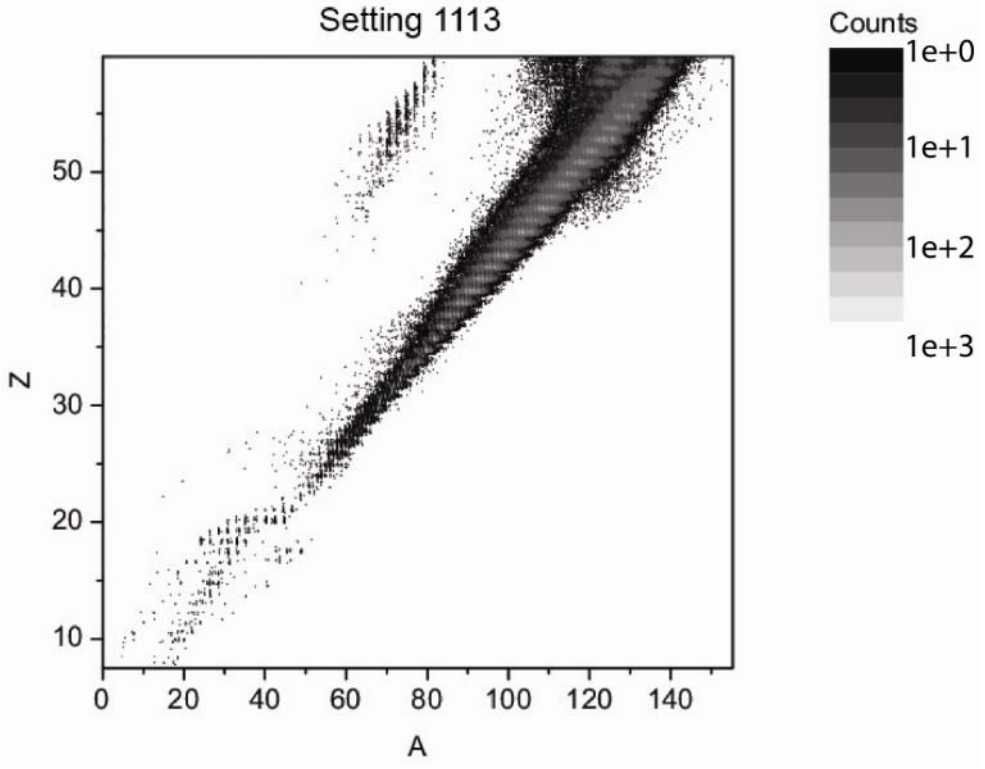

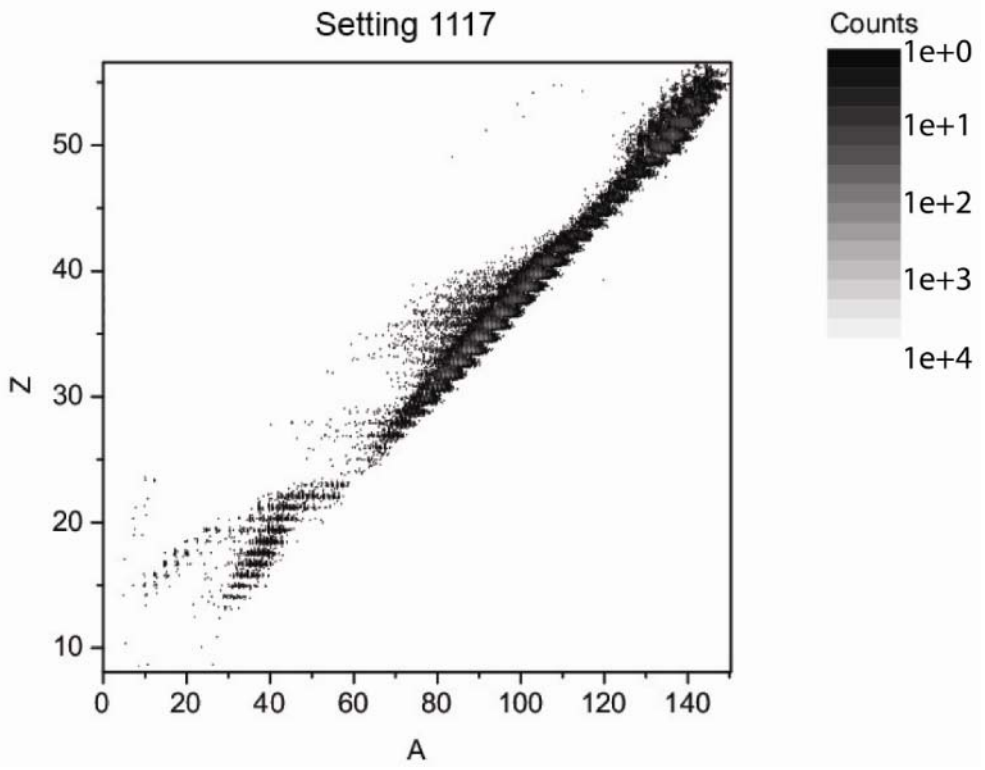

Figure 24 (Cont'd)

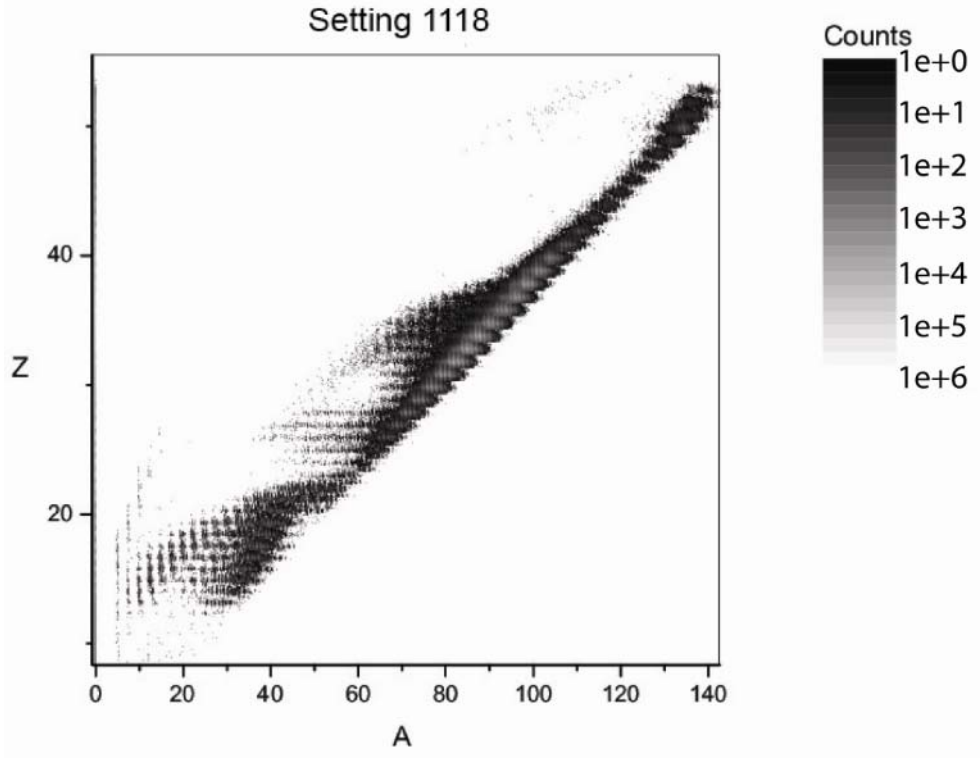

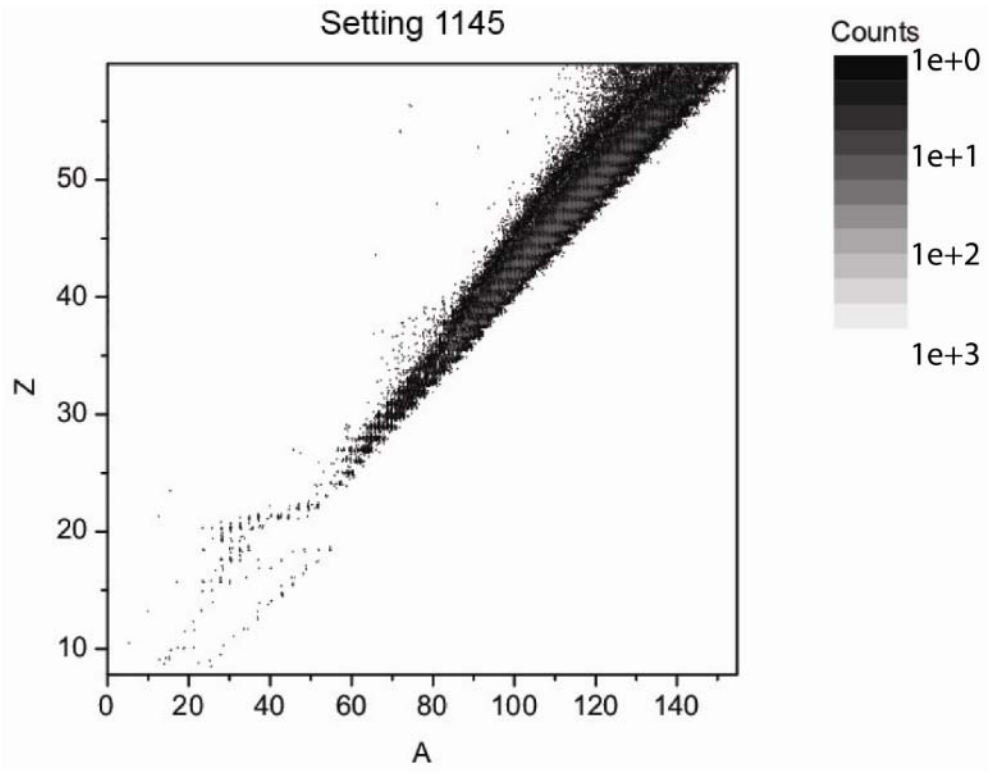

Figure 24 (Cont'd)

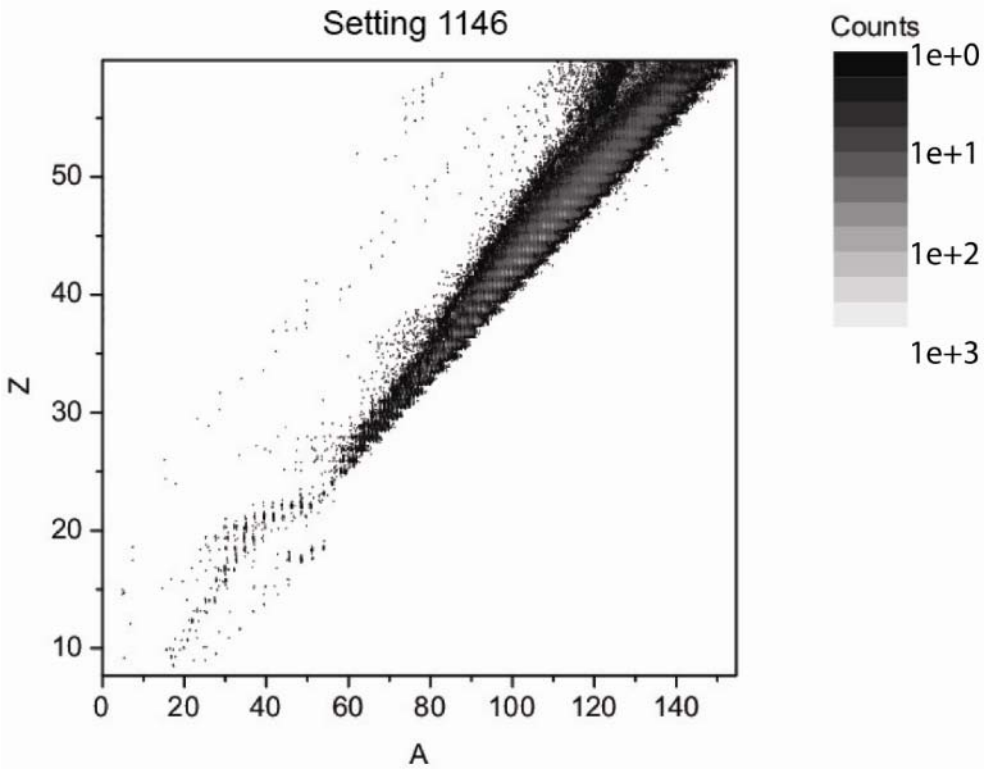

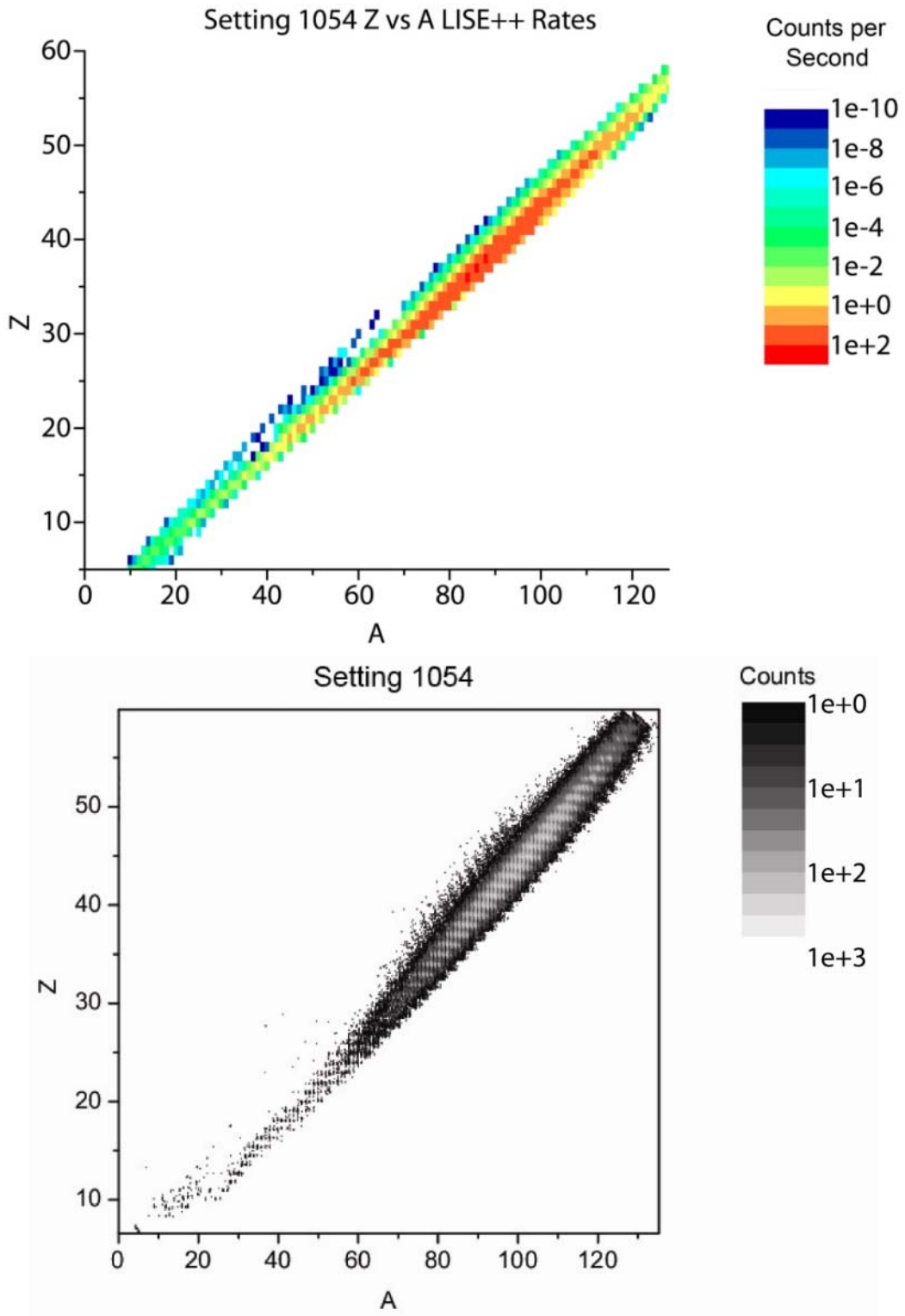

Figure 25: Comparison of LISE++ simulations to the experimental setting. Due to the energy loss detectors saturating, the system was not sensitive to Z > 60 and these data were excluded. Generally there is excellent qualitative agreement between the LISE++ preductions and the observed Z and A distributions.

Figure 25 (Cont'd)

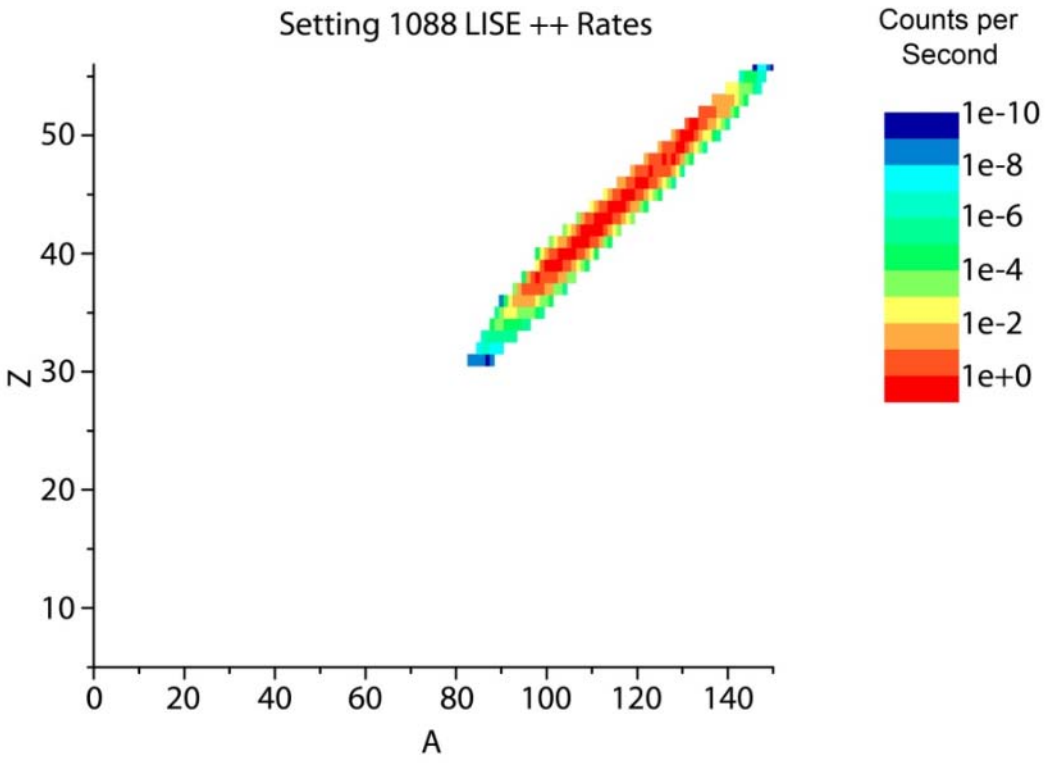

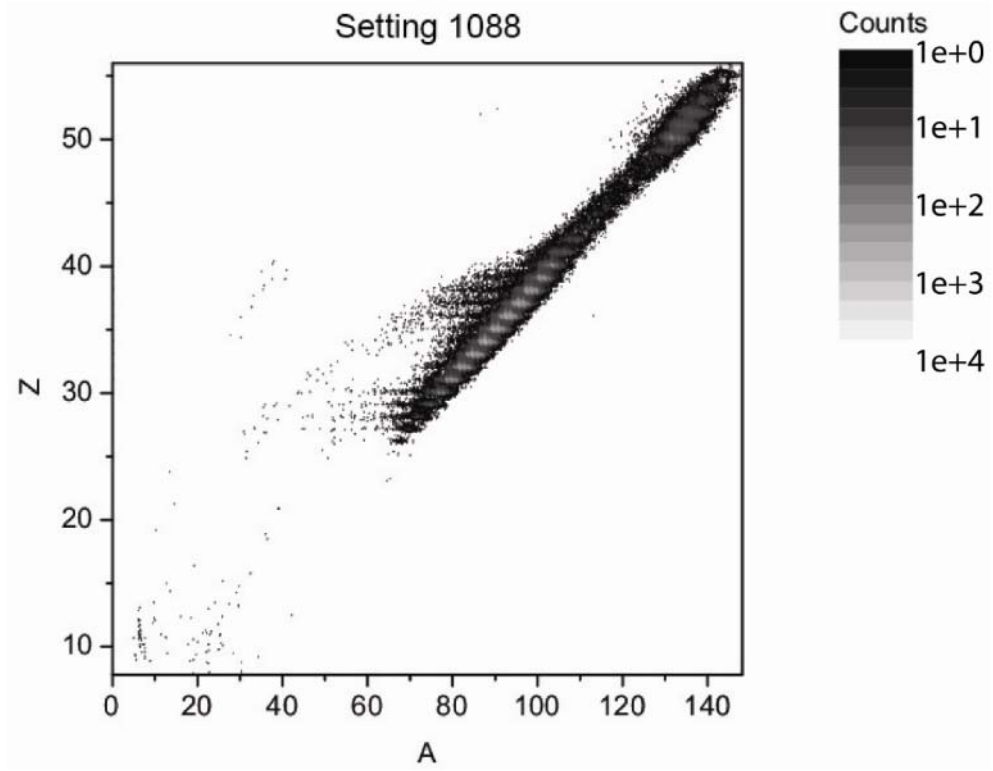

Figure 25 (Cont'd)

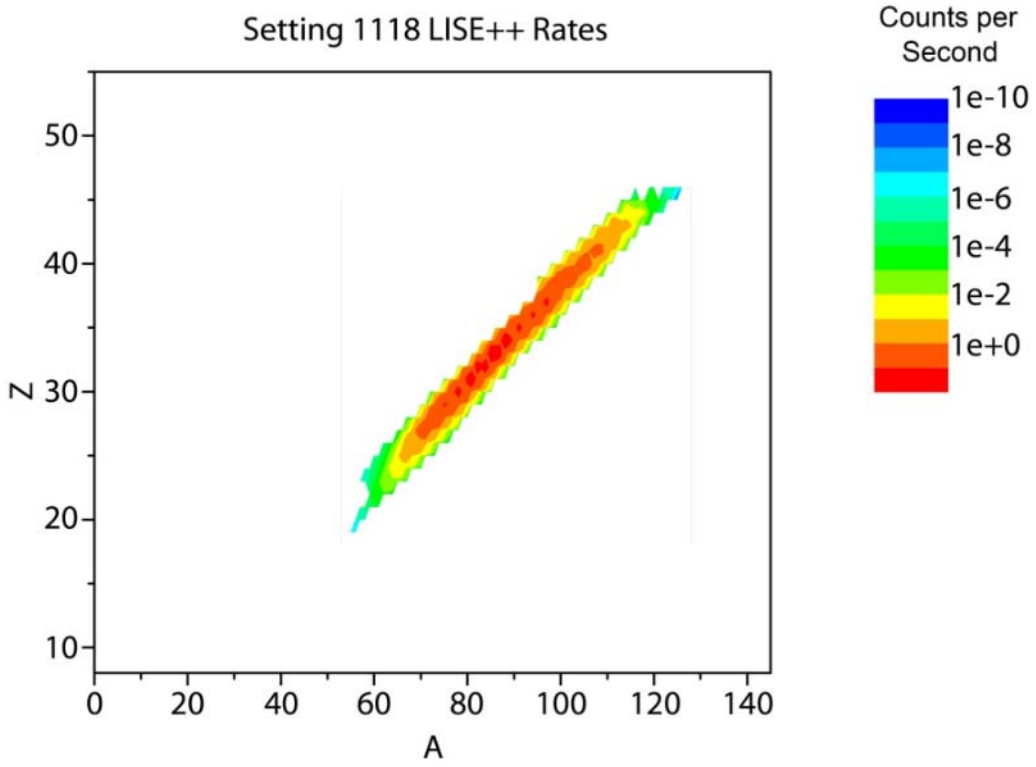

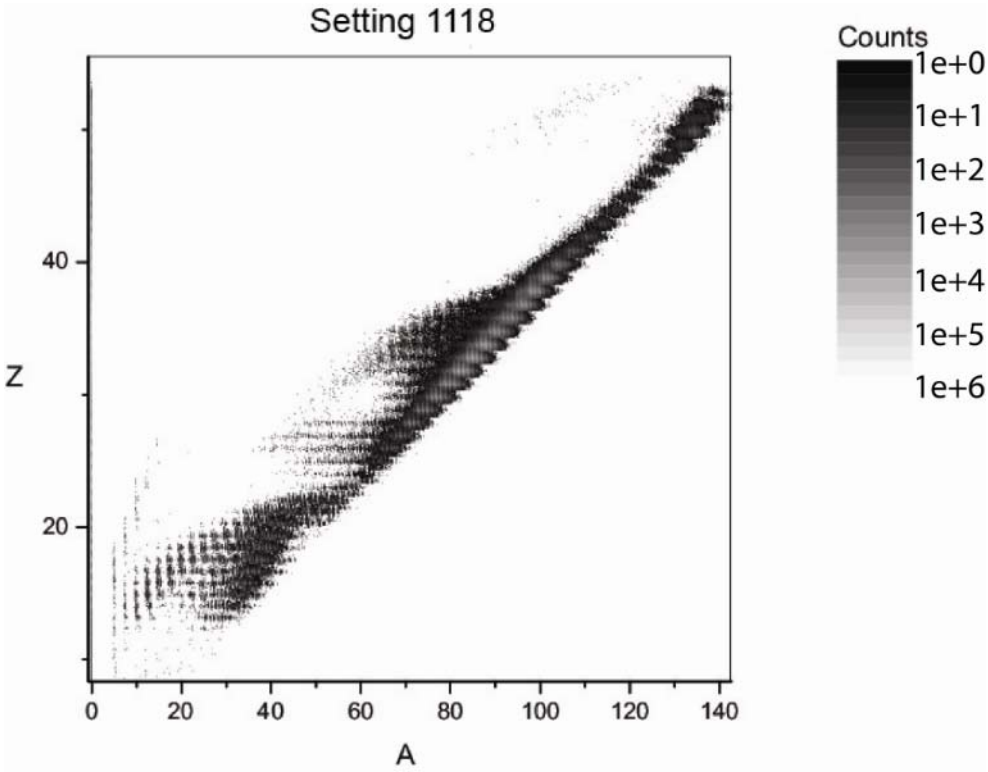

Figure 25 (Cont'd)

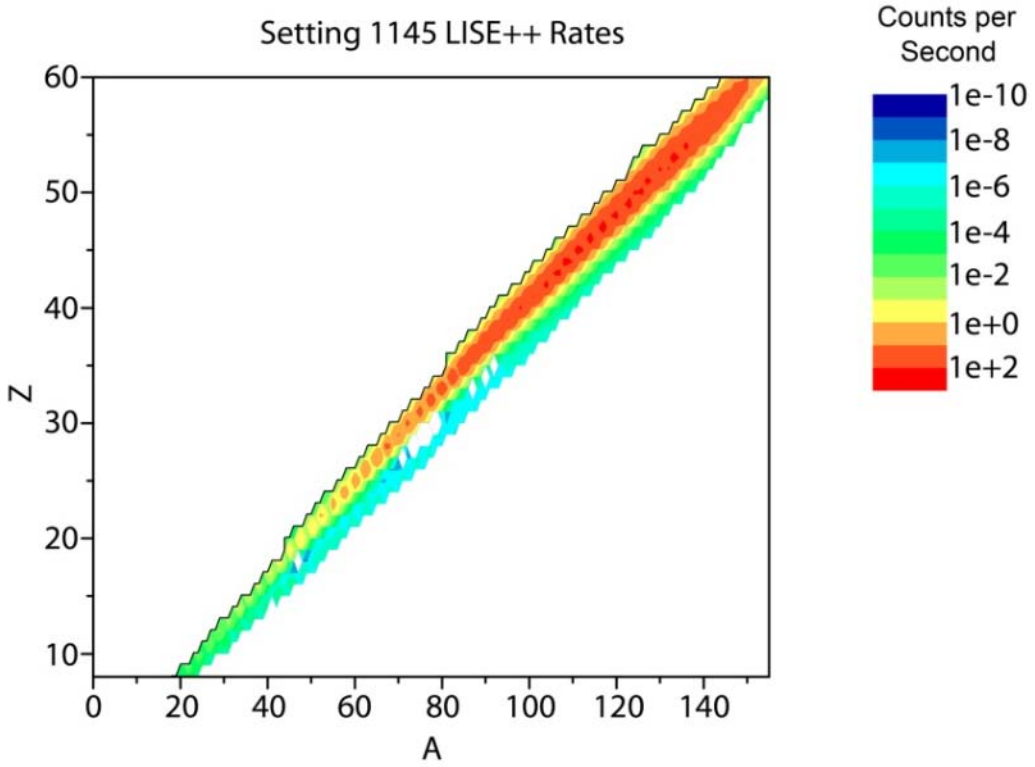

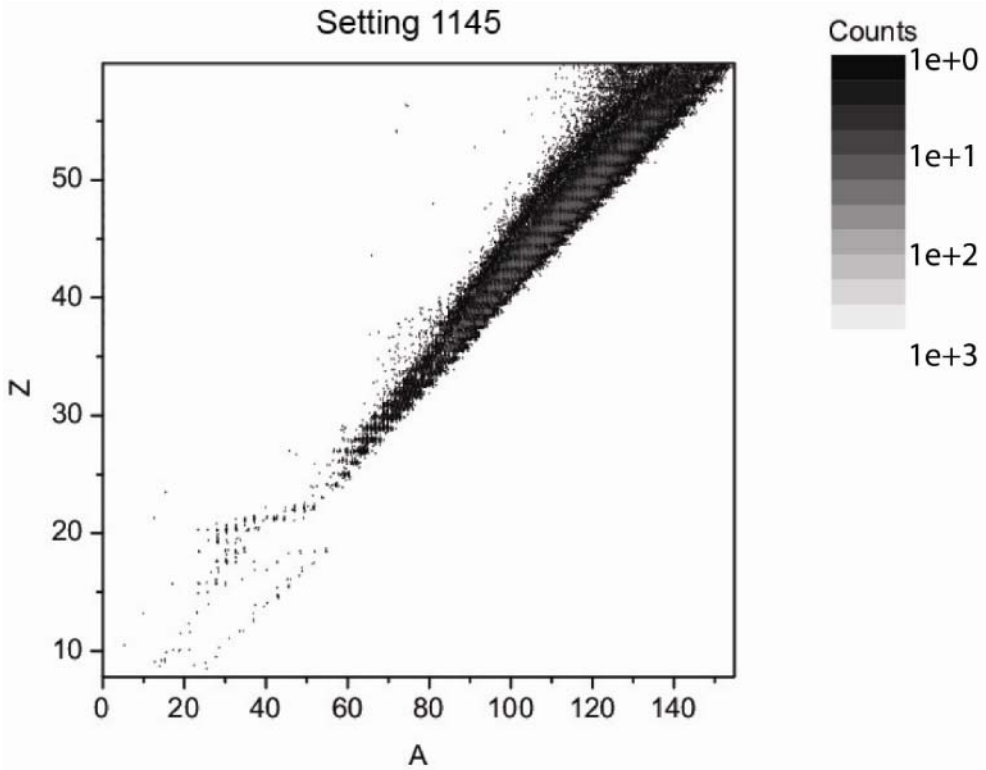

5.2 Transmission

To determine the differential production cross section as a function of momentum, for each fragment A and Z, it was necessary to accurately simulate the transmission of the generated isotope at the target to the focal plane of the A1900. For this purpose we used the Monte Carlo transmission function of the code LISE++. As mentioned previously, LISE++ simulates production of isotopes through fragmentation fission by treating the reaction as proceeding from three representative fragmentation products in the first stage, referred to here as "prefragments". These prefragments are modeled to undergo fission by the code and their final products are calculated. The prefragments themselves are selected by the code weighted by their fragmentation cross section and a mass and charge range designed to give reasonable coverage of the observed fission products measure at GSI. We elected to use the default parameters in the LISE++ fission models which were selected to match the GSI results.

5.2.1 Momentum Distributions

Measurement of a complete momentum distribution for an identified particle is not possible at the NSCL using the A1900 spectrometer due to the angular acceptance but the complete momentum range populated by the fragments can be measured. The spectrometer can be set to let particles of a certain momentum to charge ratio pass to the detection system allowing for a snapshot of the number of fragments for a particular isotope that are generated with that momentum value. The settings can then be scanned to cover the entire region of generated

momentum values giving a profile of the entire distribution after the settings are rate normalized to one another. After a complete scan the data set would give a distribution similar to Figure 26. Combining the quick setting adjustment times with the high beam rate it is possible to measure these distributions for a large number of fragments in a relatively short period of time compared to previous experiments where a lower beam intensity required sitting on a particular setting longer to generate the same number of statistics. It should be noted however that, since fragmentation-fission is a multistep process with no measurement of the intermediate steps, the measured momentum distributions are those for the entire process, not just the fission reaction. Figure 26 shows the comparison between the total theoretical momentum distribution of the selected fragments with the fragments expected to be observed after transmission. The simulation was done by the LISE++ code with the gray areas representing the region covered by the data collection settings in the experiment. From these simulations we calculated the transmission factors used to integrate the measured partial distributions (gray area) into the total production cross sections.

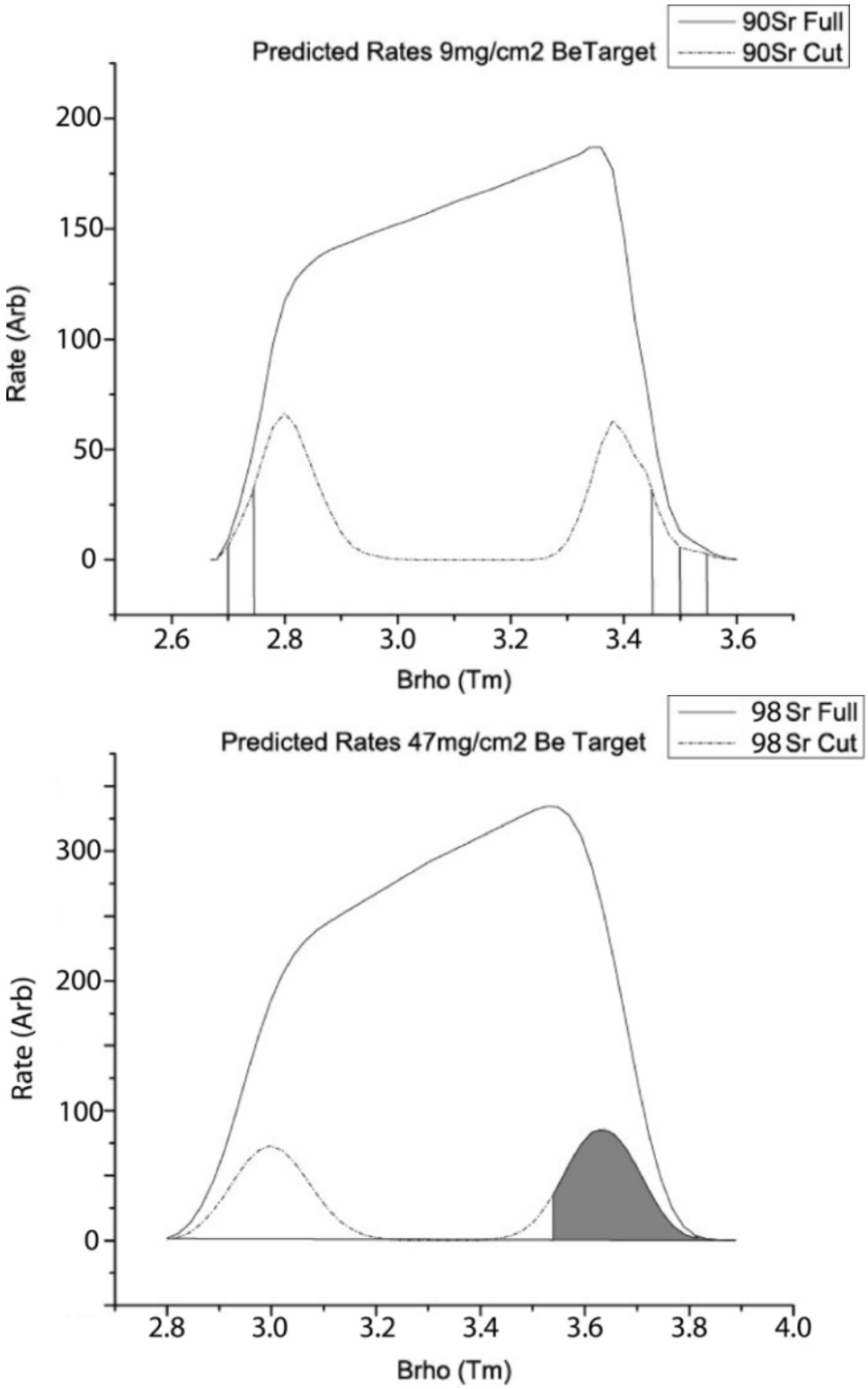

Figure 26: Regions of momentum distributions covered in experimental plan taken for representative targets. The full line represents predicted total momentum distribution for fission fragments while the broken line shows the same distribution with transmission cuts applied. Gray areas and lines represent regions where usable data was taken.

Figure 26 (Cont'd)

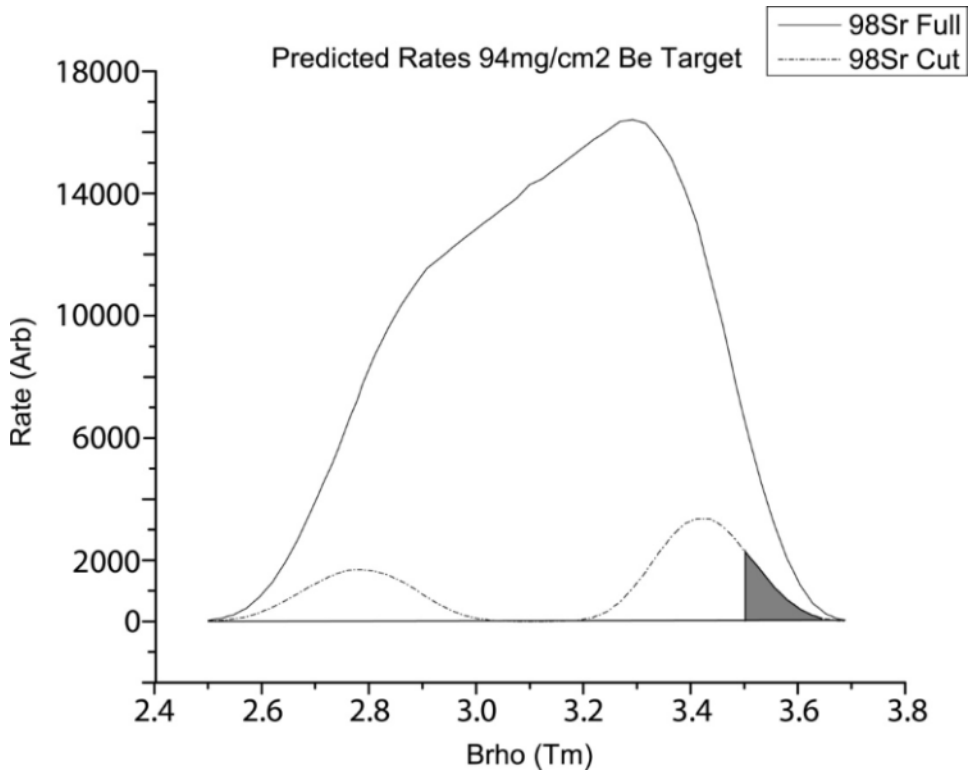

5.2.2 Angular Distributions

The angular and momentum range are set by the energy released in the fission process, which is in turn determined by the division of excitation energy between internal excitation of the fragments and the fission decay energy. Typically a separator such as the A1900 has a angular acceptance below that of the fission fragment angular spread and hence only a small fraction of the fission fragments can be collected. In the case of the A1900 only 2-5% of all fragments produced can be collected.

Due to the large phase space of fission fragments, a detailed understanding of the separator acceptance is needed to reliably extract cross sections. What can be clearly seen in

Figure 28 below is that fission presents unique fragment collection challenges. The broad distributions of fission products in both angle and momentum space require at least doubling or even tripling of the acceptance for fragmentation reactions in order to achieve a similar production rate. Design of facilities utilizing fission as a production reaction therefore require detailed knowledge of the shapes of the fragment distributions to ensure maximum collection.

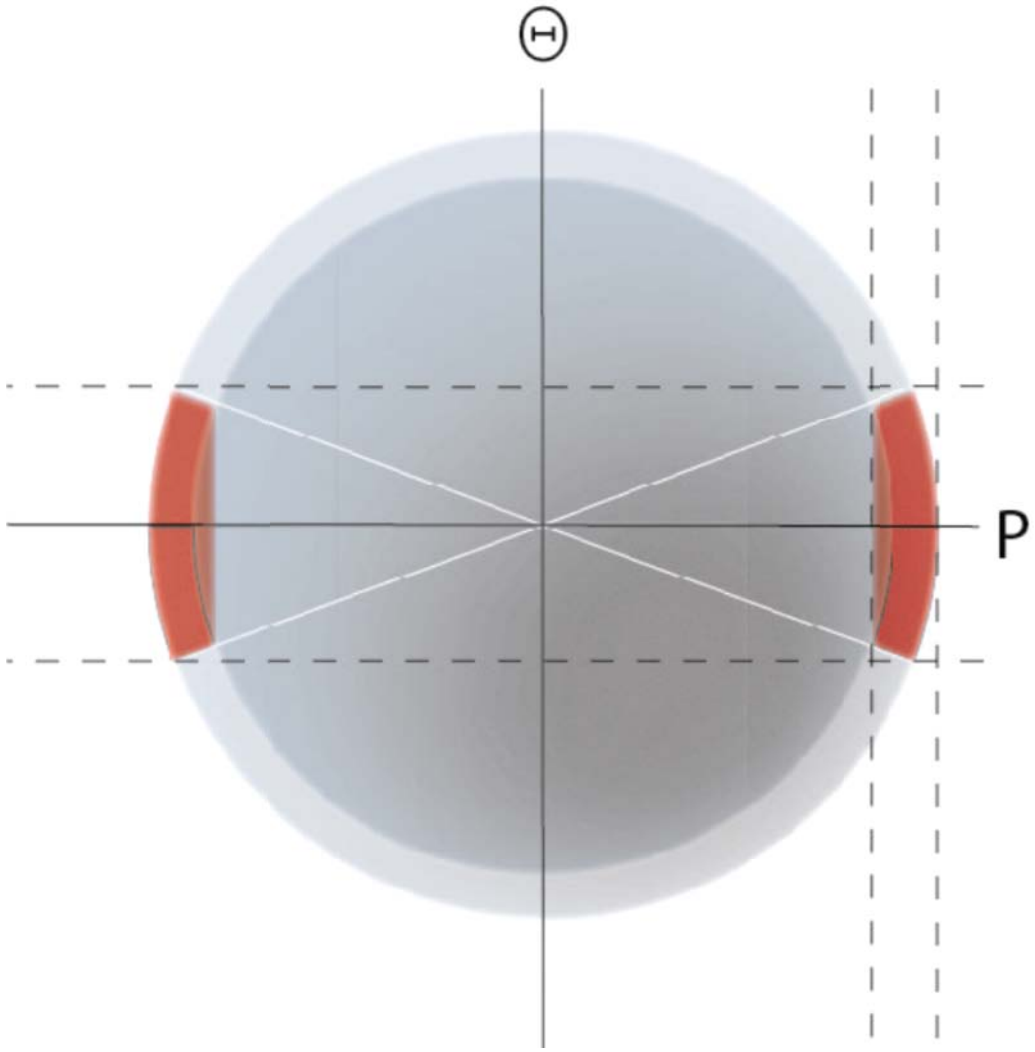

Figure 27: Schematic of a fission fragment distribution in the Center of Mass frame. The dashed lines represent separator acceptance in angle and momentum. The forward red region represents the transmitted fragments observed in this work.

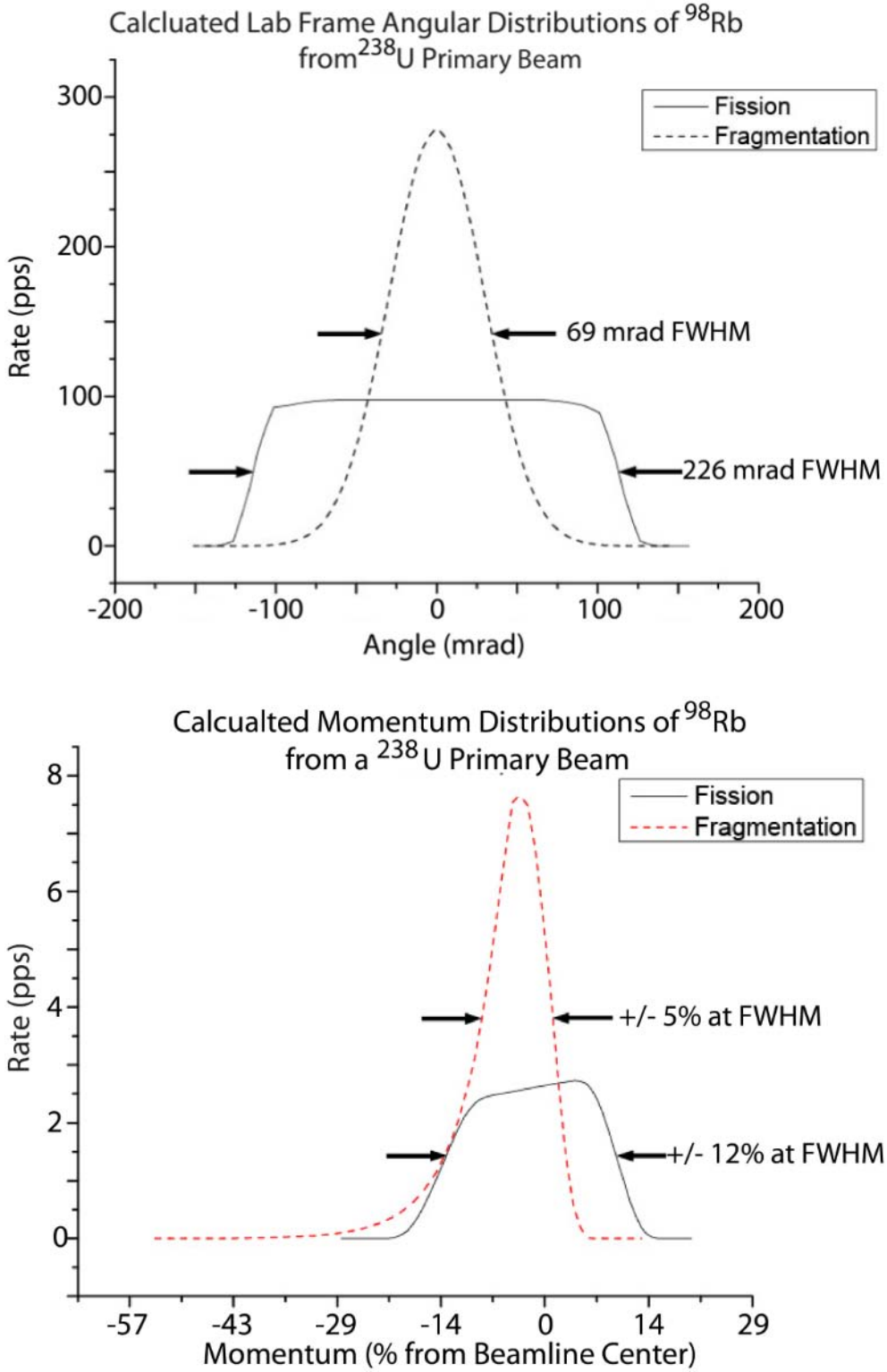

Figure 28: Comparison of the lab frame fragment momentum and angular distributions in fission and fragmentation calculated with LISE++. Typical acceptances for the best fragment separators (such as the A1900 at the NSCL) are ±50 mr in angle and ± 2.5% in momentum. One can see from the figure that it is impossible to accept the full fission yield with such a device.

The angular distributions of the fragments and the angular acceptances of the A1900 as a function of rigidity relative to the central momentum were needed to account for the losses during transmission through the separator. The model for the angular distribution of fission products assumes that the fragments are symmetrically distributed in their rest frame and then focused when boosted into the laboratory frame, and should be very reliable. Because of the accuracy of this part of the model we elected for this work not to place detectors in the system to record angular data in order to eliminate as much material from the flight path as possible which allowed for maximum fragment collection at the focal plane detectors. We confirmed our assumptions by comparison of our momentum distributions to the LISE++ transmission predictions using the spherical emission model. As will be seen in the results section, the results match prediction well indicating that the assumed spherical angular distribution and resulting transmission losses correspond with the experimental results.

Our simulations utilized the 5^{th} order ion optical calculations available in the code. We found that the 3^{rd} order calculations gave a reasonable approximation of the data, as seen in Figure 29, and that there was little difference using the 5^{th} order matrices; however use of the higher order did not add significant calculation time and these were used for all comparisons. Of note is that calculations of 3^{rd} order and above successfully reproduce the transmission losses for off momentum transmission. This comparison provides confidence that we can use the wider momentum acceptance of the A1900 to measure the fission momentum distributions. While the Monte Carlo code also allows the calculation of charge exchange losses in material, the additional computation time was prohibitive and we elected to utilize the charge state method

discussed in the previous section. In test cases the difference in loss estimates was found to be less than 5% between the Monte Carlo loss calculation and the GLOBAL calculation.

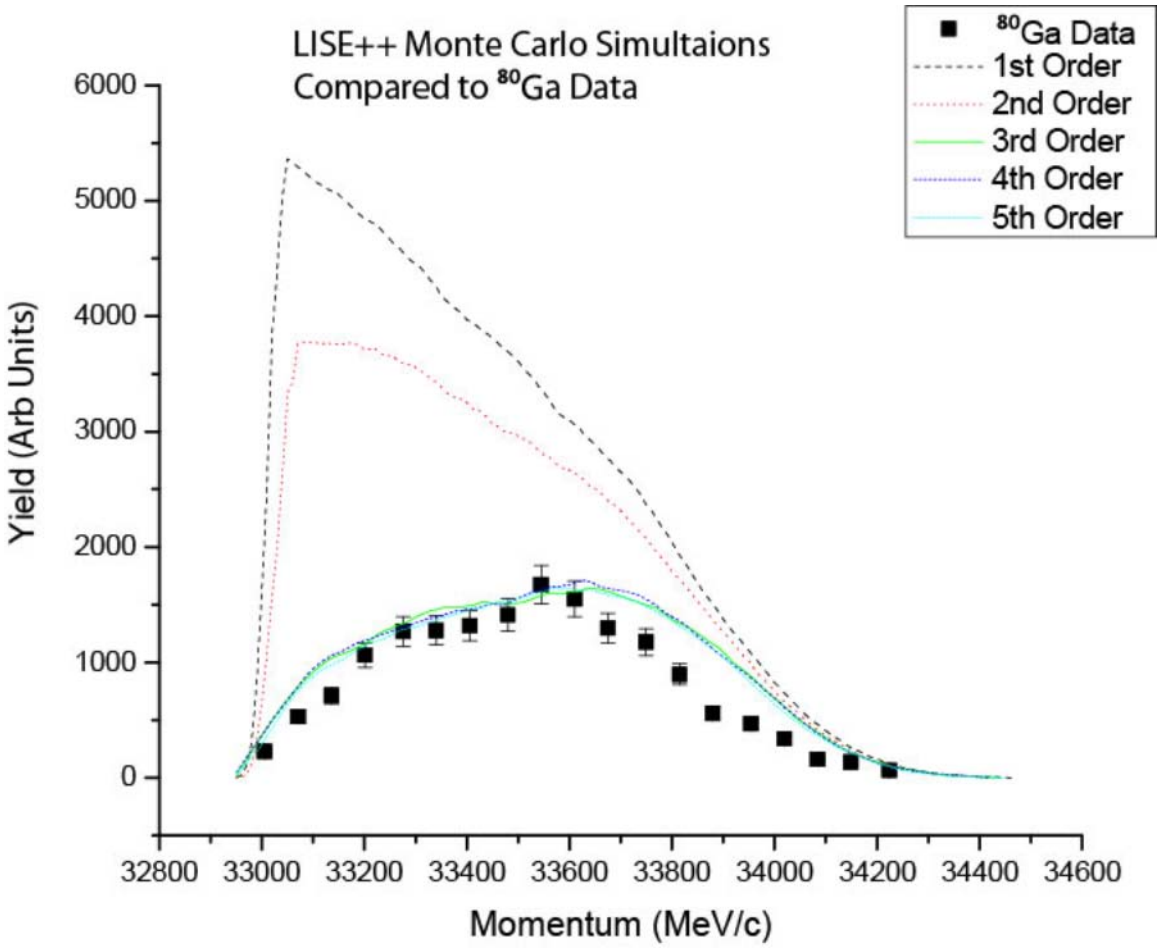

Figure 29: Comparison of Monte Carlo transmission simulations by LISE++ based upon optics order with a partial ^{80}Ga momentum distribution. In this case the central momentum of the A1900 was set to 34200 MeV/c. The LISE++ fission model predicts that the yield should rise for lower momentum. The observation that the data does not have this trend is due to the limited solid angle of the A1900 for off central momentum particles, as illustrated in the figure. The figure also shows that at least third order should be used in the simulations to provide accurate results.

The momentum dependant solid angle is a significant correction for the data and it was important to find an independent confirmation of the losses predicted by LISE. We were able to

do this by selecting isotopes that should have a linear dependence of the cross section with position at image 2. The leading edges of fission momentum distributions are expected to have linear slopes based on geometric considerations taken from the fact that the fission fragments uniformly fill the angular acceptance. This slope is seen in the first order simulation in Figure 29. The actual data compared to a linear extrapolation of the yield from the central data provides a ratio of expected to actual observed yield. This ratio can be converted into an expected fraction of predicted yield, as is shown in Figure 30. The error bars are due to statistics and an error estimate from the extrapolated slope of the central data. As shown in the figure for two representative cases, the LISE++ 5^{th} order Monte Carlo model does a good job of predicting the transmission losses. This data was then used to determine the effective solid angle of the A1900 as a function of momentum. The result is given in Table 5 and these values were used to determine double differential cross sections for selected fragments.

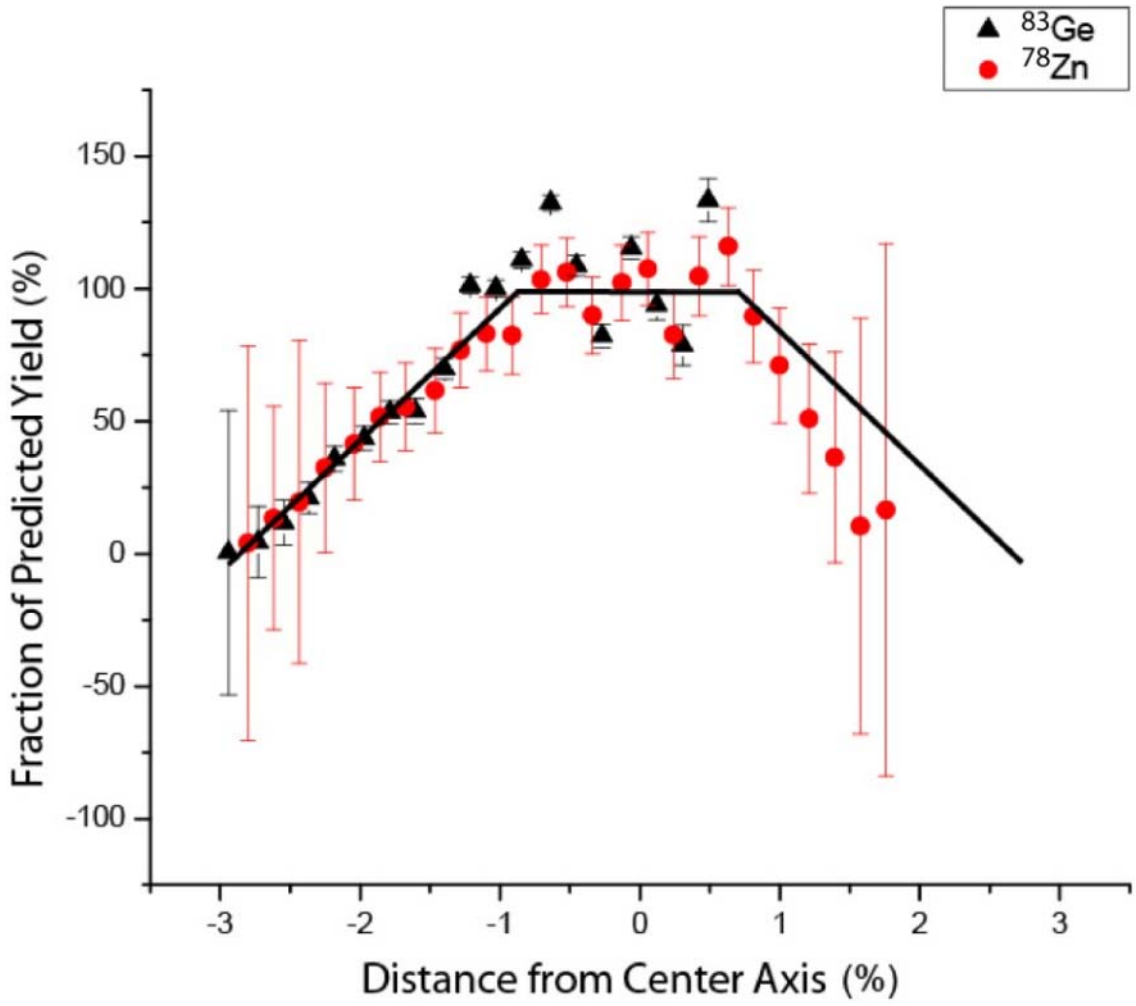

Figure 30: Experimentally determined transmission through the A1900 relative to LISE++ first order predictions as described in the text. The solid line is the predicted fraction taken from a 5th order LISE Monte Carlo Simulation. This demonstrates the loss of transmission as the fragments are transmitted further from the central axis which is accounted fo in higher order LISE++ calculations. Notably only the region of +/- 1% has essentially the predicted first order transmission.

Table 5: Experimentally determined solid angle of Transmission as a function of momentum relative to the central axis. This table assumes a central solid angle for the A1900 of 10 msr.

% from Center	% of Nominal	Solid Amgle (msr)
-3	0	0
-2.5	19	1.9
-2	41	4.1
-1.5	64	6.4
-1	86	8.6
-0.5	100	10
0	100	10
0.5	100	10
1	86	8.6
1.5	64	6.4
2	41	4.1
2.5	19	1.9
3	0	0

The particle ID and integration methods described in the previous chapter were used to construct fragment momentum distributions for over 300 fission fragments. Data were combined for different A1900 magnetic rigidity settings and charge states, but not for different Be target thickness (for the reasons described previously).

A representative set of extracted momentum distributions is shown in Figure 31. As shown in the figure, the observed distributions match the shape of the predictions of LISE++ 5th order Monte Carlo calculations using the default reaction model reasonably well. Note that the magnitude of the LISE++ predictions were scaled to match the data. The amount of the scaling will be discussed below, and can be used to determine the total production cross sections for each fragment.

Three details are of particular importance in Figure 31. The first is the start of the low yield tail on the right hand side of the plot. For the settings we have chosen in this figure the tail

region falls near the center of the separator where transmission is assumed to be only affected by the lower order effects and therefore very well modelled. Additionally, this region does not contain any mechanical cutoffs from the momentum slits. What we see from this data is that the model is predicting the shape and endpoint of the momentum tail extremely well indicating the model is correctly predicting the fragment momentum after the reaction. The second significant detail is the peak value in yield, the peak position and shape depend on the calculation of the transmission properties of the separator as the fragments travel further from the center. In the cases above, the peaks line up with prediction well, indicating that the producation and transmission model used in LISE++ is working. The third characteristic of the above plots is the low momentum cutoff. This is caused by the physical slits in beamline blocking transmission below a certain value of momentum. Matching the distribution endpoints, the low cutoff and high tail, shows that the data and model are in agreement about the slit positions and the magnetic rigidity of the separator which confirms the calibration. The final distribution is a product of the initial distribution and the transmission losses. While the data does not match the predictions perfectly, it matches reliably enough to give credence to the model predictions. This is significant because it provides confidence in the LISE++ transmission calculations to determine losses which will are then used to determine the isotopic production cross section.

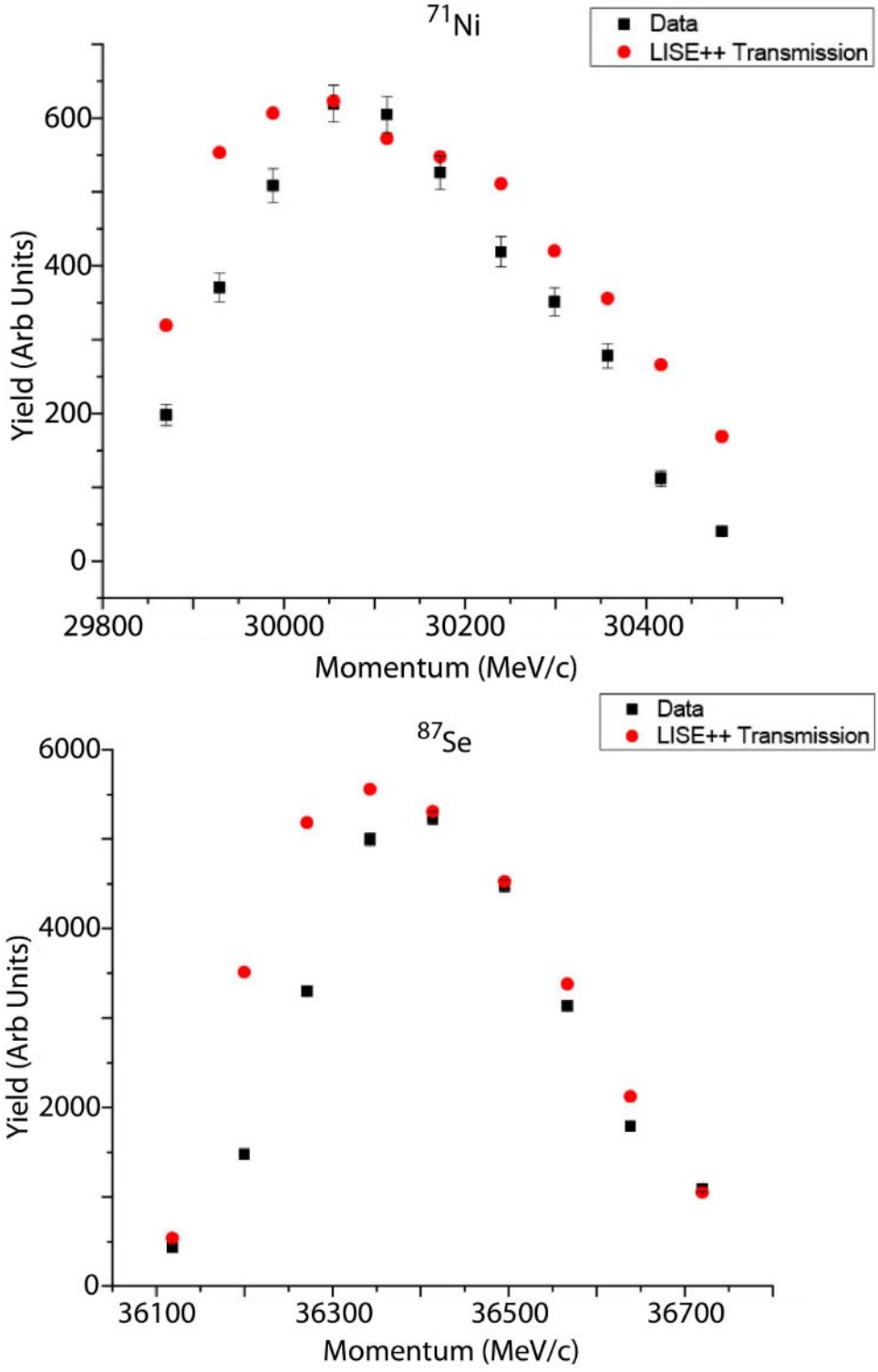

Figure 31: Measured momentum distributions for several isotopes compared to the LISE++ transmission predictions using the 5th Order Monte Carlo calculation. Note these simulations predict only relative transmission as a function of momentum and the total yields are not scaled to any particular cross section.

Figure 31 (Cont'd)

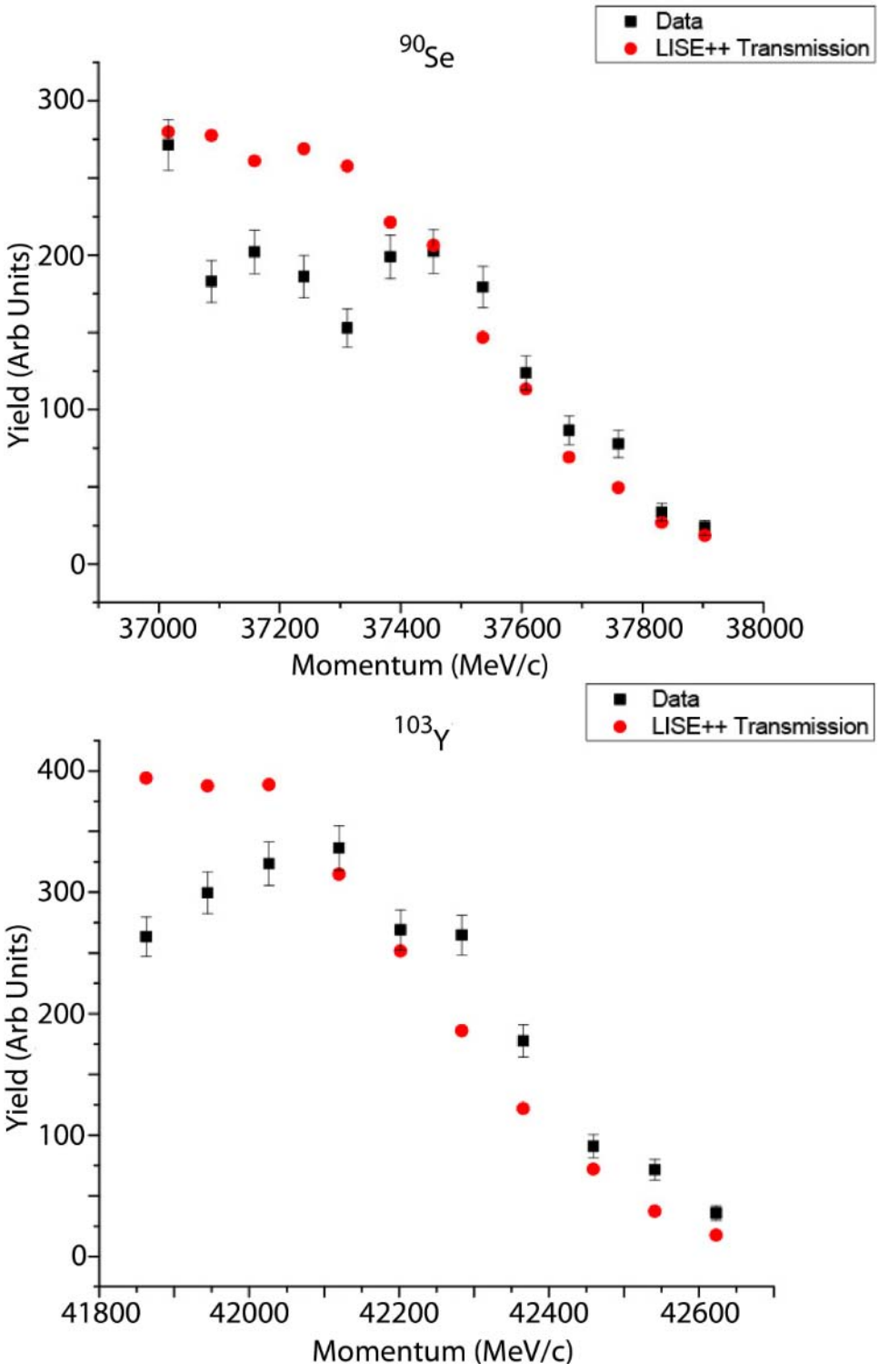

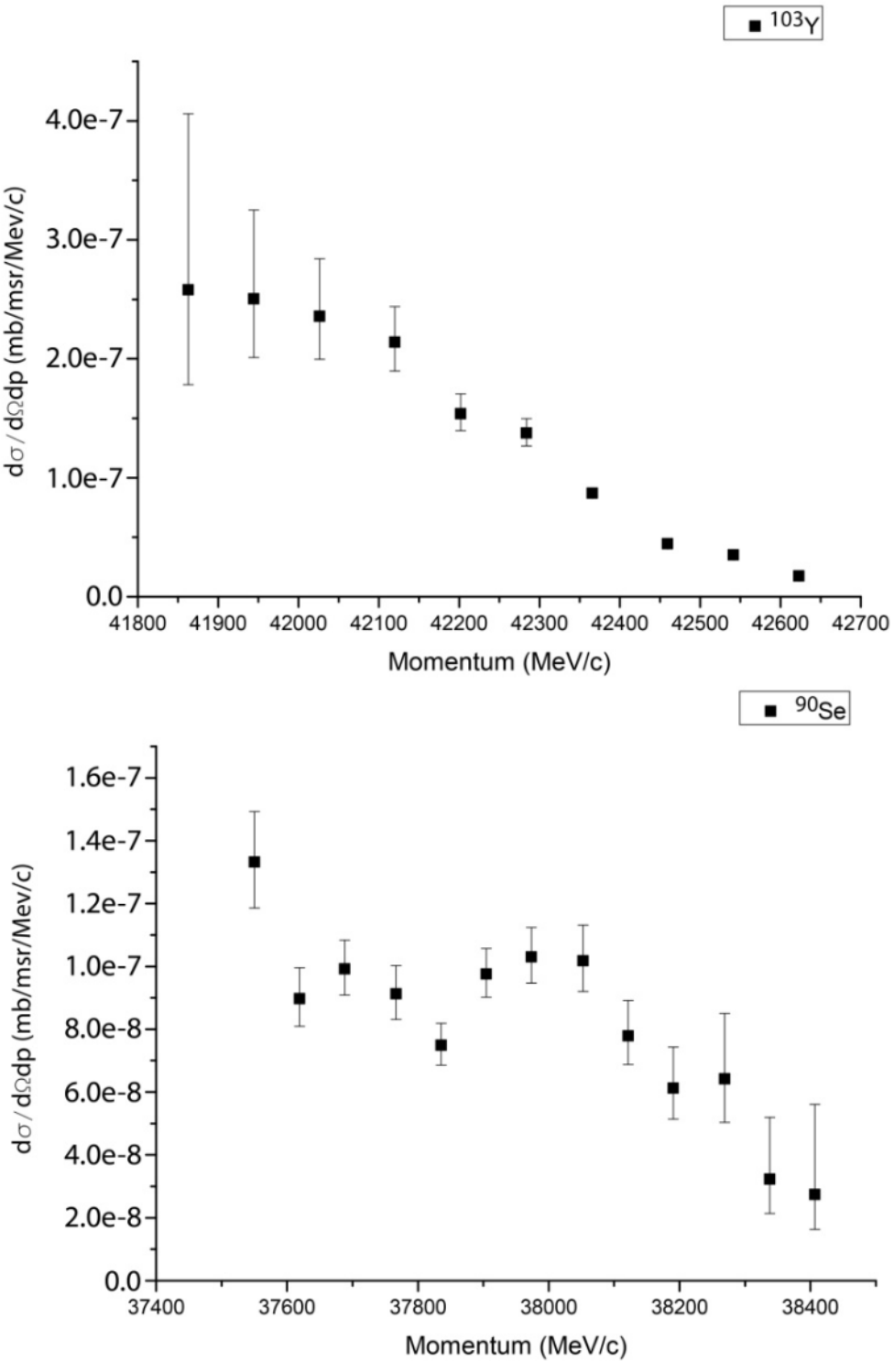

Figure 32: Double Differential Cross Sections determined from recorded momentum distributions. The angular acceptance was taken from the experimentally determined transmission given table 5, for the approprate momentum deviation from the central trajectory. The distributions, assuming a momentum independent angular transmission, are predicted to show a linear slope simlar to the first order predictions in Figure 29.

Figure 32 (Cont'd)

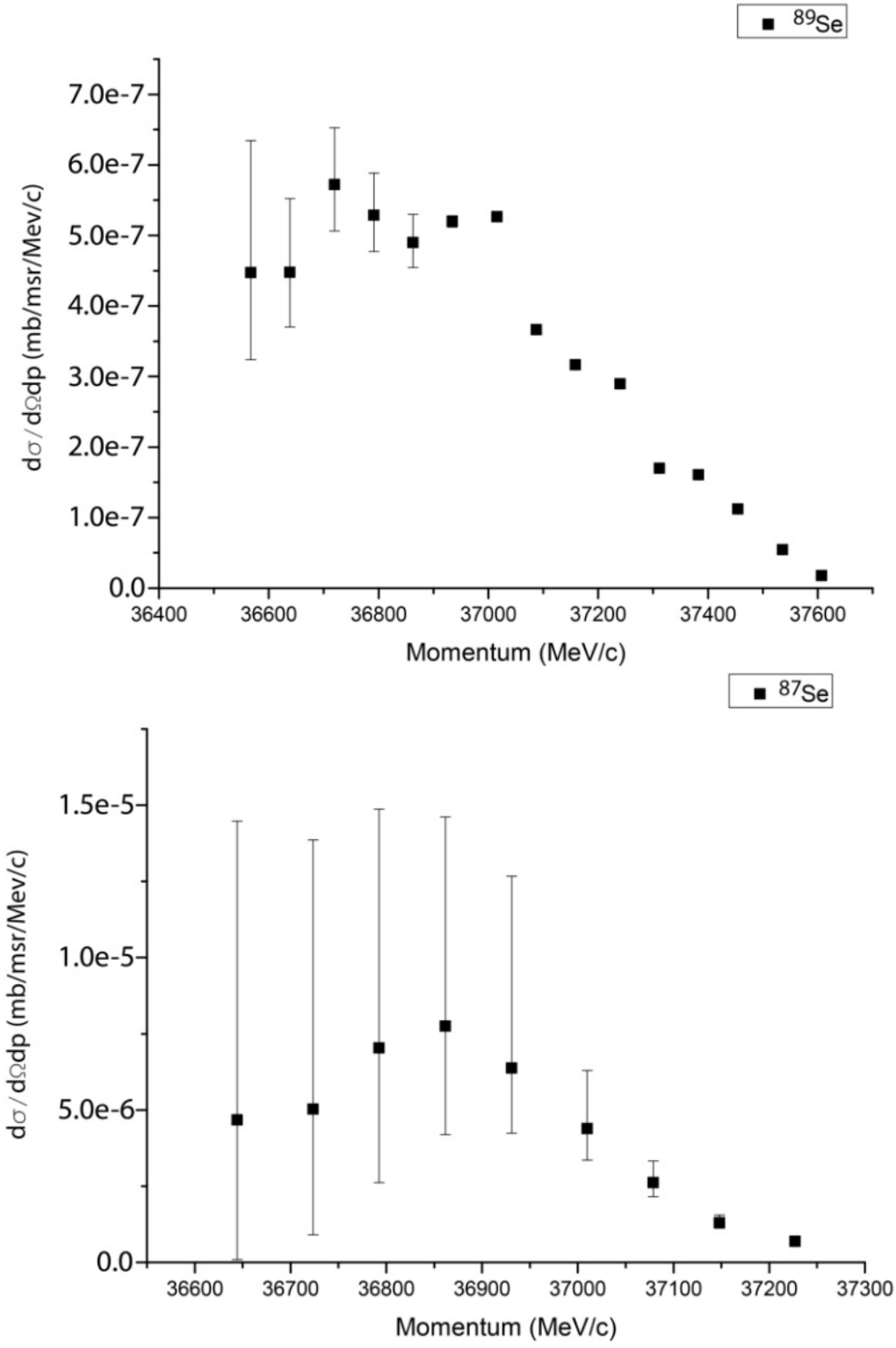

Figure 32 (Cont'd)

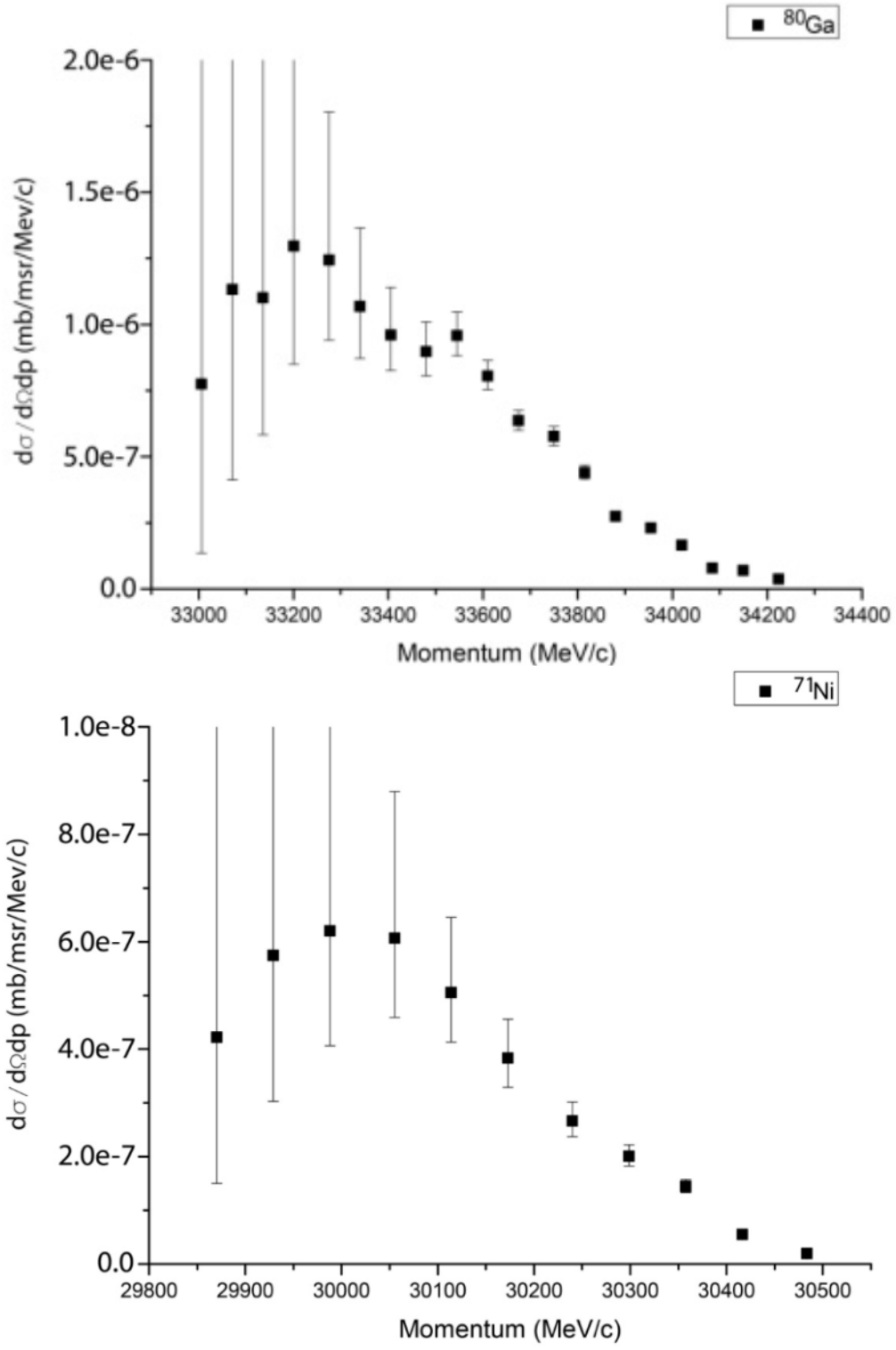

Given the beam current normalization with the NaI detectors, it was possible to integrate the total charge on target for the full data set. The LISE++ simulation of the solid angle as a function of mometum was used to determine the differential solid angle as a function of momentum. This was in turn used to generate double differential cross sections (at zero degrees in the laboratory) for the data observed in this experiment. The results are shown in Figure 32. The large error bars are due primarily to systematic errors in the determination of the solid angle.

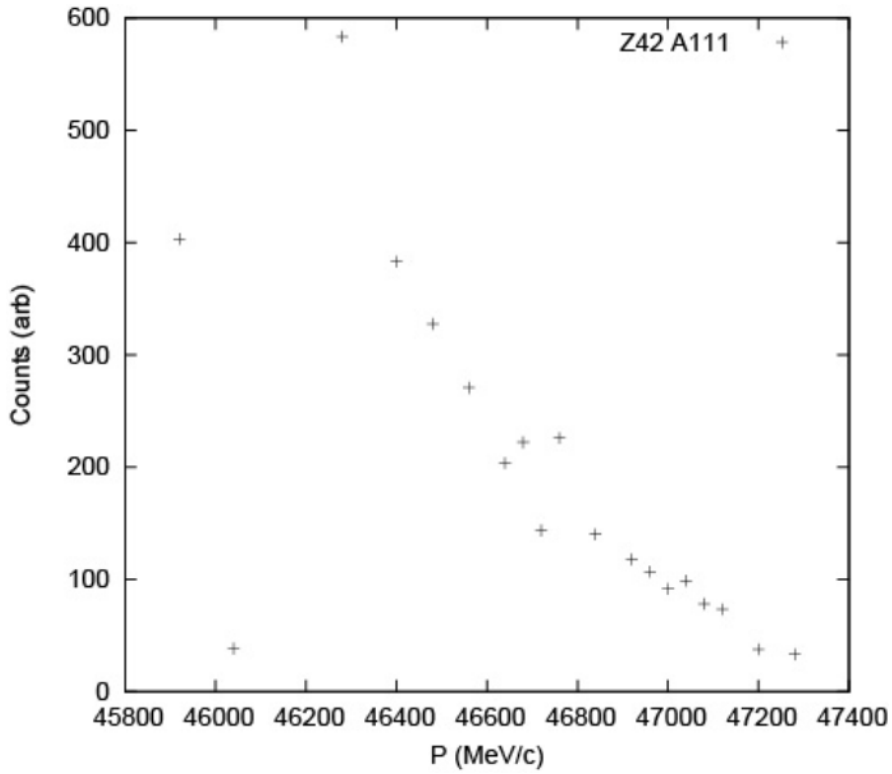

Figure 33: A sample of the momentum distributions generated in this work. The entire set of several hundred partial distributions is available at (http://www.nscl.msu.edu/~sherrill/nettleton/plots.pdf).

Figure 33 (Cont'd)

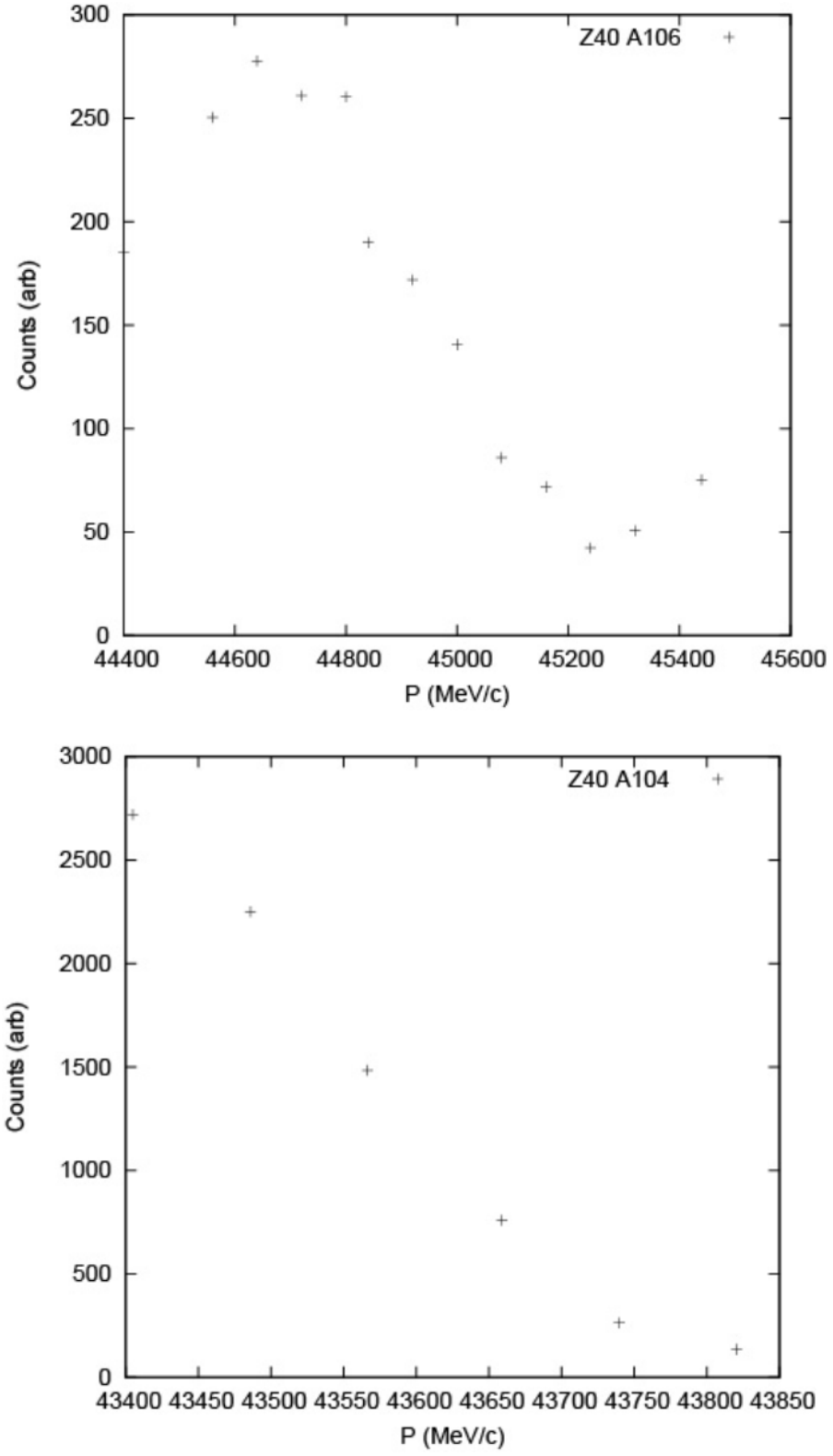

Figure 33 (Cont'd)

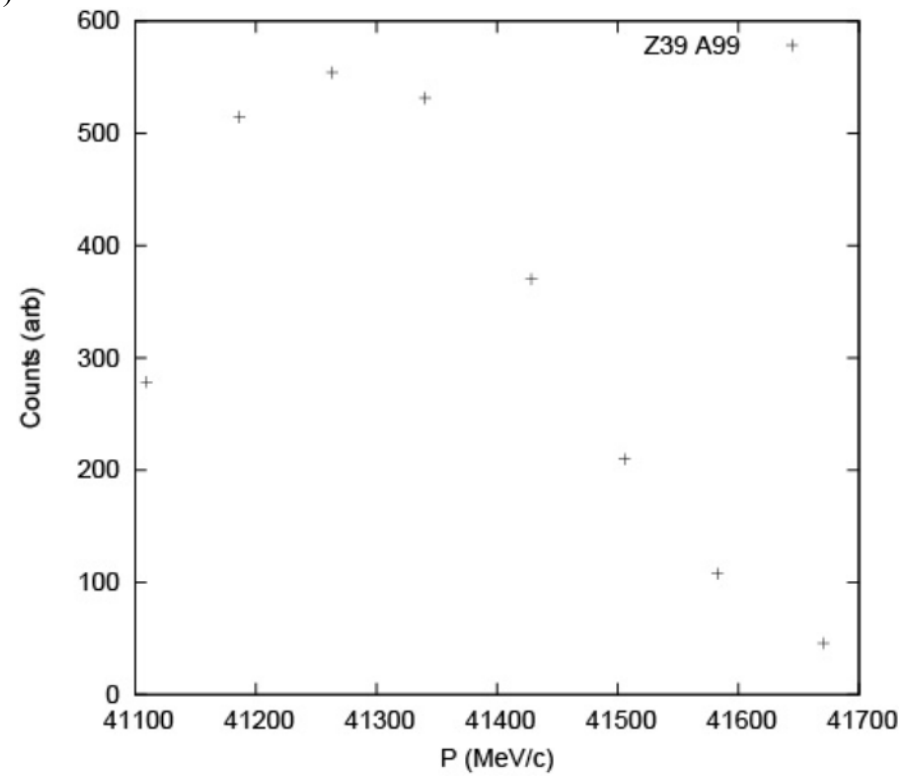

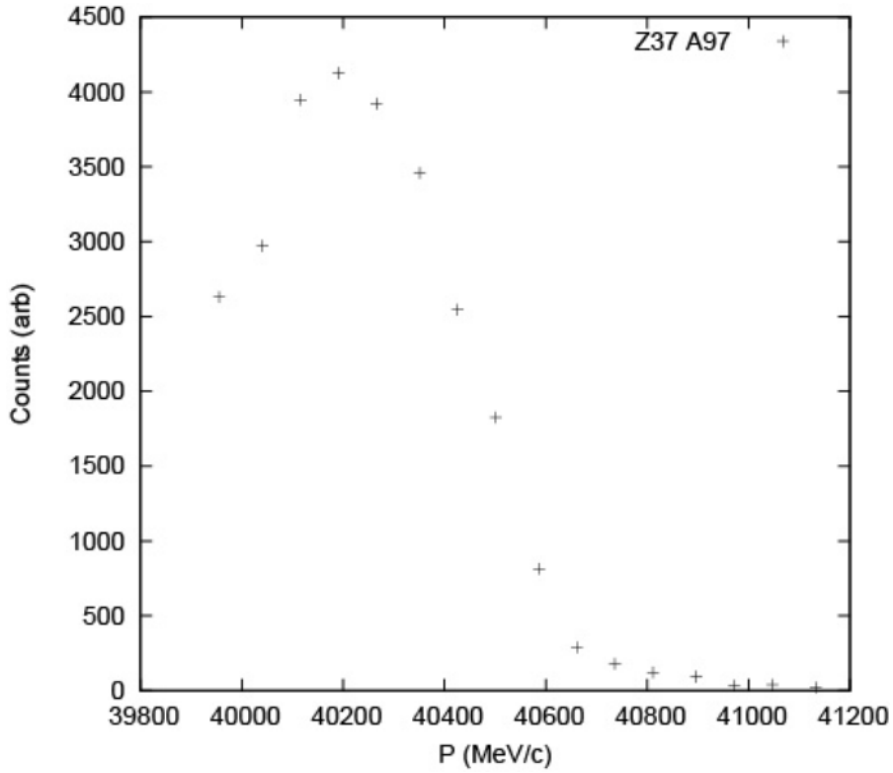

Figure 33 (Cont'd)

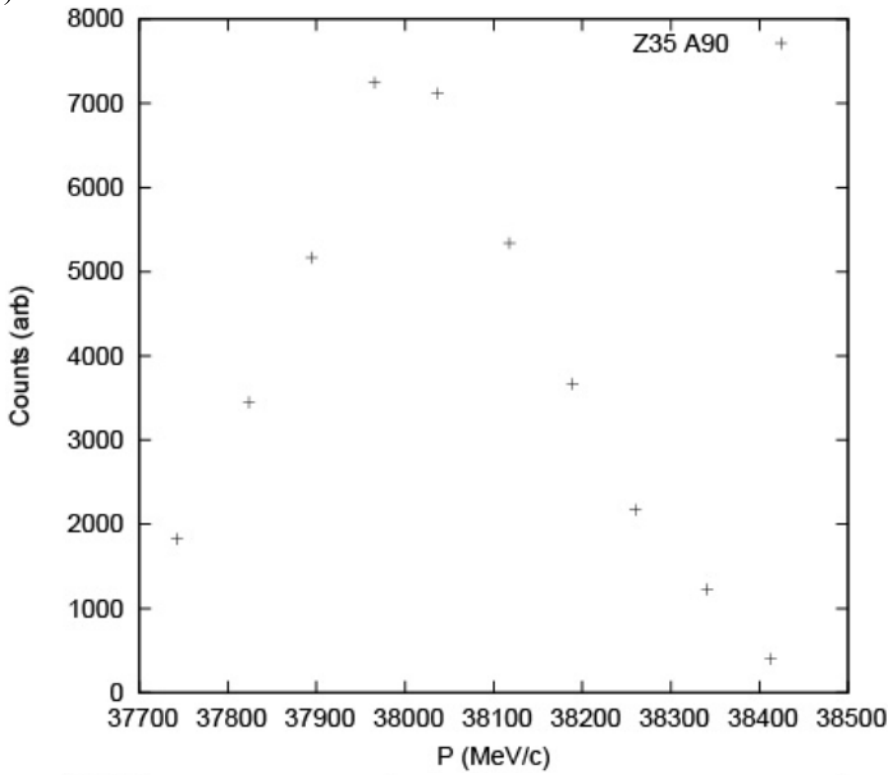

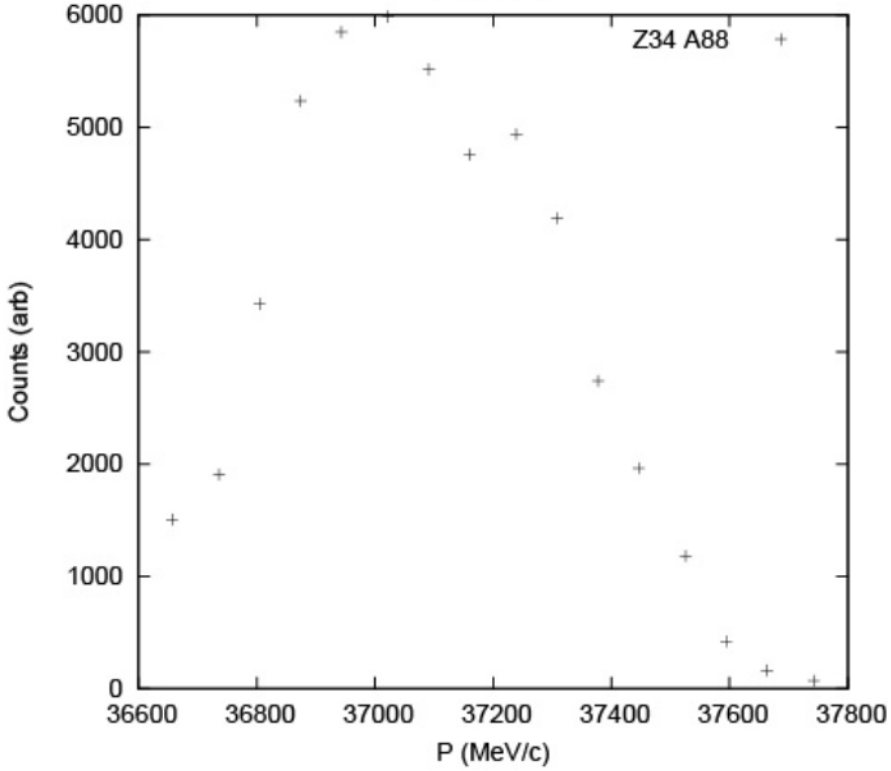

Figure 33 (Cont'd)

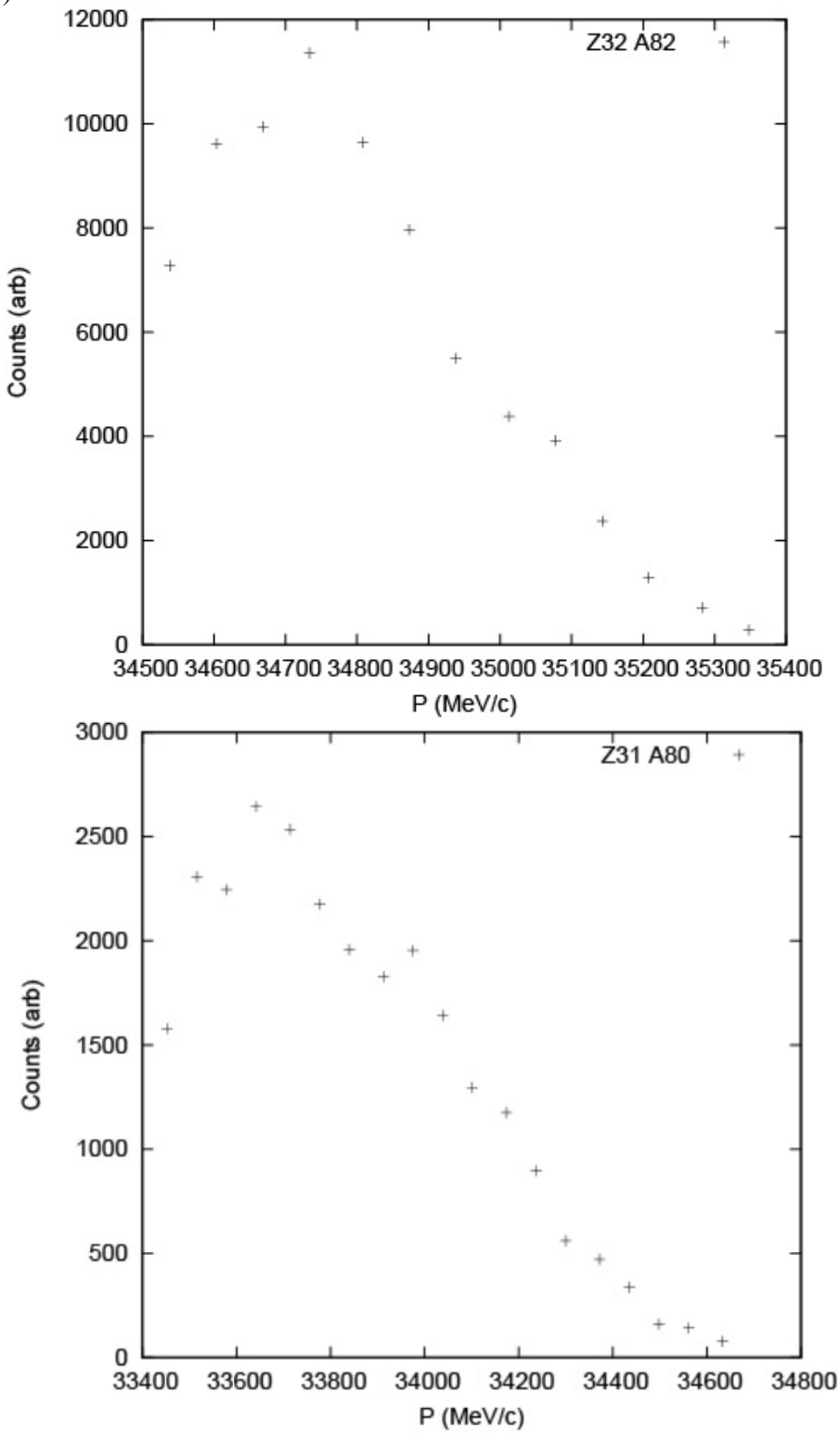

Figure 33 (Cont'd)

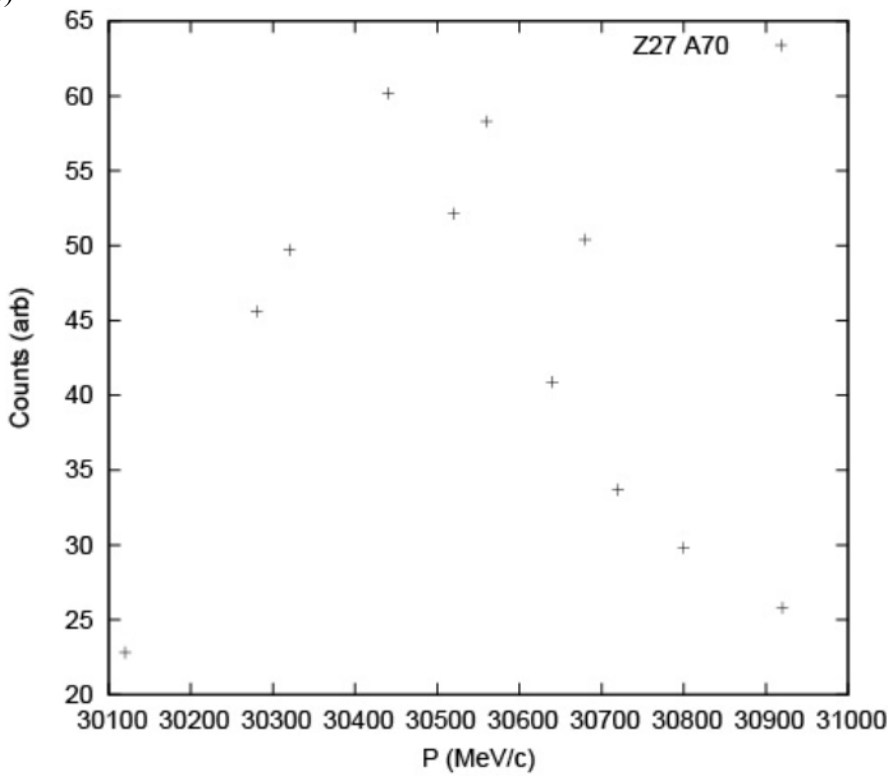

The data in Figure 33 is representative of the output generated by the automatic fitting routine applied to the data sets in Figure 24 to assess data validity, extract yields, fit peaks, and combine the results into momentum spectra. Due to the well over 100000 possible valid combinations of A, Z, Q, and P available in the data set, leading to over 400 partial momentum distributions, a representative sample was given a more detailed analysis using the transmission simularions in LISE++ and compared with theoretical predictions. When integrated for momentum and angular transmission losses the selected distributions were used to determine the total production cross sections.

5.3 Total Cross Sections

The measured momentum distributions combined with the angular distribution calculations can be extended to give the relative and total production cross sections for a given isotope. Using the calculated acceptances from an ion optics code, the momentum distributions can be corrected for losses during transmission. The resulting corrected distribution should represent the true picture of the momentum spread being generated during the reaction. This true distribution can then be integrated to give the total yield of a given isotope produced during the reaction. These integrated yields can then be combined with the beam rate, target thickness, and target density to give a total production cross section. It should be noted again that these cross sections apply to the entire process not just the fission component.

The total production cross sections were determined by a comparison between the differential cross sections and the LISE++ calculation. Due to computational constraints the LISE++ Monte Carlo code only calculates one of the three prefragments at a time and only for one particular final product with a given ionic charge state. In order to properly simulate a complete data set we needed to simulate the results from all three prefragments and then sum them in a manner consistent with the relative quantities of prefragments prescribed by the code. Before summing, each simulation was normalized to a fixed quantity, using the calculated transmission efficiencies to determine the total yield per simulation, and then multiplied by the fraction of total production assigned by LISE++. The charge state components were then corrected again using the GLOBAL method mentioned previously. To guarantee a fair comparison with the data the default binning of the simulations was adjusted to match the bin size of the data points with a momentum width of 0.2%. The application of all of these

corrections allowed for a final combined spectrum that gave yields at each of the data points corresponding to the predicted yield for a fixed number of produced fragments. The fragment number was then scaled to provide the best match between simulation and observation. The scaled fragment yield was used to calculate the production cross sections, with the differences between the simulated data curve and the real curve taken accounted for in the error. This method is explained in more detail in Appendix A.

The cross section results are shown in Figure 34 and Figure 35. The cross sections from this experiment agree reasonably well with previous results taken at GSI as well as predictions from the code LISE++. The results fall between those for the Pb target and the p^+ target as would be expected since Be falls between the two in geometric cross section. However, the Be results in this experiment fall closer to those of the Pb target than they likely should. From purely geometric considerations the beryllium reaction should have a cross section approximately four times larger than the proton and eight times smaller than the lead. This problem is compunded when including the fact the Coulomb cross section for the lead target is much larger than that of the beryllium target due to the former having 78 more protons. This behavior is predicted in the LISE++ simulations. The overall trend of reduction in cross sections with increasing neutron number however is consistent between the two small target (Be and proton) data sets and the simulations indicating that independent of the total cross section the relative cross sections remain constant between target materials where abrasion-fission is expected to be the dominant reaction. The set of isotopes shown above was chosen to show a trend in the cross section values with changing neutron number for two reasonable seperated values of Z where we had a substantial amount of data. We believe that this serves well as a representative set sufficient to prove the validity of the data analysis technique.

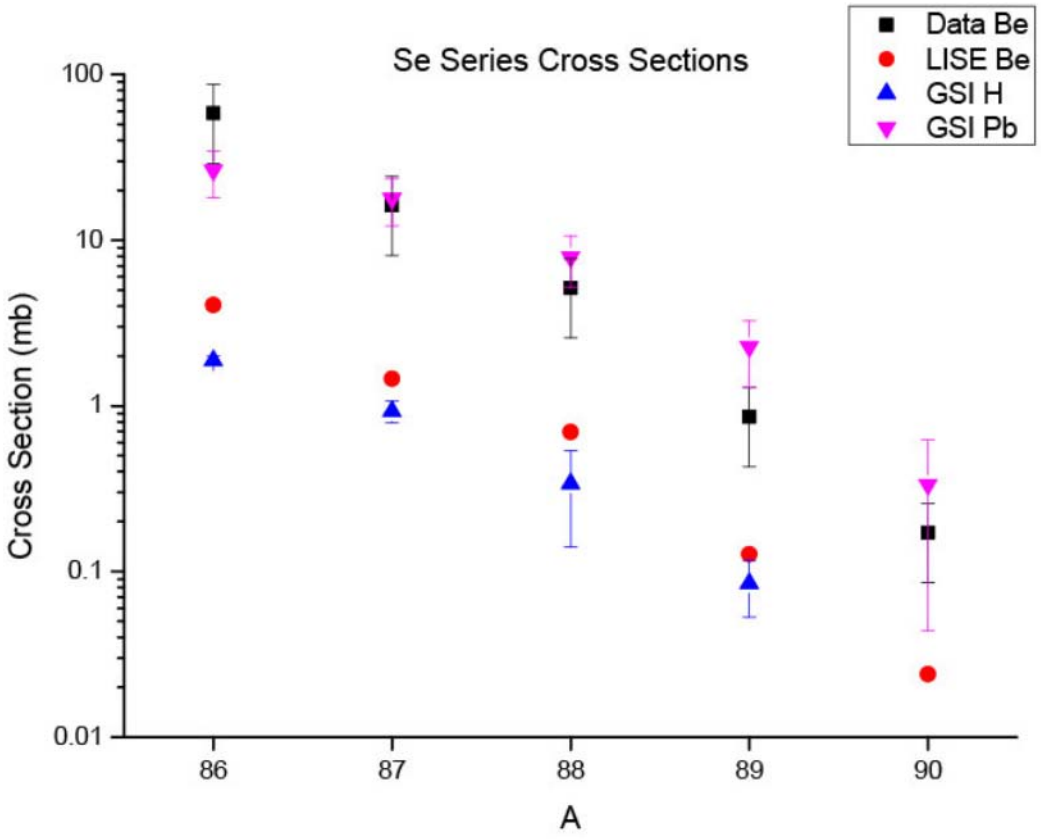

Figure 34: Comparisons of cross section data for Se isotopes taken in this experiment to previous work at GSI and the LISE++ predictions.

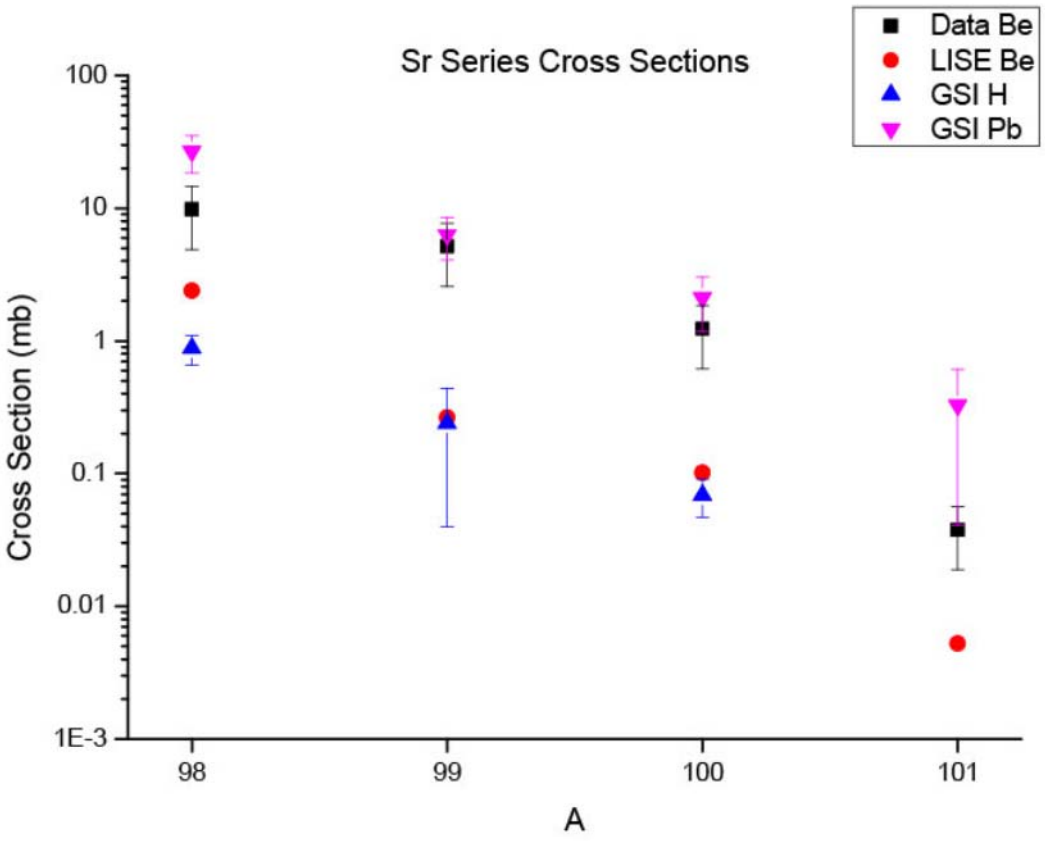

Figure 35. Comparisons of cross section data taken in this experiment to previous work at GSI and the LISE++ predictions.

5.4 Comparison to RIKEN and GSI Data

The experimental data shows that reliable identification of fission fragments at the NSCL is possible. Well resolved Z and A values for a range between Z = 25 and Z = 60 are observable for a number of magnetic rigidities and target thickesses. The particle identification plots are consistent with transmission predictions made by the LISE++ code and have been confirmed using isomer tagging. These results give confidence in our analysis technique which was based upon the the transmission simulations of LISE++. Both the results from the current work (Figure

24) and the RIKEN results (Figure 36) show an asymmetry in the A and Z distribution. This could be due to a change in the production mechanism or may be related to a transmission effect when a wedge is used. None of the settings without the scintillator at Image2 show this effect. A very slight asymmtry due to transmission is predicted by LISE for this case, but not as large as observed in the data. The agreement with the LISE++ model at 345 MeV/u (Figure 37) appears to be better than at 81 MeV/u. This indicates that there may be an energy dependence in some of the model parameters that is not seen in the RIKEN and GSI data from 300 MeV/u to 1000 MeV/u.

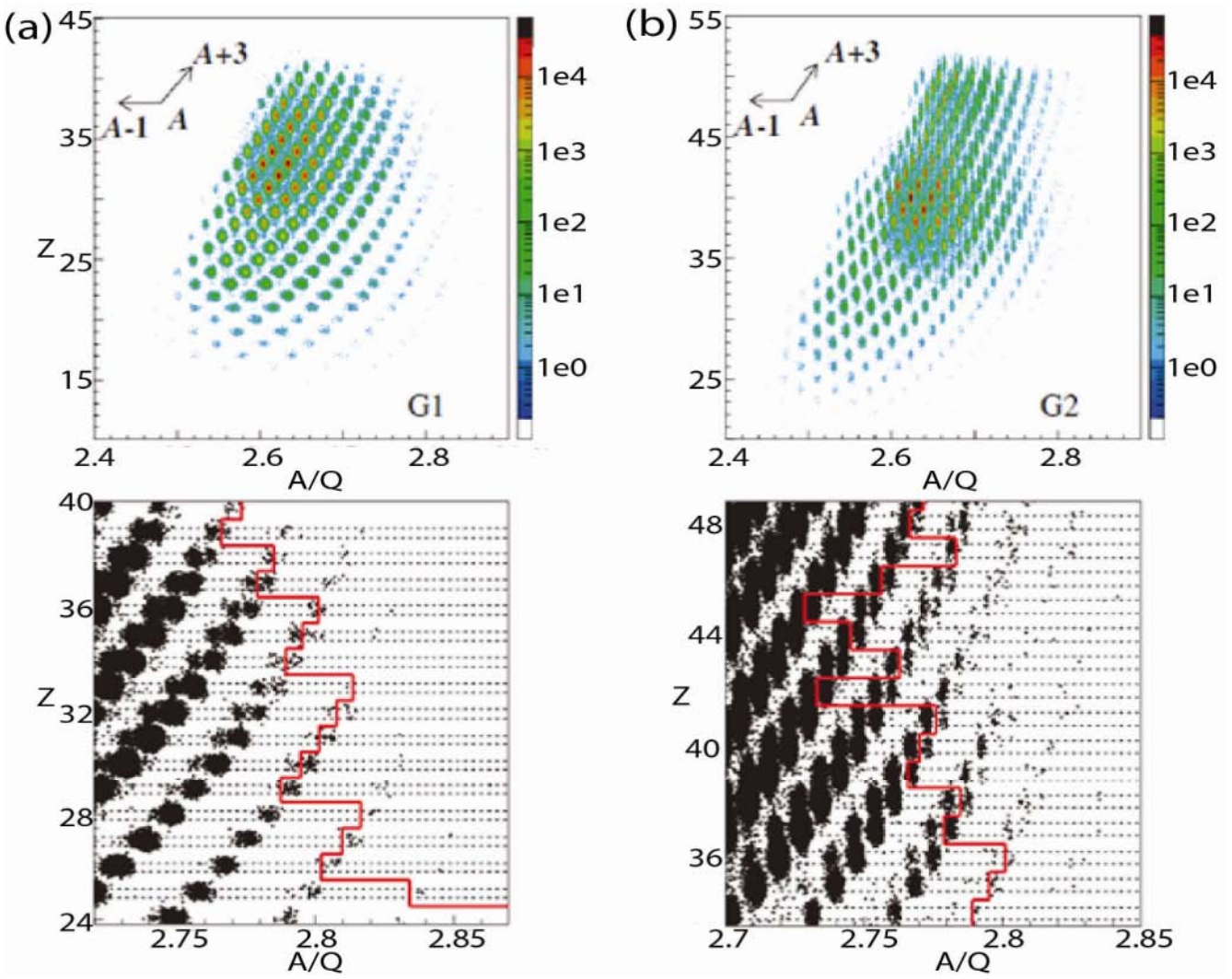

Figure 36: Particle identification plots from RIKEN abrasion fission experiment [Ohn10]. a) ^{238}U + Be set fo maximum transmission of Z = 30. b.) ^{238}U + Be for Z = 40. The results are similar to those seen in this work especially in the Z=45 region where both data show a slight asymmetry in the distributions for production of neutron-rich fragments.

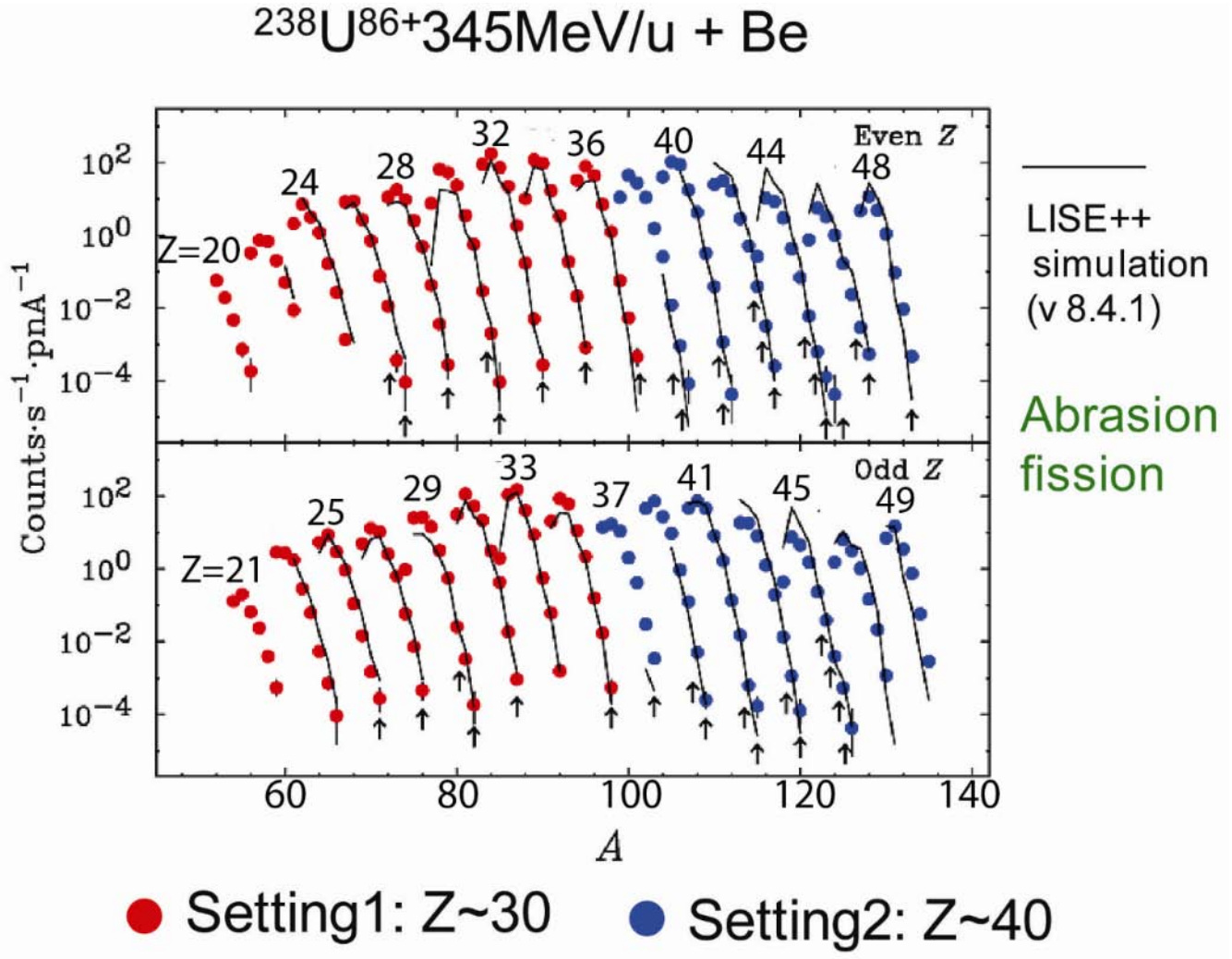

Figure 37. Production Yields from RIKEN [Ohn10] compared to LISE++ simulations. The solid agreement between prediction and results indicate that both the transmission and production cross section are being well modelled. The agreement with the LISE++ model at 345 MeV/u appears to be better than at 81 MeV/u. This indicates that there may be an energy dependence in some of the model parameters that is not seen in the RIKEN and GSI data from 300 MeV/u to 1000 MeV/u.

5.5 Isomer Identification

During the course of analyzing the data for this experiment eight previously unreported isomers and three previously unobserved transitions were observed as shown in Figure 38. Particle identification issues discussed in a previous section required observation of isomers to establish a calibration for the detector system. In the process of finding and identifying a known isomer for the identification the above isomers were also observed. These isomers fall into the region most strongly populated by the neutron rich fission fragments observed in this experiment which has not been studied for isomeric states in great detail previously. Because the experiment was designed to use isomers for calibration rather than to study them specifically the setup was not ideal for these measurements, meaning that there was a low efficiency as well as limiting the lifetimes to the microsecond range. From these results it appears that a more robust experiment to study fission isomers would likely yield even more isomers and better detail abou the existing ones. These results are described in full detail in the work of Folden, Nettleton et al.[Fol09].

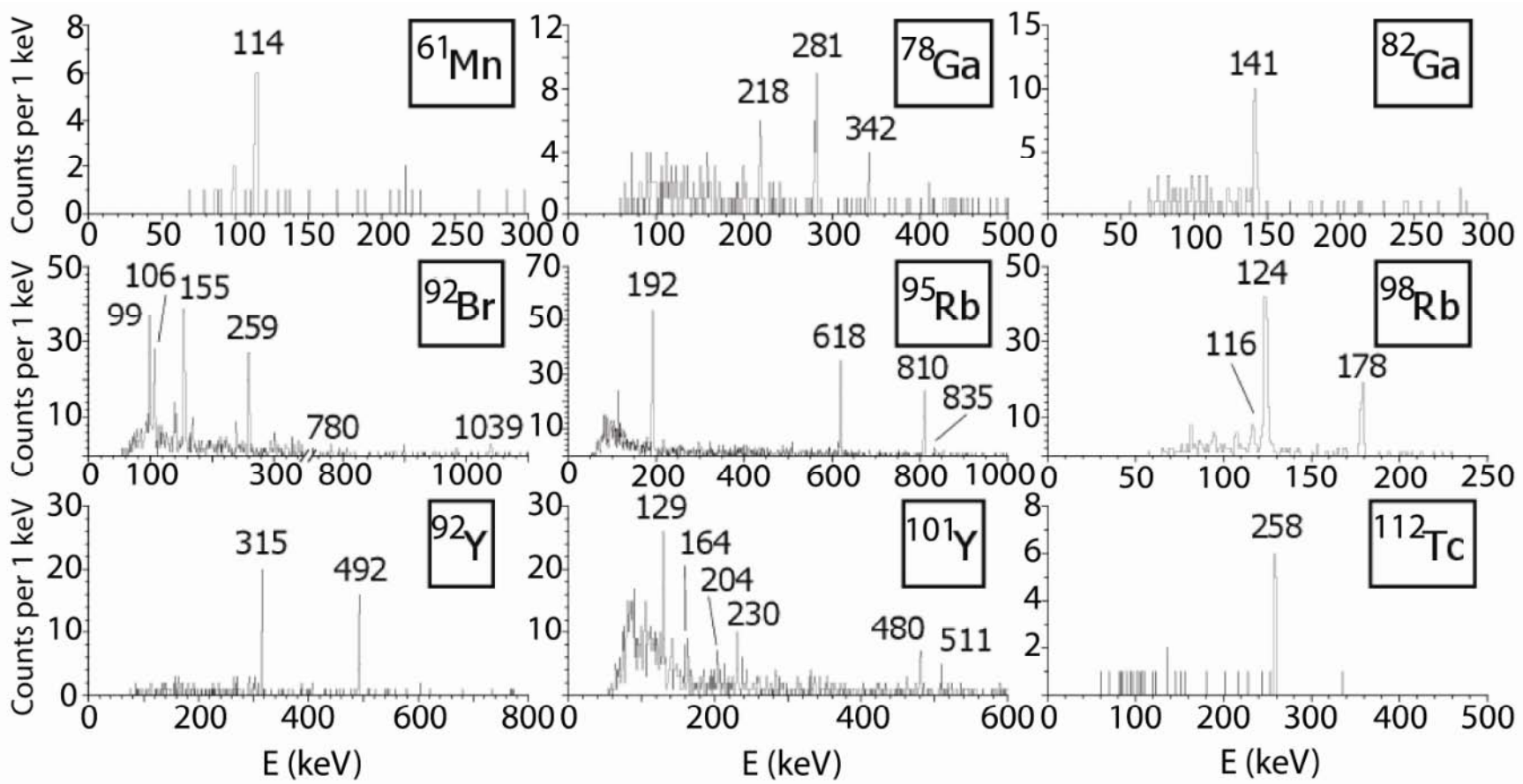

Figure 38: New Isomers and Transistions observed during the experiment [Fol09]

Figure 38 (Cont'd)

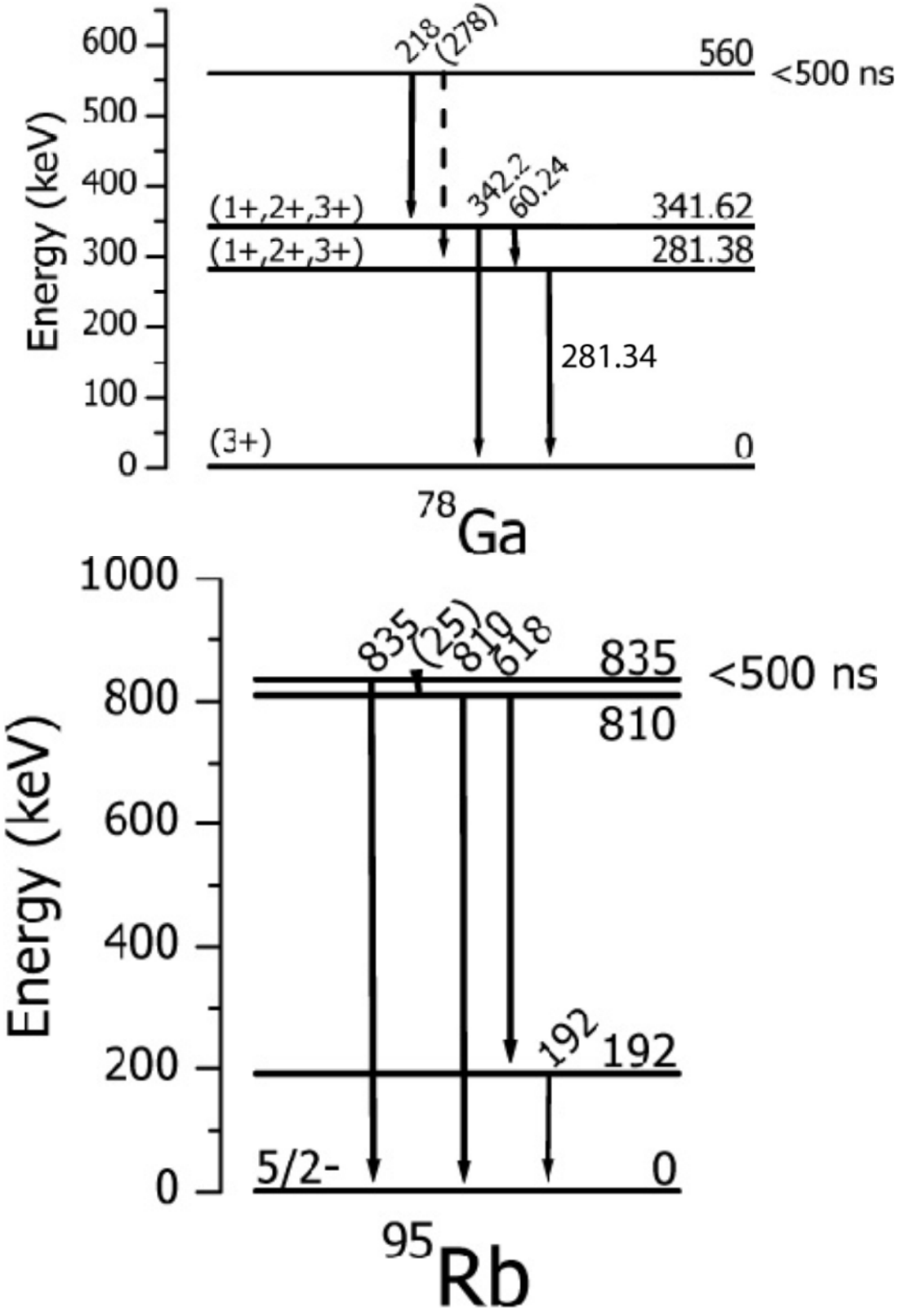

Figure 38 (Cont'd)

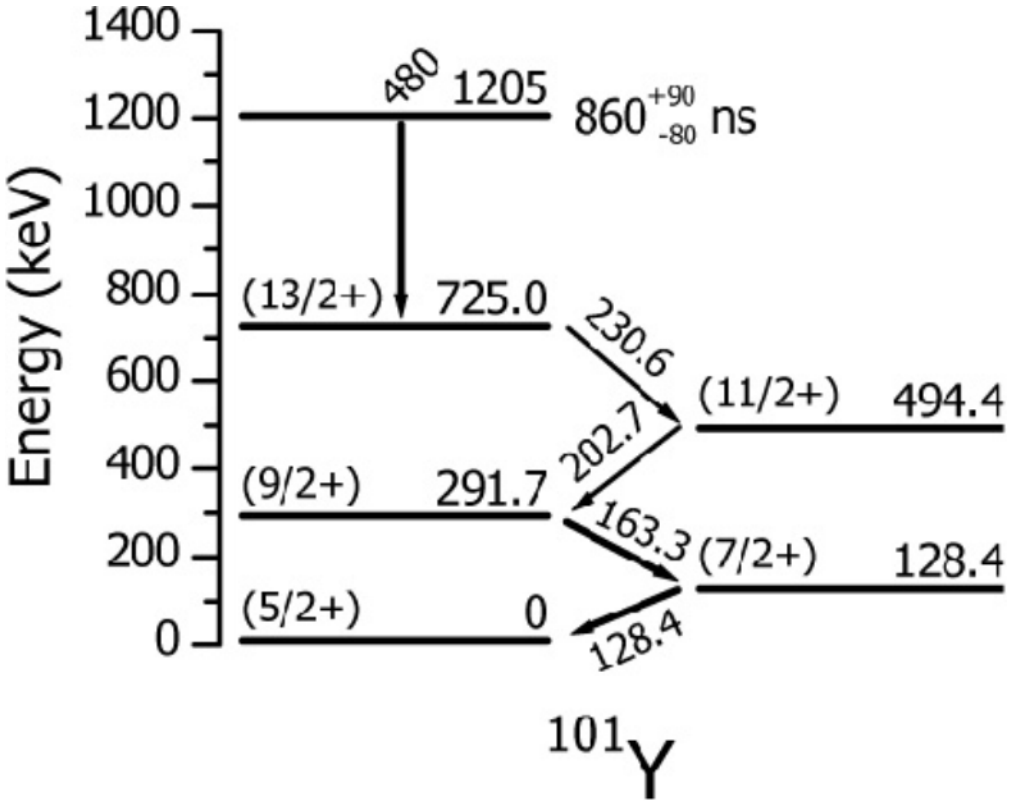

6. Conclusions

The experiment described in this dissertation achieved its basic objectives, identified several areas of interest for future study, and opened paths for future developments. The central achievement of this work was the measurement of a representative set of cross sections and momentum distributions of isotopes most strongly produced in fragmentation-fission at energy around 81 MeV/u. These data improve our ability to predict isotopic yields at energies below what had been done previously. This is important for the development of future facilities, such as FRIB, which plan to use fission as a production mechanism. The total cross sections were found to be higher than the LISE++ predictions for this experiment and fell between the GSI results for lead and proton targets at 750 MeV/u while evolving in the same way with increasing neutron number. Significantly, they were closer in value to the lead target results from GSI than the LISE++ fission model would predict, indicating that the lower beam energy may result in some fragments produced at lower excitation energy (similar to that for Coulomb fission). Further work is necessary to confirm these results.

As an element of this work, the momentum distributions (differential cross sections as a function of momentum) for a number of isotopes were measured and compared to the LISE++ code predictions. The experimental results showed that the LISE++ model predictions for the shape of the fragment momentum distributions were in general agreement with the data, verifying the predictions of energy distribution between fragments during the fission reaction. From the momentum distributions it was also shown that optics terms up to the third order are

significant for the prediction of fragment transmission when the entire acceptance of the A1900 is filled. The central two percent of the A1900 momentum acceptance was shown to have the nearly full solid angle acceptance, but this dropped off to below 20% of the full acceptance near the limit of acceptance at 2.5%. In fragmentation reactions the effect of this reduced acceptance would be less significant due to the smaller FWHM of the fragmentation distributions in angle space compared to the fission distributions with vales of approximately 70 and 230 mrad respectively for isotopes typical in this work. In the case of fission the acceptance of the separator as a function of momentum was shown to be important and this should be considered in the design of separator optics.

The measurements of the cross sections and momentum distributions required extensive work in developing particle identification techniques that are effective at lower beam energies. The primary particle identification difference between this work and previous fission experiments was determination of the fragment charge state by measurement of total kinetic energy. Due to the high beam energy of the GSI experiments it was possible to assume that the atomic charge state was equal to the nuclear atomic number, which allowed for successful particle identification using the mass to charge ratio. At lower energies, multiple charge states are present which we have shown makes resolving the fragments using only the mass to charge ratio impossible. To account for this we have developed a method to identify the charge state as an integer value based upon the fragments total kinetic energy. Development of this technique allows for fission experiments to be performed at much lower energies than those used at GSI. This means that current facilities such as the NSCL and future facilities planned like FRIB with a lower beam energy than GSI and RIKEN currently have can use fission to generate rare isotopes or study.

This experiment was also the first application of isomer tagging to verify particle identification at NSCL. Isomer tagging in the particle identification process identifies a number of new isomers and allowed us to propose several transition schemes as well [Grz95]. The new isomers identified are usable for particle identification for future experiments, and for providing information on the nuclear structure of neutron-rich isotopes. The newly identified isomers allow smaller subsets to be examined rather than the whole distribution simultaneously due to it now being possible to find a tagging isomer near many isotopes of interest. A number of isomers were observed in the neutron rich region between Z = 35 and Z = 40, which invites future investigation. It is an interesting observation that the fission process produces a large number of isotopes.

Several follow-up experiments are suggested based upon the results of the present work. Due to the increased number of isomers available for tagging after this experiment, measurement of exotic cross sections is now much more feasible. The new tagging isomers allow for transmission settings to focus on a much smaller region of fragments allowing for higher rates of collection. In addition to this work, which focused on momentum distributions, a future work to examine the fission angular distributions would allow for much more reliable determination of fragment transmission and the total production cross sections. This could be performed by shifting the incident beam angle and examining how the transmission profile changes. With higher collection efficiency, a more narrowly focused acceptance, and a gamma detection setup with more detectors and a higher efficiency (than the 1% at 1.4 MeV in this experiment), there also appears to be great potential for isomer studies in some of the previously unexplored regions that have been identified during this experiment.

The results of this work have application in the design of new facilities such as FRIB. The transmission characteristics observed in this experiment have confirmed many of the predictions of LISE++ and have shown the acceptance values necessary to maximize fission yields. The methodology used demonstrates the viability of fission for the production of secondary beams at lower energies than those used by GSI and RIKEN. This work opens the possibility for many future experiments at NSCL and FRIB, as well as other facilities that use in-flight fission in the energy range of 100 to 200 MeV/u.

APPENDICES

Appendix A.

In the course of the analysis a large amount of data for hundreds of isotopes was collected. The intent of this appendix is to provide the details on how to calculate total cross sections from double differential momentum distributions contained in (http://www.nscl.msu.edu/~sherrill/nettleton/plots*.ps) where the "*" represents the target thickness in mg/cm^2 (9,47, or 94) . The steps listed below outline the proceedure. The spectrum refereed to is for one of the double differential cross sections shown in the plots.pdf file.

This guide assumes the use of LISE++ Version 9.1.12 with the abrasion fission production mechansism. A sample LISE++ file that can be used for the process is located at (http://www.nscl.msu.edu/~sherrill/nettleton/05048Run1118Settings.lpp).

Cross Section Calculation Procedure:

1. Input the corresponding settings for the spectrum to be analyzed into LISE++ including the specific isotope and the charge state to be examined. Set the fission low, med, and high excitation energy fissile nucleus by using the button provided in LISE++. A sample configuration for Setting 1118 is provided in the directory with the data sets.
2. Run the LISE++ Monte Carlo transmission simulation for the fragment momentum (P in the LISE++ code) after the FP_SLITS set for Abrasion-Fission Low Ex. Allow simulation to run until the desired statistical accuracy is achieved.
3. Record number of counts in the generated distribution and the efficiency percentage, save 1-d P distribution to a file

4. Repeat procedure for Med Ex and High Ex fragments by selecting the appropriate mid or high checkbox in the fission options
5. Re-bin the saved 1-d simulations to match the momentum bin width from experiment (0.2% dp/p) and center each bin upon corresponding point from data set
6. Determine the total number of points required to generate each distribution by dividing the total counts by the transmission fraction
7. If not already done, normalize each of the distributions to the same, set number of total counts
8. Sum the three distributions (Low, Med, and High Ex) point-wise weighted by their relative contributions according to LISE++. This can be done by dividing the partial cross section (found in Abrasion-Fission production mechanism dialogue) for each energy setting by the total cross section and then multiplying each the distribution for each energy range by its respective fraction. Upon summing, the total counts should then be equal to the initial normalization number
9. Scale the summed simulation distribution until it matches the experimental data set as well as possible
10. Multiply the normalization number by the scaling factor to get the total number of counts required to generate the simulation (and the corresponding data set)
11. Correct total by dividing by the fraction of total yield produced in the observed charge state (can be taken from GLOBAL found in LISE++ under “Utilities”)
12. Calculate the cross sections using the total fragments produced (from step 11), the total primary beam on target (taken from scalars), and the target parameters (thickness and

material). The integrated beam on target for each setting can be found in the directory with the data set.

BIBLIOGRAPHY

Bibliography

[Ant94] T. A. Antaya, S. Gammino, Rev. Sci. Instr., 65 (1994) 1723

[Arm96] P. Armbruster, M. Bernas, S. Czajkowskim H. Geissel et al., Z. Phys. A 355, 191-201 (1996)

[Aum05] T. Aumann, Eur. Phys. J. A 26, (2005) 441-478

[Baz02] D. Bazin, O. Tarasov, M. Lewitowicz, O. Sorlin, Nucl. Instr. and Meth. A 482 (2002) 307.

[Ben98] J. Benlliure et al., Nuclear Physics A 628 (1998) 458-478

[Ben02] J. Benlliure et al., Eur. Phys. J. A 13, (2002) 93–98

[Ber94] M. Bernas et al., Phys. Lett. B 331 (1994) 19-24

[Ber98] M. Bernas et al., Nuclear Physics A 630 (1998) 41c-51c

[Ber03] M. Bernas et al., Nuclear Physics A 725 (2003) 213–253

[Ber06] M. Bernas et al., Nuclear Physics A 765 (2006) 197–210

[Bert88] C. Bertulani, G. Baur, Physics Reports 163, Nos. 5 & 6 (1988) 299-408

[Berz93] M. Berz et al., Phys. Rev. C 47 (1993) 537

[Bethe30] H. Bethe, Annalen der Physik Volume 397, Issue 3, pages 325–400, 1930

[Brown80] K.L. Brown et al., CERN Report 80-04, 1980.

[Bol05] G. Bollen, D.J. Morrissey, S. Schwarz, A Study of Gas-Stopping of Intense Energetic Rare Isotope Beams, Nucl. Instr. Meth., A550, 27 (2005)

[Bon01] Bonofiglio, J.; Alfredson, S.; Hitchcock, S.; Marti, F.; Rodriguez, A.; Stork, G. CYCLOCTRONS AND THEIR APPLICATIONS 2001: Sixteenth International Conference. AIP Conference Proceedings, Volume 600, pp. 117-119 (2001).

[Bur57] Burbidge et al., Reviews of Modern Physics, vol. 29, Issue 4, pp. 547-650

[Cle95] H. –G. Clerc et al., Nuclear Physics A 590 (1995) 785-794

[Coh74] S. Cohen, F. Plasil, W. J. Swiatecki, Annals of Physics 557-596 (1974)

[Det85] C. Détraz, *Nature* 315, 291 - 294 (23 May 1985)

[Dob07] A. Dobrowolski, K. Pomorski, J. Bartel, Physical Review C 75, 024613 (2007)

[Donz98] C. Donzaud et al. Eur. Phys. J. A 1, 407-426 (1998)

[Eng95] Ch. Englemann et al., Z. Phys. A 351-352 (1995)

[Enq99] T. Enqvist et al., Nuclear Physics A 658 (1999) 47-66

[Fau02] H. R. Faust, Eur. Phys. J. A 14, 459–468 (2002)

[Fol09] C. M. Folden, A. S. Nettleton et al., Physical Review C 79, 064319 (2009)

[Gai91] J.-J. Gaimard, K.-H. Schmidt, Nuclear Physics A531 (1991) 709-745

[Gru99] H. A. Grunder et al., "ISOL Task Force Report to NSAC", Nov 22, 1999 <http://www.er.doe.gov/np/nsac/docs/ISOLTaskForceReport.pdf>

[Grz95] R. Grzywacz, Phys. Lett. B 355, (1995) 439

[Hau11] M. Hausmann, D. Morrissey, B. Sherrill, Internal FRIB Report (2011)

[Hax50] Haxel, Jensen, and Seuss, Z. Physik 128, 295 (1950)

[Hen05] D. Henzlova, Dissertation, Czech Technical University In Prague (2005)

[Hes96] M. Hesse, M. Bernas et al., Z. Phys. A 355, 69-75 (1996)

[Huy04] M. Huyse "The Why and How of Radioactive Beam Research", Lect. Notes Phys. 651, 113–135 (2004)

[Jun07] A. Jungclaus et al., Phys. Rev. Lett. 99, 132501 (2007)

[Lau73] Lauterbur, P. C. Nature, Volume 242, Issue 5394, pp. 190-191 (1973)

[Lam80] S. T. Lam et al., Phys. Rev. C 22, 2485–2491 (1980)

[Lan11] K. Langanke, G. Martínez-Pinedo, I. Petermann, F.K. Thielemann, Progress in Particle and Nuclear Physics 66 (2011) 319–328

[Lin96] J. Lindhard, A. Sorensen, Physical Review A 53 4 (1996) 2443-2456

[Lov01] Walter D. Loveland, David J. Morrissey, Glenn T. Seaborg, Modern Nuclear Chemistry, Wiley-Interscience 2001

[May50] M. G. Mayer, Phys. Rev. 78, 16 (1950)

[Mol09] P. Moller et al., PRC 79, 064304 (2009)

[Mor80] D. J. Morrissey et al., Physical Review C 21, (1980) 1783-1798

[Mor97] D. J. Morrissey, Nuclear Physics A, 616 (1997) 45c-55c

[Mor98] D. J. Morrissey, B. M. Sherrill, Phil. Trans R. Soc. Lond. A (1998) 356, 1985-2006

[Mor03] D. J. Morrissey et al., NIM B 204 (2003) 90-96

[Mor04] D.J. Morrissey and B.M. Sherrill, In-flight Separation of Projectile Fragments, Lect. Notes Phys. 651, 113–135 (2004)

[Mus03] B. Mustapha, J. A. Nolan Nuclear Instruments and Methods B 204 (2003) 286–292

[Ohn08] T. Ohnishi et al., J. Phys. Soc. Jpn. 77, 083201 (2008)

[Ohn10] T. Ohnishi et al., J. Phys. Soc. Jpn. 79, 073201 (2010).

[Per00] J. Periera-Conca, Dissertation, University of Santiago de Compostela (2000)

[Sch94] K. –H. Schmidt et al., Phys. Lett. B. 325 (1994) 313-316

[Sch98] K. –H. Schmidt, A. R. Junghans et al., Nuclear Physics A 630 (1998) 208c-214c

[Sch00] K. –H. Schmidt et al., Nuclear Physics A 665 (2000) 221-267

[Sch02] K. –H. Schmidt et al., Nuclear Physics A 710 (2002) 157-179

[Scheid98] C. Scheidenberger et al., Nucl. Instr. and Meth. B 142 (1998) 441

[Schwar09] S. Schwartz, “Opportunities and Challenges for the next Facility for Rare Isotope Beam” Presented to ICIS (2009)

[Schwar10] S. Schwartz et al., Rev. Sci. Instrum. 81, 02A503 (2010)

[Sher11] B. M. Sherrill, “What is FRIB?”, Presented to Second Uio-MSU-ORNL-UT School, 3 January 2011

[Soul97] G. A. Souliotis et al., Phys. Rev. C 55 5 (1997) 2146-2149

[Sto05] A. Stoltz et al., Nuclear Instruments and Methods in Physics Research B 241 (2005) 858–861

[Swan94] D. Swan, J. Yurkon, D. Morrissey, Nuclear Instruments and Methods in Physics Research A 348 (1994) 314-317

[Tan85] I. Tanihata et al., Phys. Rev. Lett 55 (1985) 2676

[Tar03] O.B. Tarasov, D. Bazin, NIM B 204 (2003) 174-178

[Tar07] O.B. Tarasov, Personal Communication (2007)

[Tar08] O.B. Tarasov, D. Bazin, NIM B 266 (2008) 4657-4664

[Ter75] Ter-Pogossian, M.M.; M.E. Phelps, E.J. Hoffman, N.A. Mullani (1975). "A positron-emission transaxial tomograph for nuclear imaging (PET)". *Radiology* 114 (1): 89–98

[Uen08] H. Ueno, European Physical Journal-Special Topics 162 (2008) 221-229

[Wig36] E. Wigner, Phys. Rev. 51, 106 1936

[Wil76] B.D. Wilkins, E.P. Steinberg, R.R. Chasman, Phys. Rev. C 14 (1976) 1832.